

Dissertation

On the Origin and Propagation of Ultra-High Energy Cosmic Rays

(Measurements & Prediction Techniques)

Nils Nierstenhoefer

Wuppertal, 2011

University of Wuppertal



Supervisor/First reviewer: Prof. Dr. K.-H. Kampert
Second reviewer: Prof. Dr. M. Risse

Motivation & Preface

It is a long known fact that cosmic rays reach Earth with tremendous energies of even above 10^{20} eV. Despite of decades of intensive research, it was not possible to finally reveal the origin of these particles. The main obstacle in this field is their rare occurrence. This is due to a very steep energy spectrum. To make this point more clear, one roughly expects to observe less than one particle per km^2 in one century exceeding energies larger than 10^{20} eV. To overcome the limitation of low statistics, larger and larger cosmic ray detectors have been deployed. Today's largest cosmic ray detector is the Pierre Auger observatory (PAO) which was constructed in the Pampa Amarilla in Argentina. It covers an area of 3000 km^2 and provides the largest set of observations of ultra-high energy cosmic rays (UHECR) in history.

A second difficulty in understanding the origin of UHECR should be pointed out: Galactic and extragalactic magnetic fields might alter the direction of even the highest energy events in a way that they do not point back to their source.

In 2007 and 2008, already before the completion of the full detector, the Auger collaboration published a set of three important papers [1, 2, 3]. The first paper dealt with the correlation of the arrival directions of the highest energetic events with the distribution of active galactic nuclei (AGN) closer than 75Mpc from a catalog compiled by Veron-Cetty and Veron (VC-V) [4]. This very bright type of galaxies presumably hosts an active black hole. The correlation was maximal for events above 56 EeV on an angular scale of $\Psi = 3.1^\circ$. This energy threshold roughly coincides with the suppression of the overall energy spectrum above 40 EeV as measured and published by the Auger collaboration in the second paper. If combined, these two measurements support the hypothesis that the aforementioned flux suppression is caused by a drastic energy loss due to reactions of the cosmic rays with photons from the cosmic microwave background (CMB). In the third paper the Auger collaboration reported that the observed cosmic ray data at the highest energies favors a mixed composition of cosmic rays - that is, nuclei contribute to the upper end of the energy spectrum.

In conjunction with these results, the following points were frequently discussed:

- P1:** As stressed in [5], the AGN correlation does not prove that AGN are the sources of UHECR. The AGN might just act as tracers due to their celestial distribution which is correlated with the overall distribution of matter and, hence, maybe with the actual sources of UHECR. Thus, it is merely a proof that the arrival directions of UHECR are not isotropic at a 99% confidence level.
- P2:** The correlation analysis treats all AGN equally, independently of their astronomical properties.
- P3:** The r.m.s. deflection angle of UHECR in a random extragalactic magnetic field is indeed of

the order of a few degrees for protons, but scales with the atomic number Z . Thus, the reported small angular scale $\Psi = 3.1^\circ$ alone might conflict with the previously mentioned heavier composition as indicated in the Pierre Auger Observatory measurements. Furthermore, it is difficult to physically understand the AGN correlation parameters themselves: the proton hypothesis might go along with the observed angular scale, but could contradict the small distance $\approx 75 \text{ Mpc}^1$ to the correlated AGN which, contradictorily, might imply a heavier composition. That is, because protons have a longer energy loss length than light or medium sized nuclei in the intergalactic medium.

P4: The VC-V catalog is not a statistically complete sample of AGN [4].

P5: The correlation study does not realistically model propagation effects such as magnetic deflection or reactions with ambient photon fields. In particular, UHECR masses are not taken into account.

Clearly, to overcome this situation and to conclusively solve the cosmic ray puzzle is an effort which can only be accomplished in a cooperation of many scientist, combining their ideas and abilities. Following this spirit, this thesis aims at contributing to a set of different projects (in various collaborations). Three of these are the main topics of this thesis. All this work was explicitly chosen to advance in answering at least one of the conjectures **P1-P5** as stated above. To emphasize this, all chapters shall be shortly described and connected with the corresponding points **P1-P5**.

In chapter 2, the scan technique which was applied in the aforementioned AGN correlation study by the Auger collaboration was extended to take into account an additional AGN property (**P1** and **P2**). This extended scan technique has been applied to the VC-V radio AGN using the radio luminosity as the fourth scan parameter. Furthermore, a hypothesis test is introduced to monitor the observed possible signal with independent data.

For a realistic modeling (**P5** and **P3**) tools are needed to predict the effects of the propagation of UHE-nuclei - especially their mass loss due to photo disintegration and the deflection in extragalactic magnetic fields. A corresponding public, tool has been developed and is introduced in chapter 3.

In chapter 4, the ongoing work on a catalog of radio and infrared sources is introduced which could be used as an alternative to the VC-V catalog to reduce the problems as addressed in (**P4**).

Beforehand, a short overview on the physics of ultra-high energy cosmic rays will be given in chapter 1. This defines the scientific context of this PhD thesis.

¹If interpreted as caused by energy losses (GZK-like effect) and not by a dilution of the anisotropy due to magnetic deflections.

Contents

Motivation & Preface	3
Nomenclature	7
1. Scientific Context of this Thesis	9
1.1. Cosmic Rays	9
1.2. Overview: AGN	15
1.2.1. Observational Classes and Some Features of AGN	16
1.2.2. The AGN Unification Scheme	20
1.3. Extensive Air Showers	23
1.3.1. Electromagnetic Showers	24
1.3.2. Hadronic Showers	25
1.4. Composition of UHECR	26
1.5. Anisotropy and UHECR Astronomy	29
1.6. The Pierre Auger Observatory	33
2. Source Search Using a Binomial Scan Technique	39
2.1. The Binomial Scan Technique	39
2.2. Extension 1: The Galactic Plane Cut	41
2.3. Extension 2: The Additional Scan Parameter	42
2.4. Four Dimensional Scan Using VC-V Radio AGN	42
2.4.1. Data Set	45
2.4.2. Scan in Radio Luminosity	47
2.5. Penalized Probability	51
2.6. Improvement by the Fourth Scan Parameter?	52
2.7. Effect of Reconstruction Uncertainties	54
2.8. Hide and Seek	55
2.9. Prescription Principles and Suggestions	58
2.9.1. Wald's Sequential Probability Ratio Test	58
2.9.2. The Luminosity Shuffling	64
2.9.3. Rescanning Using an Enlarged Data Set	66
2.10. Status of the Prescription Using the Latest Data Set	68
2.11. The Radio Threshold and Additional Astronomical Properties	71

3. Towards a Model Testing Procedure	77
3.1. A Short Introduction to CRPropa version 1.3	78
3.2. Propagation of Nuclei with CRPropa: A Guideline	78
3.3. Mean Free Path in an Ambient Photon Field.	80
3.4. The Numerical Evaluation	82
3.5. The Photo-Nuclear Cross Sections	83
3.6. Overall Convergence of the Mean Free Path Calculations	85
3.7. The Thinning Options	86
3.8. Propagation Algorithm (Automatic Step Size)	89
3.9. Applications of CRPropa	91
3.9.1. Completeness of the Photo Disintegration Cross Section Data	91
3.9.2. Propagation Matrix and X_{\max} Interpretation	92
4. Towards a Radio and Infrared Catalog of Galaxies	97
4.1. Input Catalogs	98
4.2. Calibration	98
4.3. Preselection	99
4.4. The Raw Catalog	101
Overview of Scientific Results	105
Acknowledgments	107
A. VC-V AGN List	111
B. List of Correlated AGN	119
C. SPRT: Examples with Different p_1 Values	121
D. CMB Photon Number Density	123
E. Photonuclear Cross Sections For Light Nuclei	125
Bibliography	127

Nomenclature

Abbreviations:

AGN	Active Galactic Nuclei
BL Lac	BL Lacertae
BLR	Broad emission Line Region
CDAS	Central Data AcquiSition
CIC	Constant Intensity Cut
CMB	Cosmic Microwave Background
FD	Fluorescence Detector
FR I/II	Faranoff Riley I/II
FSRQ	Flat Spectrum Radio Quasar
GP	Galactic Plane
GPR	Galactic Plane Region
IACT	Imaging Atmospheric Cherenkov Technique
ICRC	International Cosmic Ray Conference
IRB	InfraRed Background
LSS	Large Scale Structure
NED	Nasa Extragalactic Database
NLR	Narrow emission Line Region
PAO	Pierre-Auger Observatory
PD	PhotoDisintegration
QSO	Quasi Stellar Object
SD	Surface Detector
SNR	Super Nova Remnant
SPRT	Sequential-Probability Ratio Test
SSRQ	Steep Spectrum Radio Quasar
UHE	Ultra-High Energy
UHECR	Ultra-High Energy Cosmic Rays
VC-V	Veron-Cetty Veron
VHE	Very-High Energy

Variables:

E, M, A, Z	energy, mass, mass- and atomic number of UHECR
z	redshift (often used as rough distance measure)
Ψ	angular separation between UHECR arrival direction and astronomical object
F	total flux density
L	luminosity
α, δ	right ascension and declination (equatorial coordinate system)
ϕ, θ	azimuth and zenith angle in the site system
l, b	longitude and latitude (galactic coordinates)

Scientific Context of this Thesis

A short introduction to the field of ultra-high energy cosmic ray physics is given in this chapter. It is merely a general overview to introduce the scientific background and context of this work. Further details which directly are a subject to this thesis will be discussed in the corresponding chapters. It should be acknowledged that I benefited a lot from clearly structured and well written publications e.g. [6, 7, 8, 9, 10, 11, 12] while preparing this chapter.

1.1. Cosmic Rays

The cosmic ray phenomenon was discovered by Victor Hess when he measured the intensity of radiation as function of altitude up to 5.3 km in a series of balloon flights. His observations substantiated that the radiation increases above altitudes of 1 km. From his finding, Hess concluded that there must be radiation penetrating Earth from outside the atmosphere [13]. It was Millikan who proposed the name *cosmic rays* in 1925. Victor Hess was rewarded with the Nobel Prize for the discovery of cosmic rays in 1936. Indeed, cosmic rays led to the discovery of e.g. the positron, the muon and the pion before the era of man-made accelerators started. Next to the astrophysical questions, particle physics is still a big motivation for studying cosmic rays. This is because they induce hadronic interactions at energies much higher than what is accessible at accelerator experiments.

Kolhörster, Pierre Auger and others took another major step in understanding the radiation firstly discovered by Hess. They measured the radiation with sets of distant detector stations on ground. They reported time coincidences between the signals in those stations and concluded that they have detected cascades of secondary particles which were initiated by a single cosmic ray particle which interacted in the atmosphere [14, 15]. These particles cascades are called *extensive air showers*, see chapter 1.3 for further explanations.

The energy spectrum of cosmic rays follows a broken power law $dN/dE \propto E^\gamma$ spanning over 11 orders in energy and 30 orders in flux, see figure 1.1. There are four points in energy where the power

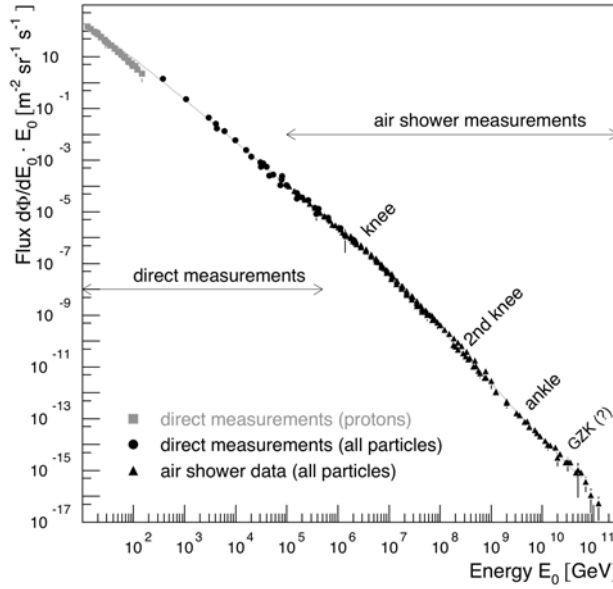


Figure 1.1.: The overall energy spectrum of cosmic rays [6]. At lower energies the region in energy is marked in which the cosmic rays can be measured directly with satellite or balloon experiments. At higher energies the properties of the particles are derived from the air shower they have started in interactions with matter of the atmosphere. The energy spectrum follows a broken power law. The points where the index of the power law presumably changes are labeled as *knee*, *2nd knee*, *ankle* and *GZK(?)*-suppression.

law index γ changes [6, 16]

$$E = \begin{cases} \gamma \approx -2.7 & E \lesssim 4 \text{ PeV} \\ \gamma \approx -3.1 & 4 \text{ PeV} \lesssim E \lesssim 0.4 \text{ EeV} \\ \gamma \approx -3.3 & 0.4 \text{ EeV} \lesssim E \lesssim 4.1 \text{ EeV} \\ \gamma \approx -2.6 & 4.1 \text{ EeV} \lesssim E \lesssim 29 \text{ EeV} \\ \gamma \approx -4.3 & 29 \text{ EeV} \lesssim E. \end{cases} \quad (1.1)$$

They are labeled as: *knee*, *2nd knee*, *ankle* and *GZK(?)*-suppression. To properly match this behavior of the in general featureless cosmic ray spectrum, is a challenge and a plausibility principle for models of cosmic ray acceleration and propagation. Note, the plain fact that the cosmic ray spectrum follows a broken power law already suggests that the cosmic rays do not originate in thermal processes.

At energies of $E \lesssim 10^{14}$ eV, cosmic rays are subject to *direct measurements* with balloon and satellite borne experiments. At higher energies the cosmic ray flux becomes too low. Hence, the secondary particles of the air showers need to be measured at ground or while traversing the atmosphere. From this measurements one has to conclude on the properties of the initial cosmic ray particle. This approach is referred to as *indirect measurement*. Quantities derived in this way are e.g. the energy E , the mass M and the arrival direction of the primary particle, cf. chapter 1.3.

Some cosmic rays at energies below $E \sim 1 - 10$ GeV originate from the Sun. This energy range is not subject to this thesis and hence those cosmic rays will not be discussed. But, it should be noted that the mechanisms of their acceleration might be related with those of particles at the highest energies - the ones considered here. Thus, the Sun is often considered a worthwhile and nearby example

of particle acceleration which might provide clues about similar mechanisms which could produce cosmic rays at the highest energies.

In the recent past, a *standard model* for Galactic cosmic rays seems to evolve: In many papers the Galactic cosmic rays are supposed to originate in supernova remnants (SNR) with their initial spectrum being modified by the propagation inside the Galaxy. The knee is believed to be a result of the charge dependent escape of particles out of the Galaxy. This is because, particles with atomic number Z can be confined by Galactic magnetic fields until the Larmor radius

$$r_L = 1.08 \text{ pc} \frac{(E/\text{PeV})}{Z \cdot (B/\mu\text{G})} \quad (1.2)$$

exceeds the size of our Galaxy¹. Here, B is the Galactic magnetic field strength which is believed to be of the order of $\sim \mu\text{G}$. In this way, iron nuclei would escape from the Galaxy at 26 times higher energy than protons. This model is supported by KASCADE measurements which show hints of this *rigidity dependent* escape of particles: the proton knee is found at energies of 5 PeV [17]. But, an iron knee at 26 times higher energy has not been confirmed yet.

In 1934, Zwicky estimated that three supernovae per century which convert $\sim 10\%$ of their energy output into cosmic ray acceleration can provide enough power to explain the energy density of Galactic cosmic rays $\rho_G = 1 \text{ eV/cm}^3$ [18]. A first model that explained how the energy which is released in supernovae explosions could be used to accelerate particles was proposed by Fermi [19]. Today's scenarios of cosmic ray acceleration are still often founded on his idea: it is believed that matter which is ejected in a cataclysmic event - e.g. a supernova explosion - can create shock fronts that are linked with confined magnetic fields. These shock fronts can be produced e.g. if the ejected matter propagates faster than Alfvén speed² into the intergalactic medium. Charged particles can gain energy if they encounter these shock fronts many times, while in each encounter they are believed to gain a relative energy $\Delta E/E \sim \beta$. Here $\beta = v/c$ is the speed of the shock front. Clearly, this mechanism is a statistical process, as one has to take the probability into account that a particle is not confined by the magnetic fields or is by chance scattered out of the acceleration region e.g. [20, 21, 7]. Modern calculations in which e.g. the interaction of the magnetic fields and the cosmic rays are considered predict cosmic ray energies up to $Z \cdot 10^{17} \text{ eV}$ in supernova remnants [22].

It should be noted that nuclei heavier than iron do not make a large contribution to the Galactic cosmic rays. Furthermore, a comparison of the abundance of elements in the Solar system and in cosmic rays suggests that the two samples are very much alike. In other words, the cosmic rays originate from ordinary matter which was accelerated to higher energies [23].

The acceleration of cosmic rays might also be directly driven by the electromotive force (*one shot acceleration*), e.g. in pulsars. A simple estimation of the maximum energy is derived in [20]: A varying magnetic field \vec{B} induces an electric field \vec{E} according to Maxwell's equation $\nabla \times \vec{E} = -d\vec{B}/dt$. Assuming that the change of the magnetic field develops over a distance L and that it propagates with speed v , one finds $E/L = B/(L/v)$. Integration gives the maximum energy $E_{\max} = Ze \int_0^L E ds = eZBvL$. For the case of pulsars with $B = 10^6 \text{ T}$, $L = 100 \text{ km}$ and $v = c$ an upper limit of $E_{\max} \approx 10^{19} \text{ eV}$ is estimated.

By requiring that the cosmic rays can only be kept in the acceleration region as long as their gyro radius is smaller than the size of the acceleration region L and using a characteristic velocity $v = \beta c$

¹Diameter of the Galaxy is $\sim 30 \text{ kpc}$ with a thickness of $\sim 3.7 \text{ kpc}$

²More precisely, the characteristic speed of the magnetic waves.

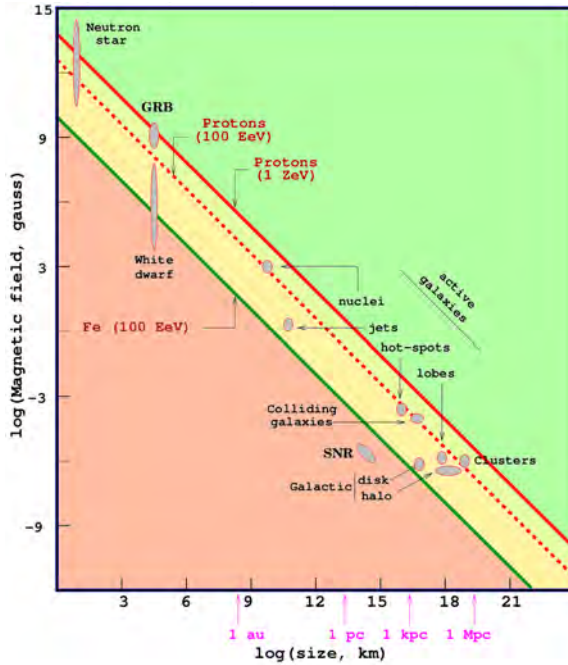


Figure 1.2.: *Hillas diagram* taken from [24]. Possible astrophysical sites of UHECR acceleration of size L and with a magnetic field of strength B which can provide particles up to an energy E_{\max} have to lie above a line in this diagram, cf. equation 1.3. Exemplary, three lines for the case of proton and iron acceleration for different maximum energies and $\beta = 1$ are drawn.

of the scattering centers for the Fermi mechanism, a similar formula for the maximum energy E_{\max} can be derived [25]

$$\left(\frac{E_{\max}}{\text{EeV}} \right) \simeq \frac{1}{2} Z \beta \left(\frac{L}{\text{kpc}} \right) \left(\frac{B}{\mu G} \right). \quad (1.3)$$

This argumentation has firstly been suggested by Hillas and, thus, is often called *Hillas' argument*. Based on this, the ability of some source candidates to accelerate particles to energies above 10^{20} eV are sketched in figure 1.2. Only very few sources seems to meet this requirement, see [24] for further reference. Here, the focus is only on those source candidates which are of importance in the context of this thesis:

- **jets, lobes and hot spots of powerful radio galaxies**

Many galaxies host an active galactic nucleus (AGN) and comprise a very bright class of galaxies, see chapter 1.2 for more details. Some AGN also develop an extended and very luminous radio structure consisting of jets, lobes and hot spots: There is no complete understanding of the development of these phenomena which can have sizes up to $\sim 10 - 100$ kpc for very powerful radio galaxies. In some common scenarios this special morphology is thought to arise from the ejection of plasma from the rotating black hole. The observable radio signature is generated by synchrotron radiation of relativistic electrons which are spiraling in magnetic fields. Probably, electrons become accelerated in the lobes. This is plausible because the synchrotron cooling of the electrons is very efficient and would not allow the electrons to enlight the huge observed volume of the lobes at radio wavelength [12]. This acceleration of electrons could take place in the same process than the acceleration of the UHECR which are of special interest in this

thesis.

E.g. for a hot spot of $L \sim 1\text{ kpc}$, $B \sim \mu\text{G}$ and $\beta = 1$ one finds that the maximum energy is $E_{\max} = 5 \cdot 10^{20}\text{ eV}$.

The author of [26] combined Hillas' argument with assumptions on the magnetic field strength in jets and lobes of radio galaxies and derived a lower limit on the radio luminosity L_{408} at 408 MHz of the sites of UHECR acceleration

$$\left(\frac{L_{408}}{\text{W Hz}^{-1}}\right) > \frac{2.0 \times 10^{24}}{Z^{7/2}} \left(\frac{E}{\text{EeV}}\right)^{7/2} \left(\frac{R}{100\text{kpc}}\right) \quad (1.4)$$

Here, R is the size of the lobe/jet structure. Using $R < 250\text{kpc}$ as the size of the radio lobes, a lower limit of $L_{408} = 2.5 \times 10^{24} \text{ W Hz}^{-1}$ is found for the acceleration of protons ($Z = 1$) to energies above 100 EeV. Only very few, very bright radio sources are known to fulfill this requirement. Indeed, the nearby extended radio galaxy Centaurus A just satisfies this criterion with a luminosity of $L_{408}^{\text{CenA}} = 3 \times 10^{24} \text{ W Hz}^{-1}$. Clearly, if UHECR are charged particles ($Z > 1$) every radio galaxy could be a potential source according to equation 1.4. But, this calculation does not take into account energy losses e.g. by synchrotron radiation or photo disintegration which might strongly constrain the acceleration of nuclei [26]. For more information on UHECR acceleration in radio loud AGN in general, or Centaurus A in especial see e.g. [27, 28, 29, 30, 31, 32], too. It should be acknowledged that the possibility of the acceleration of UHECR in radio galaxies was firstly discussed in [33].

- **active galactic nuclei (AGN)**

Next to the jets or hot spots, the acceleration in the active nucleus ($L \sim \text{mpc}$) is a widely favored site for UHECR acceleration [34]. The energy is provided by accretion of matter in the region of the black hole. For magnetic fields of $B \sim \text{kG}$ an acceleration of protons up to 10^{20}eV might be possible.

UHECR lose energy in the ambient low energy photon fields (e.g. CMB) due to photo meson production or photo disintegration, see section 3.2 for details. The energy loss of nucleons in reactions with CMB photons, mainly by forming the $\Delta^+(1232)$ resonance, was firstly pointed out by Greisen, Zatsepin and Kuzmin and is called *GZK effect* since then [35, 36]. Intensive studies of the *photo disintegration* of UHE-nuclei by excitation of the giant dipole resonance were done in [37]. In addition, energy losses in ambient photon fields due to the conversion of low energy background photons into e^+e^- pairs in the Coulomb field of the charged cosmic rays are expected. There is also an adiabatic energy loss due to the expansion of the Universe. Note, that this so called *redshift loss* is only important for far away source. Additionally, it is independent of the UHECR energy. Hence, it does not alter the shape of the energy spectrum. It turns out that the GZK horizon³ for iron nuclei and protons are similar while lighter and medium nuclei lose their energy faster [11]⁴. These energy losses restrict the volume of potential UHECR sources to a volume of $\sim 100 - 200\text{Mpc}$. The exact value of the GZK-horizon depends on the composition and the injection spectrum of UHECR at the source, the source distribution itself and the Galactic and extragalactic magnetic fields.

Shortly summarized, the aforementioned energy losses “act as a filter to nearby sources minimizing directional ambiguities from too many sources” [9]. Furthermore, the trajectories of the highest energy cosmic rays are the ones which are less effected by deflections in magnetic fields. These two circumstances might allow for UHECR astronomy, cf. section 1.5.

³Strictly speaking the term GZK-horizon might be misleading because the flux suppression could be caused by photo disintegration reactions in case of UHE nuclei.

⁴This follows from simulations of UHECR energies $E > 6 \cdot 10^{19}\text{eV}$ and assuming an uniform source distribution.

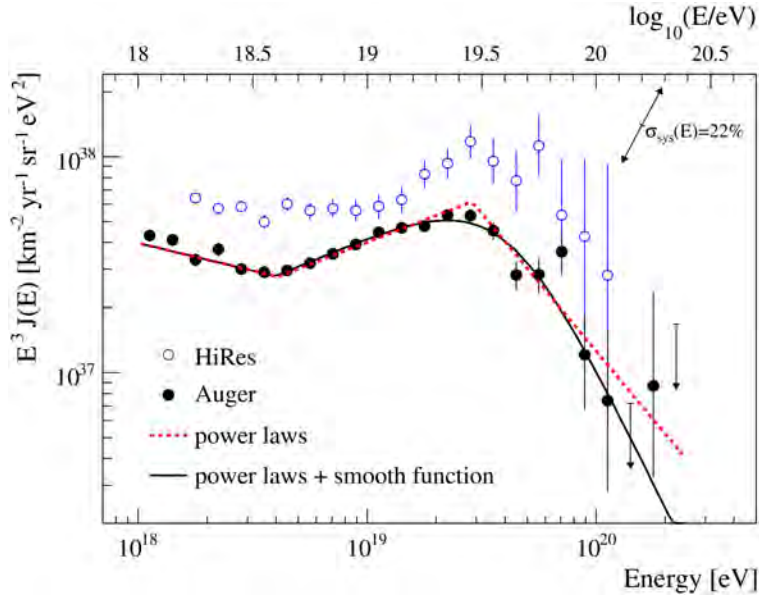


Figure 1.3.: Combined Auger spectrum using hybrid and surface array data in comparison with HiRes stereo data [39]. The plot holds the fits of a strict and a smoothed power law function [16]. The flux has been weighted with E^3 . This weighting will assign the systematic energy uncertainty of 22% to the flux axis. To account for this, the uncertainty is implied with the rotated error bar in the upper right.

Clearly, energy losses also occur in the acceleration region and not only during the propagation through the inter galactic medium, too. Thus, a drawback of the UHECR generation e.g. in the core of AGN is the fast energy loss in the high field density near the core of the AGN which restricts the maximum energy [38]. This is less of a problem e.g. in the radio jets where the medium is thinner and the expected energy losses are comparably smaller.

Assuming that the sources of cosmic rays can provide UHECR with sufficient energies, photo meson production and/or photo disintegration reactions with background photons should cause a suppression of the flux of UHECR. Such a feature is observed in the Auger and HiRes energy spectra, cf. figure 1.3, and is detected with a high statistical significance[16, 39]. But, it might be that this drop in the flux is just an imprint of UHECR accelerators that run out of power. Both Auger and HiRes incorporate the measurement of the complete air shower profile in the atmosphere in their energy spectrum⁵. A spectrum that is based only on the particles that can still be detected on the ground is the one of the AGASA collaboration. This spectrum does not show the suppression feature which might be explained by a systematic shift of the energy reconstruction. Anyway, these circumstances inspired the development of so called *non-acceleration* or *top down* models. Herein, UHECR originate in the decays or the annihilation of *exotic* and super-heavy particles. The most of those models are linked with a high fraction of photons and thus seem to be disfavored by measured upper limits of UHE-photons, see section 1.4. For a review on non acceleration models see e.g. [40].

There are three popular models which try to explain the shape of the spectrum of UHECR at the highest energies: the *dip*, the *mixed* and the *ankle* model. Herein, the shape of the spectrum is a result

⁵Note, that the shift in the flux of the Auger and HiRes spectra can be compensated if one applies a systematic energy shift of 25% to one of the measurements [11].

of the energy loss processes discussed before. This paragraph follows a summary which was given in [8]. All of these models assume that the higher end of the spectrum $E \gtrsim 10^{18}$ eV is of extragalactic origin. This is plausible as the arrival directions of these particles should be barely affected by Galactic magnetic deflections and should point back to their potential Galactic origin. The Galactic cosmic rays are modeled as suggested in [41]. The extra galactic cosmic ray spectrum is modeled as function of only three parameters: the spectral index of the source spectrum, the maximum CR energy at the source E_{cut} and an overall normalization constant. In [8] the evolution of sources as function of the redshift z is neglected.

- **dip model**

In the dip model all UHCER are assumed to be protons. In particular, the ankle feature is an accumulation of protons due to the energy loss by pair production. Indeed, this is the reason for the restriction to protons; for higher atomic numbers Z the position of the ankle induced by pair-production would be shifted, as this energy loss length - for a fixed Lorentz factor - scales proportional with Z^2 , cf. equation 3.4. Furthermore, the dip model predicts the 2nd knee at 0.1 EeV as a consequence of the transition from galactic to extra galactic cosmic rays.

- **mixed composition model**

As already stated by its name, this model allows for UHE-nuclei. The abundance at the source is assumed to be equal to the one observed in Galactic cosmic rays at lower energies. As in the case of the dip model, the mixed composition model can describe the data well but predicts the transition from galactic to extra galactic cosmic rays to take place at somewhat higher energies $E_{\text{th}} = 1$ EeV.

- **ankle model**

Here, the transition point to the extra galactic component of a pure proton spectrum was fixed in the ankle region. As a consequence, this requires that the Galactic cosmic rays reach up to energies of several EeV which would require modifications of the rigidity dependent knee model as discussed above.

It should be pointed out that a proper model of the UHECR creation and propagation should not only describe the energy spectrum data well. It should rather be able to correctly predict all observables. Hence, future parameters to distinguish models is the predicted composition of UHECR or even more challenging the distribution of UHECR arrival directions.

1.2. Overview: AGN

A very luminous class of galaxies are *active galactic nuclei* (AGN). As they play an important role in the context of this thesis, a short introduction to this type of galaxies will be given. This includes some aspects of their unique spectral features as well as their rich morphology. To do so, this section will mainly summarize important information from the corresponding chapter 26 of [12]⁶ and follows its useful structure. Additional information for this chapter has been taken from [42, 27]. A very recent summary article is [43].

⁶Only information that is not taken from [12] will be explicitly cited.

1.2.1. Observational Classes and Some Features of AGN

In the beginning of their exploration, the spectra of AGN have roughly been sketched by a power law (index $\alpha \sim 0.5 - 2$). The fact that one observes power law like shaped spectra implies a non thermal origin of the observed radiation presumably by synchrotron radiation of relativistic electrons. On top of the very luminous *continuum spectrum*, some spectra of AGN show a blue bump - due to a thermal component, too. At lower frequencies the plasma becomes opaque to its own synchrotron radiation which causes the so called *turnover* in the spectra (*synchrotron self-absorption*).

Today, astronomers can observe the spectra of AGN over more than fifteen orders of magnitude in frequency - from radio up to TeV. Of course, the spectral energy distribution (SED) of AGN shows more features on top of the oversimplified power law behavior. Indeed, the finer structures in the SED contain important information on the processes that create the observable radiation as well as the physical and chemical environment of the AGN. AGN are subdivided into different astronomical classes as they show remarkable differences in observables like e.g. redshift, time variability, type and width of the emission line in their spectra. These emission lines originate in photoionization processes powered by light from the continuum spectrum. Some observable differences which are a basis for the separation of AGN into the astronomical classes will be shortly addressed in this subsection.

Seyfert 1/2

Seyfert galaxies comprises only 10% of all galaxies but 90% among the AGN themselves. About 90% of the known Seyfert cores reside in *spiral galaxies*. Although Seyfert galaxies are very abundant in our cosmological vicinity their source of energy could not yet be fully resolved. Many of the Seyfert galaxies are located close to another galaxy with which they gravitationally interact. This interaction might be linked with a change of the overall torque which could allow matter to encounter the galaxy's center. The corresponding higher density could be a basis for the galaxies activity e.g. an enhanced *star formation* rate or by feeding a mass accrediting black hole.

Seyfert galaxies can be further classified using the emission lines in their spectra. These lines can be divided by their width into *broad* and *narrow* ones. Next to the expected *permitted* lines one can also find *forbidden* lines - the latter only means that the corresponding transitions only occur with a very low probability. Note, the broadening of the lines is an effect of fast random motion of the light emitting atoms (Doppler effect). From the existence or non existences of forbidden lines, one can explore the density of the material: If the density is too high, the forbidden transitions will not occur as the atoms would preferably deexcite in collisions. If the density is too low, there are just not enough atoms to produce the very unlikely forbidden transitions often enough. Those Seyfert galaxies which only have narrow lines (allowed and forbidden) are called *Seyfert 2* (S2) galaxies. In comparison, *Seyfert 1* (S1) galaxies only have broad allowed and forbidden lines. There are intermediate states in the Seyfert classification (e.g. S1.2) if a galaxy shows both broad and narrow permitted lines. In general, Seyfert 1 type galaxies are usually more luminous and more X-rays are measured. Indeed, a X-ray component linked with Seyfert 2 galaxies seems to exists but may be absorbed by a high matter density in the line of sight. It is noteworthy that the luminosity of the broad lines have been observed to vary by a factor or ~ 2 sometimes even on time scales of days. This is not the case for the narrow lines which indicates that both types of lines originate from somewhat different regions in the AGN. This and the fact that the *polarized* spectrum of Seyfert 2 galaxies show features of a Seyfert 1 galaxies were two important observations that led to the development of the *AGN unification scheme*, cf. section 1.2.2.

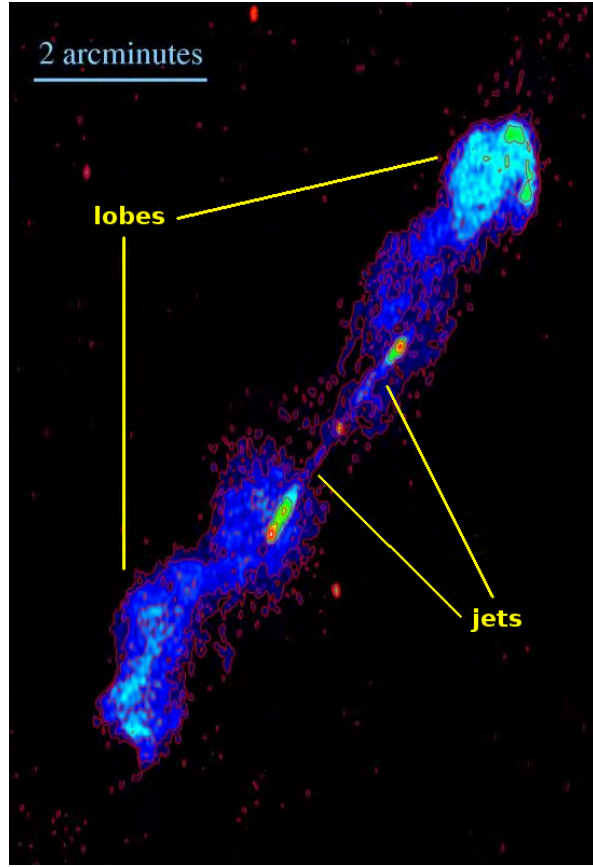


Figure 1.4.: Picture of the giant radio galaxy B1545-321 at wavelength of 13 cm. The galaxy itself is located in the center of the picture. Labels have been added to point out the location of the narrow jets and the giant radio lobes which extend over a distance of 460 kpc (1.5 million light years). Picture taken by L. Saripalli, R. Subrahmanyam and Udaya Shankar using the Australia Telescope Compact Array (ATCA), from [44].

Radio Galaxies (FR I/II)

Some AGN show a radio component in their spectrum which is $\sim 10^3 - 10^4$ times stronger than what is observed in Seyfert cores. Indeed, often this immense radio luminosity does not emerge from the AGN core itself, but from huge radio structures in the vicinity of the AGN - e.g. the so called narrow *radio jets* or the huge, “cloudlike” *radio lobes*, cf. section 1.2.2 and figure 1.4. Due to these structures, radio galaxies are morphologically very different from Seyfert galaxies. On the other hand, like in the case of the Seyfert galaxies, the cores of radio galaxies are more luminous compared with the “normal” majority of dim galaxies. Furthermore, radio galaxies show emission lines and, can further be subdivided into NLRG/BLRG if they show narrow/broad emission lines, respectively. Radio galaxies are usually found at larger redshifts and are mostly hosted in elliptical galaxies Historically, radio galaxies have often been classified as suggested by Fanaroff and Riley [45]. They defined two subclasses *FR I* and *FR II* in terms of the ratio $R = \Delta H / \Delta S$ of the distance ΔH between the two most luminous radio spots on both sides of the host galaxy and the overall radio

extension ΔS of the galaxy

$$\text{FR classification} = \begin{cases} \text{I} & : R < 0.5 \\ \text{II} & : R > 0.5. \end{cases} \quad (1.5)$$

Fanaroff and Riley reported that the two classes are sharply separated at a luminosity of $L \sim 2 \cdot 10^{25} \text{ W Hz}^{-1} \text{ sr}^{-1}$ at a wavelength of 178 MHz. Herein, the type II galaxies are the ones often linked with higher radio luminosities. Furthermore, FR I galaxies often seem to have two jets (*jet domination*) and weak emission lines in contrast to the *lobe dominated* FR II galaxies with strong emission lines which mostly only show one jet [27]. FR I are usually located in rich clusters of galaxies while FR II are often isolated or in poor clusters [27].

QSOs, Quasars (FFQR, SSQR)

Quasi stellar objects (*QSOs*) are an optically very luminous type of AGN which initially appeared stellar due to their very large distances (redshifts up to $z = 6$). Most of the QSOs show an excess in ultraviolet wavelength in their spectra which are up to 10^5 times brighter than the spectra of galaxies without an AGN core. Although many QSOs show broad forbidden and permitted emission lines like Seyfert 1, there are nearly no examples of QSOs with narrow lined Seyfert 2 like spectra. In 10% of the cases there is a radio signal linked with the QSO. These sources are also called quasi stellar radio objects, *quasars* for short. Sometimes, quasars become further subdivided in flat- (*FSRQ*) and steep spectrum (*SSRQ*) radio quasars. Usually, QSOs show only a very low polarization of less than 3%. For redshifts $z < 2$, there are indications that QSOs undergo an evolution of being more luminous in the past. It seems that QSOs are often accompanied by a neighboring galaxy - another similarity with Seyfert galaxies.

BL Lacertae objects

Class of AGN showing highly polarized (40-60%) and variable spectra. The luminosity of BL Lacertae objects can alter by a factor 100 with short term variations up to 30% within 1 day. They show only very weak or no emission lines at all - a major difference if compared to QSOs - and are mostly observed at large redshift. 90% of all resolved BL Lacertae objects reside in elliptical galaxies.

The class of *blazars* summarizes those BL Lacertae objects and quasars which are highly polarized in optical wavelengths with additional high brightness variability.

A major new insight into the physics of AGN became possible with the installation of ground based telescopes applying the imaging atmospheric Cherenkov technique (IACT) like HESS, MAGIC and VERITAS, see e.g. [47] for an overview. The basic idea is that very-high energetic (VHE) photons in the TeV range can induce particle cascades by alternating e^+/e^- pair production and photon creation in the atmosphere - cf. section 1.3. These charged leptons travel faster than the speed of light in the air and thus emit Cherenkov light. This light can be measured and allows to draw conclusion about the primary, incident TeV-photon. Up to date 46, extragalactic sources have been detected which emit VHE-photons with energies $E_\gamma > 100 \text{ GeV}$. They are displayed in figure 1.5. Thus, the IACT allows astronomers to perform multiwavelength campaigns from radio frequencies up to the TeV regime. Indeed, this remarkable enhancement in the astronomical observation is of importance for the field of UHECR physics. This can be outlined with the quasar 3C279 with a redshift of $z = 0.536$ whose

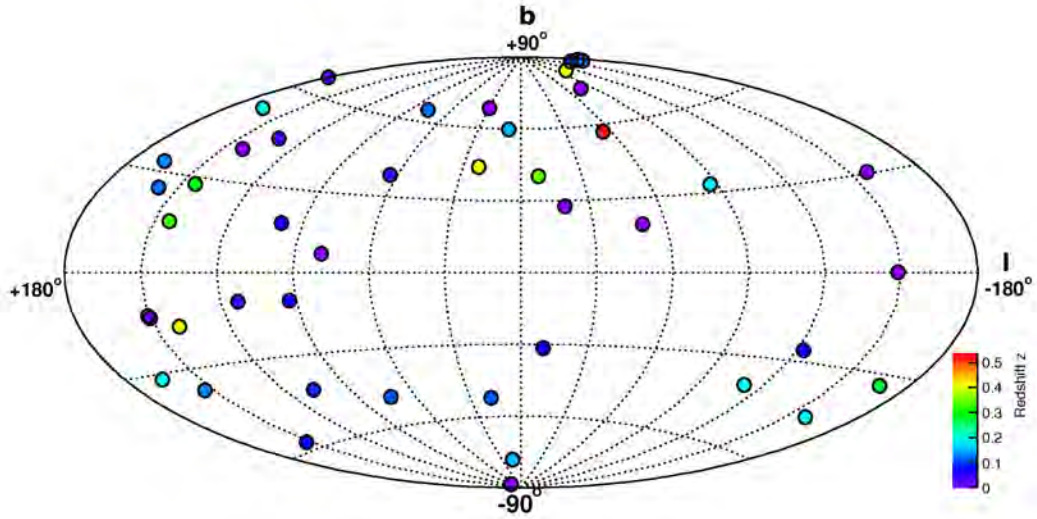


Figure 1.5.: Skymap of the 46 known extragalactic sources (points) of observed gamma rays with energies $E_\gamma > 100 \text{ GeV}$ [46]. The positions are given in galactic coordinates l, b . The redshift of the sources is colorcoded.

TeV-photon emission was detected by MAGIC in February 2006 [48]. The measured spectral energy distribution of 3C279 - including the MAGIC measurements - is best described using a hadronic model which includes the presences of protons with energies up to 10^{18} eV [49]. They produce the TeV component either directly via proton synchrotron radiation or indirectly by synchrotron radiation of muons created in proton- γ reactions in the source. Although, the energies of these protons do not reach up to 100 EeV this is an indication that hadrons can become accelerated in AGN. Anyway, the large distance to this special galaxy does note make it a good source candidate for observable UHECR due to expected energy losses during propagation to Earth. It should be noted, that relativistic jet activity on $\sim \text{pc}$ scales has been confirmed in 3C279 during 1991-1997 [50].

If indeed ultra-high energetic protons or nuclei are existent in blazars, they might leave the host galaxy. During the subsequent propagation in the extragalactic space they can indirectly induce UHE-photons in reactions with the low energy photon background via pair production or photo production of mesons such as fast decaying neutral pions ($\pi^0 \rightarrow \gamma\gamma$) - note, the latter is the GZK reaction again. The direct search for these UHE-photons is discussed in more detail in section 1.3. The UHE photons can dissipate their energy by creating electromagnetic cascades providing a component of TeV photons. Note, that TeV photons might be directly created in these distant blazars, but would probably be absorbed in the extra galactic background light before reaching Earth. Indeed, it has been reported that spectra of distant blazars can be well fitted with a spectrum that mainly consists of secondary photons cascades induced by photo meson- and pair production of protons propagating through the extragalactic space [51]. This model is further supported by the indication that far away blazars show less time variability in their TeV component than nearby ones. Thus, one presumably observes TeV emission from different processes or regions. The implication is that the variable component might be induced directly inside the AGN, the non-variable one during the propagation of emitted UHECR to Earth.

1.2.2. The AGN Unification Scheme

Today, many astronomers believe that the AGN classes which were roughly sketched in the previous section might all be linked with the same fundamental phenomena - a matter accreting black hole within a galaxy. Different angles of observations with respect to the galaxy's disk linked with different obscuration by the host galaxy's matter might be the reason for the various appearances of AGN leading to the diversity of astronomical classes. Furthermore, the level of "activity" might be connected with the rate of mass accretion or the mass of the black hole. This concept of a general picture of AGN is referred to as the *AGN unification scheme*. The main observations which led astronomers to this unified description of AGN are:

- All classes of AGN - except from BL Lacertae objects - show the same linear dependency $L_{H\alpha} \propto L_{FC}$ between the amount of radiation $L_{H\alpha}$ found in the $H\alpha$ line and the continuum luminosity L_{FC} , e.g. figure 2 in [52]. This is a remarkable similarity which is pointing to a common underlying phenomenon which is independent of the AGN class.
- Starting with an observation by Antonucci et al. [53], many Seyfert 2 galaxies have been found that comprise features of Seyfert 1 galaxies - namely, broad emission lines - if the measurements were restricted to polarized light. Thus, a Seyfert 2 galaxy might have a Seyfert 1 core which is just observed through a torus of matter of the hosting galaxy. In addition, the narrow lines of galaxies seem to have a weaker time variability than their broad counterparts, which indicates a different origin of these two kinds of emission lines.
- From the rapid time variability of the luminosities of some AGN an upper limit on the size of the emission region $s \sim 1$ AU of AGN was derived by purely geometrical reasoning. A lower limit on the mass of the emission region $M > 3.3 \cdot 10^8 M_{Sun}$ of quasars can be derived using the Eddington luminosity limit. Here, M_{Sun} is the mass of the Sun. This huge mass on such a limited space already hints that a black hole might be involved. Note, that a black hole with a Schwarzschild radius of \sim AU is expected to have a similar mass.

In the AGN unification scheme the central black hole is the engine of the AGN. Three processes are often discussed to explain the generation of energy in connection with a black hole.

- Release of gravitational **potential energy** by the rotating black hole which is accreting the surrounding matter. The luminosity which is linked with this process can be written as $L = \eta \dot{M} c^2$ where $\dot{M} c^2$ is the rest mass accretion rate and $5.32\% < \eta < 42.3\%$ is the degree of efficiency of the energy conversion.
- Rotational energy from the **spin** of the black hole could be converted into particle energy by the *Blandford-Zjaneck* mechanism: in a descriptive manner one can think of the black hole as a rotating conductor in a magnetic field. A potential difference is generated between the equator and the poles of the black hole which might be a source of kinetic energy for charged particles.
- Conversion of **magnetic field energy** into kinetic energy of particles: Simplified, the central black hole accretes a huge amount of matter and the confined magnetic fields. Caused by the rotation of the black hole, the magnetic field lines can become compressed and twisted (relativistic *frame dragging / Lense-Thirring effect*). Roughly, if field lines with opposite polarization *touch* (cf. *magnetic reconnection* in the Sun), the magnetic field energy might be released and transformed into kinetic energy of the plasma [20].

The aforementioned mechanisms to gain energy from a black hole require the presence of matter to be accreted or to provide the plasma that is linked with the needed magnetic fields. This fact is taken

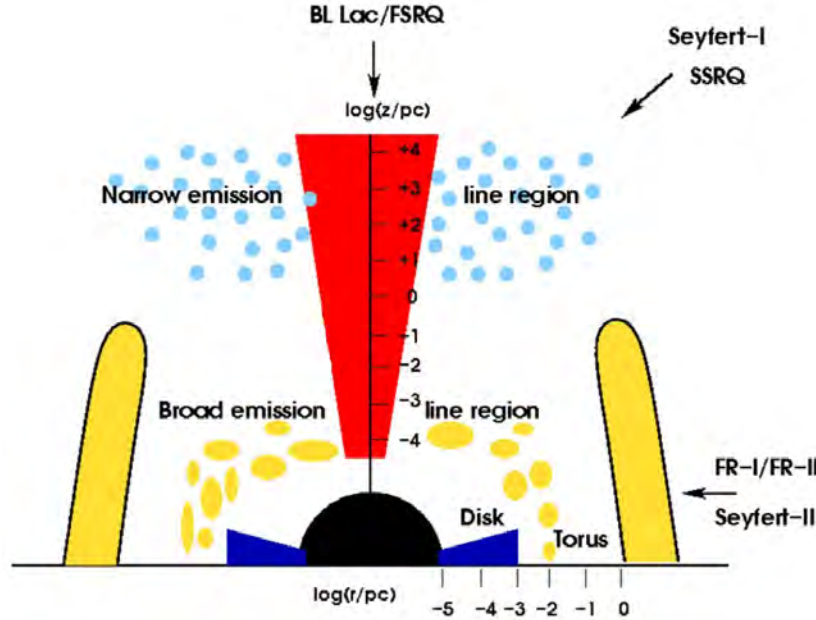


Figure 1.6.: Graphical adaption of the AGN unification scheme. Slightly modified from [54]. See text for explanation.

care of in many unification models by imposing an accumulation of matter in the vicinity of the black hole, the so called *accretion disk*. See figure 1.6 for a graphical representation of the AGN unification scheme that will be further explained and motivated in this section. The temperature of the disk roughly follows $T_{\text{disk}} = M^{-1/4}$ with e.g. $T_{\text{disk}} = 10^5 \text{ K}$ in case of a "normal" QSO. Note, that the corresponding thermal black body spectrum would peak at a wavelength that coincides with the blue bump which is a main characteristic for many QSOs. Surely, next to this thermal component, an additional non thermal component is needed to explain the width of the observed continuum spectrum of these objects. It is expected that the final shape of the disk depends on the fraction $f = L_{\text{disk}}/L_{\text{Edd}}$ of the disk's luminosity L_{disk} in terms of the Eddington luminosity L_{Edd} : for small f (small radiation pressure) gravitation will compress the matter into a small, dense volume (torus). In case of very luminous disks, $f > 1$, the dominant radiation pressure might produce a more extended *radiation torus* or thin disk. Exemplary values are $0.01 < f < 0.1$ for Seyfert galaxies and $f \sim 1$ for luminous QSOs.

Next to the disk, the *broad line region* (BLR) is located - the origin of the broad emission lines. Its temperature is of the order of $T_{\text{BLR}} \sim 10^4 \text{ K}$. Clues about the size of the BLR again follow from the time variability of the assigned emission lines. Restrictions on the matter density follow from the non existence of forbidden lines: On the one hand forbidden transitions will not occur due to the low probability of their excitation in case of low densities. On the other hand, the atoms will preferably deexcite in collisions if the matter density is high. It is believed that only 1% of the volume of the BLR is filled with matter which is preferably clumpy.

The BLR is surrounded by a opaque bulk of matter referred to as the *torus* which would obscure an observer's view with a line of sight close to the disk of the host galaxy of the AGN. The torus has mainly been included to the unification scheme to explain the observable differences and similarities between Seyfert galaxies of type 1 and 2. Both classes are intrinsically the same phenomenon just

seen under different angles and, hence, through different layers of obscuring matter - the torus.

Finally, at larger distances from the black hole, the *narrow line region* (NLR) as origin of the permitted and forbidden narrow lines has been inserted in the model. To allow for forbidden lines, the number density of the electrons is believed to be lower than in the BLR. In spite of that difference, the temperature of $T_{\text{NLR}} = 10^4 \text{ K}$ is similar to T_{BLR} and the consistency presumably is clumpy as in the case of the BLR. There are indications (namely a blue shift) that the NLR is moving away from the galactic center probably due to radiation pressure.

So far the previously described unification scheme does not include the radio luminosity or morphology of radio loud AGN. Indeed, these observational facts can be included in the model, too. The energy source for the formation of the huge radio structures again is the "black hole engine" of the AGN. Driven by the central engine, relativistic particles, plasma and confined magnetic fields could be ejected from the center of the AGN. This matter ejection is the basis of the creation of the jets. Their narrow and well collimated structure might be due to funneling effects by the disk that surrounds the black hole. Furthermore, the jet might be collimated by a sustentative magnetic field configuration. During their voyage, relativistic electrons spiral around the magnetic field lines to create the measurable radio signal via synchrotron radiation. If the stream of matter hits the intergalactic medium or remnants from previous ejections, shock waves could be produced which may be identified with the observed *hot spots* in the jets of some AGN. While the charged particles propagate further into the extragalactic space they continuously cool down via synchrotron radiation until they fill the huge volume of the huge *radio lobes*. These are a major source of the tremendous most luminous radio signals. The sheer size of the lobes is well illustrated by noting that - if we could see radio wavelength by eye - the radio lobes of some galaxies, which appear almost point like to us, would have a size comparable to that of the moon. It is often assumed that the kinetic and magnetic energy in the jet/lobes are approximately equal - that might cause a stability of these phenomena on longer time scales. And thus one encounters a major key point why jets and lobes of radio galaxies are a frequently discussed in context with UHECR acceleration in the literature: the electrons would lose their energy due to synchrotron radiation on time scales of $\sim 10^4 \text{ yr}$ - clearly, not enough time to fill the huge observed volume of the lobes. This is a strong indication that the electrons become re-accelerated in the lobes. This may, or may not be due to a Fermi like acceleration mechanism. In any case, if this acceleration is driven by the electromagnetic force, do ionized and charged nuclei also couple to this mechanism and become accelerated to ultra-high energies?

BL Lac and FSRQ enters the unification scheme of figure 1.6 if radio loud AGN are looked at along the jet directly into the radio loud core. The interpretation of the emission from the BLR/NLR does not change for the radio galaxies. Finally, the FR I/II galaxies are extended radio galaxies seen from the side where the lobes and jets might be resolved.

The unification scheme might also implicate a picture of the evolution of galaxies



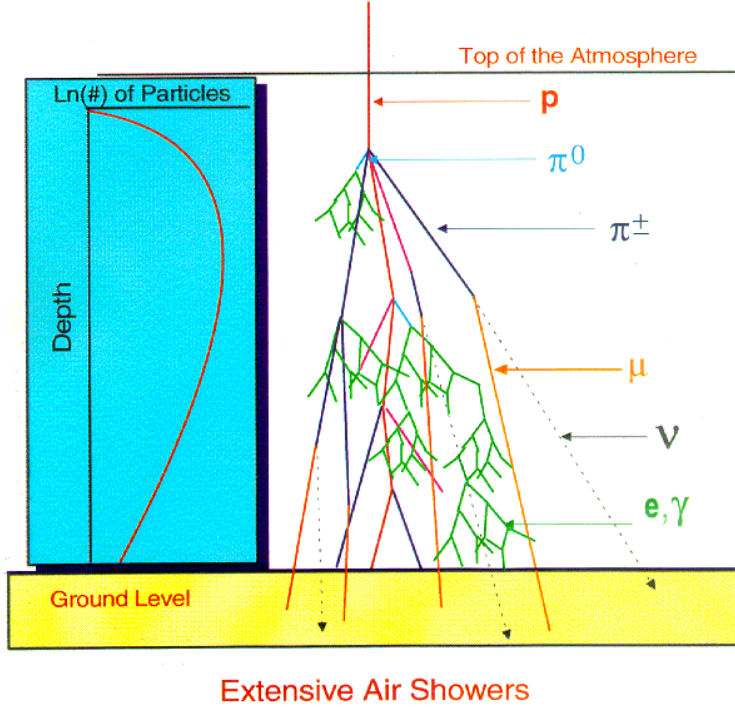


Figure 1.7.: A diagram of the propagation of an extensive air shower showing the particles produced [55].

1.3. Extensive Air Showers

At the very-highest energies, the flux of cosmic rays is so low that indirect measurements have to be used for their detection. In this case, the primary particle's properties are estimated from the features and development of the cascade of secondary particles which is induced in reactions with the Earth's atmosphere. These cascades of particles are called *extensive air showers*. Depending on e.g. the mass M , energy E and azimuth θ of the primary particle, different air showers might develop which in turn give clues on the primary particle. A sketch of an extensive air shower is given figure 1.7. The origin of the shown particle content will be further explained in the following sections.

The detection of air showers can be done by using the footprint of the secondary particles on ground. These can extend up to many km^2 - depending on the particles energy E . Thus, time delays between distant detector stations on ground and their signal strength can be used to reconstruct air showers. Alternatively, one can measure the induced fluorescence light profile of the air shower which is produced while its cascade of secondary particles propagates through the atmosphere. The fluorescence light is linked to the de-excitation of nitrogen molecules which were previously excited by the secondary particles from the air shower. Recently, it is studied if the radio signal caused by the *geo-synchrotron* radiation of the secondary electrons can be used to study the profile of air showers in the atmosphere, too [56]. The interpretation of measured air shower data with respect to e.g. the energy E and mass M of the primary particle is done by comparing the shower development to predictions from simulations. This is difficult especially at ultra-high energies as the multiplicity and the cross section of the particle's early interactions are not accessible at today's man-made accelerators. Hence, models of

ultra-high energy particle reactions are mainly an extrapolation from available measurements at lower energies. This introduces a model dependent systematic uncertainty. This exceptionally effects the prediction of the first interaction which are the seed for the overall shower development that follows. On top of that, as a direct consequence of the probability interpretation in quantum mechanics, so called *shower to shower fluctuations* are introduced. For example, assuming a mean free path λ for the first interaction of a primary particle with Earth's atmosphere, then the point of the first interaction can be sampled from an exponential $\exp(-X/\lambda)$ where X is the atmospheric depth. Due to this, two identical primary particles can produce somewhat different looking air showers.

The detailed modeling of the air shower development is not subject to this thesis. Thus, only two oversimplified models of electromagnetic and hadronic air showers will be discussed here which at least allow for a qualitative understanding of air shower physics. These explanations are based on [6, 7].

1.3.1. Electromagnetic Showers

Air showers that are induced by electrons⁷ or photons are called *electromagnetic* showers. They are mainly driven by particle production due to alternating pair productions and bremsstrahlung reactions. At lower energy E_c the electrons will start to lose energy due to ionization which is described by the Bethe-Bloch formula - and no longer via bremsstrahlung. This will cause the particle production to stop as the photons which are linked with the ionization do not have enough energy to create new electron-positron pairs. Hence, at an average electron energy E_c , the air shower will start to thin out.

This interplay between bremsstrahlung and pair production inspired Heitler's toy model for electromagnetic cascades: It is assumed that the number of particles $N = 2^n$ is doubled after each interaction length λ . Here, n is the number of already propagated interaction lengths. The energy of the particles for the n^{th} generation is supposed to be equally divided among the created particles and one yields $E_n = E/2^n$. The n^{th} generation of particles are linked with a atmospheric depth $X = n\lambda$. The maximum number of secondary particles N_{\max} is reached when a significant number of particles have a critical energy E_c . The corresponding atmospheric depth of the shower maximum is abbreviated as X_{\max} . From this simple equations one can derive two important qualitative statements about electromagnetic cascades

$$N_{\max} = \frac{E}{E_c}, \quad (1.6)$$

$$X_{\max}^{\text{em}} = \lambda_{\text{em}} \log_2\left(\frac{E}{E_c}\right). \quad (1.7)$$

Assuming that the cross sections for bremsstrahlung and pair production (called *approximation A*) as well as the one for ionization losses (referred to as *approximation B*) are independent of the energy, analytical formulas for the development of electromagnetic cascades were given by e.g. Rossi and Greisen [57, 58]. Furthermore, Nihimura, Kamata and Greisen also derived an approximate formula - called NKG formula - for the lateral spread of an electromagnetic shower due to Coulomb scattering of electrons[59, 60]. But, this formulas only provide numbers "averaged" over the shower to shower fluctuations. Furthermore the assumption of a constant cross section is only valid at the highest energies. Thus, it is common to use predictions derived by full Monte Carlo simulations our days.

⁷In what follows this also includes positrons.

1.3.2. Hadronic Showers

Air showers induced by nucleons or nuclei are called *hadronic showers*. In a simple model, the primary particle creates n_{tot} secondary particles - mostly charged and uncharged pions in a ratio of ~ 2 . This is because pions are an Isospin triplet of the strong interaction. The uncharged pions immediately decay into photons $\pi^0 \rightarrow \gamma + \gamma$ which in turn induce electromagnetic sub showers, as discussed in the previous section. The charged pions are assumed to undergo further hadronic interactions with Earth's atmosphere until they reach an energy E_d below which they mainly decay into muons and neutrinos. Thus new pions can only be produced until the energy per particle drops below E_d which gives an expression for the number n of hadronic particle generations $E_d = E_0 / (n_{\text{tot}})^n$. Using this equation and the identity written as $1 = n \ln(n_{\text{ch}}) / \ln(n_{\text{tot}}) = n \ln(n_{\text{tot}}) / \ln(n_{\text{tot}})$ and assuming that every charged pion creates one muon, one finds

$$N_\mu^{\text{had}} = (n_{\text{ch}})^n = \left(\frac{E}{E_d} \right)^\alpha \quad (1.8)$$

where $\alpha = \ln(n_{\text{ch}}) / \ln(n_{\text{tot}}) = 0.85 \dots 0.92$ and n_c is the number of charged pions out of n_{tot} . Note, that the number of muons is roughly proportional to the initial energy. The free parameters of this simple model can be calibrated with simulations as has been done in [61].

Due to the aforementioned Isospin symmetry in each new generation 2/3 of the initial energy is transferred into the hadronic component of the shower - mainly into charged pions. Thus the hadronic energy E after the n^{th} interaction length is $E_{\text{had}} = (2/3)^n E_0$. The remaining energy $E_{\text{em}} = E_0 - E_{\text{had}}$ is sent to the electromagnetic component. From this one can learn that already after a small number of generations a lot of energy is into the electromagnetic cascade. E.g., for a primary particle of 10^{20} eV more than 90% of the initial energy will end up in the electromagnetic cascade [62].

In a simple approximation, the shower maximum $X_{\text{max}}^{\text{had}}$ of the hadronic shower equals the one from a corresponding purely electromagnetic shower but is shifted by the hadronic interaction lengths λ_{had} . Furthermore the energy of the particle that induces the corresponding electromagnetic sub showers is of the order of $\sim E/n_{\text{tot}}$

$$X_{\text{max}}^{\text{had}}(E) \sim \lambda_{\text{had}} + X_{\text{max}}^{\text{em}} \left(\frac{E}{n_{\text{tot}}} \right). \quad (1.9)$$

Note, that $X_{\text{max}}^{\text{em}}(E)$ is given in equation 1.7.

If it comes to the development of air showers initiated by a nucleus, one can think of the nucleus with mass number A as a superposition of A nucleons with an energy E/A . First of all, the substitution $E' = E/A$ will not alter the number of particles in the shower maximum $N_{\text{max}}^{\text{em}} = N_{\text{max}}^{\text{had},A}$. This is because the total amount of energy E for particle production is the same - it is just divided among many nucleons. Nevertheless, one finds an altered estimations for the muon number N_μ^A and the depth of the shower maximum for nuclei X_{max}

$$N_\mu^A \approx A^{1-\alpha} N_\mu^{\text{had}}, \quad (1.10)$$

$$X_{\text{max}} \approx X_{\text{max}}^{\text{had}} \left(\frac{E}{A} \right) = X_{\text{max}}^{\text{had}}(E) - \lambda_{\text{em}} \log_2 A. \quad (1.11)$$

These formulas emphasize that X_{\max} and N_μ are useful variables to derive the composition of UHECRs from air shower measurements. Note, that this superposition model also suggests that nuclei have smaller shower to shower fluctuations by a factor

$$\text{RMS}(X_{\max}) \sim 1/\sqrt{A} \quad (1.12)$$

if compared to protons. Although this is only a rough estimation, $\text{RMS}(X_{\max})$ is a useful composition indicator.

The electromagnetic part of an air shower will convert its energy faster than the hadronic component. E.g., 1000 g/cm² of atmosphere roughly corresponds to 27 electromagnetic radiation lengths but only to 11 hadronic interaction lengths.

Showers with a different point of first interaction or different X_{\max} values will also be observed at different stages of their development. Thus, a shower induced earlier in the atmosphere will have a nearly planar shower front at ground if compared to a shower which started closer to the surface. Similar geometrical considerations suggest a slower signal rise time for deeper penetrating showers e.g. in the surface array of the Pierre Auger observatory [63], cf. section 1.6. Here, the rise time is just the time needed for the integral over the signal to e.g. raise from 10% to 50% as in the case of [64]. That is why the rise time τ and the shower front curvature r_c are often used composition sensitive quantities.

It should be noted that neutrinos can induce air showers, too - although this will only happen very rarely. It happens if UHE-neutrinos create hadron which are accompanied by a lepton (charged current) or a neutrino (neutral current). The leptonic channel is the main channel for neutrino detectors as e.g. IceCube. The hadrons will induce “normal” air showers. But, due to the very low cross section of the weak interaction which is involved here, this can take place very deep in the atmosphere or even inside the Earth and the corresponding air shower can be vertical or even up going (but still having an electromagnetic cascade). Thus, air shower observations have and will be used to search for neutrinos or to set upper limits on UHE-neutrino fluxes, too.

1.4. Composition of UHECR

A recent measurement of the composition of UHECR has been published by the Pierre Auger collaboration [65]. It is motivated by the qualitative behavior of air showers as given in the equations 1.12 and 1.11. In short: protons will have larger X_{\max} values than nuclei and have larger shower to shower fluctuations $\text{RMS}(X_{\max})$. The results are shown in figure 1.8. It is based on observations of longitudinal air shower profiles using the fluorescence telescopes from the Pierre Auger observatory. The averaged X_{\max} values and the corresponding $\text{RMS}(X_{\max})$ values are compared with the expectation values of iron and proton simulations. Both plots show a trend to heavier nuclei at the highest energies. Using Hillas’ argument, as stated above, this is not unreasonable. Heavy nuclei might longer be kept in the acceleration region than protons and, hence, are accelerated up to higher energies. Of course, this is only a hand waving argument: modeling the sources and the acceleration of cosmic rays has to take into account the effects of synchrotron radiation and the disintegration of nuclei in reactions with the photon and hydrogen gas in the accelerator region.

It should be noted that a similar measurement by the HiRes collaboration was presented at the ICRC in 2009 which tends to give larger X_{\max} values for increasing energy hinting a lighter composition, cf. [66].

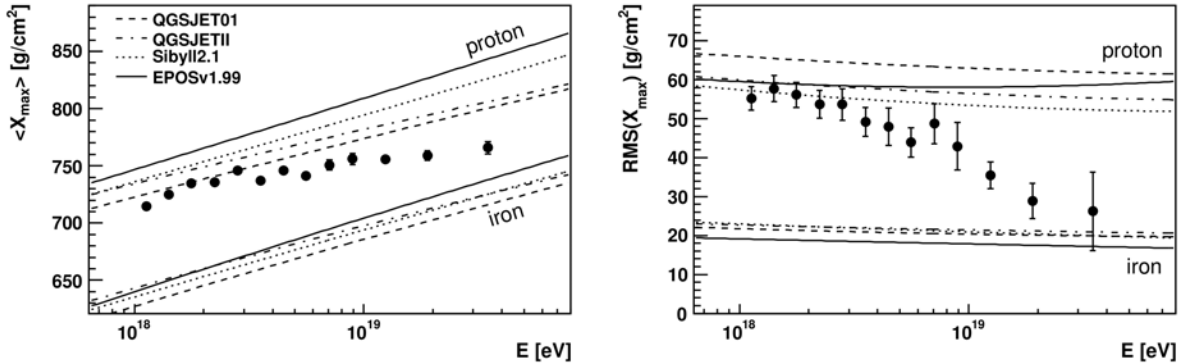


Figure 1.8.: X_{\max} and $\text{RMS}(X_{\max})$ observations from the measurement of longitudinal shower profiles with the fluorescence telescopes of the Pierre Auger observatory (points) [65]. Additionally, predictions made with different Monte Carlo tools are given.

Historically, only electrically charged particles are summarized as cosmic rays. It is an important question to understand if neutral particles like neutrinos ν and photons γ contribute to the cosmic ray spectrum. An expected link between UHECR and neutrinos as well as photons can be shortly outlined in context with the so called *multimessenger connection*, see [54] for further details: UHE protons can induce the following particle reactions in ambient photon field ($p\gamma \rightarrow \Delta^+ \rightarrow p\pi^0$ or $n\pi^+$) or hydrogen gas ($pp \rightarrow NN + n\pi^{0,\pm}$). Here, N is a nucleon and n_π is the multiplicity of the pion production⁸. The p-p collisions are more likely to happen in the denser source region itself due to the expected presence of hydrogen gas. The excitation of the delta resonance in the extragalactic low energy background light (CMB and IRB) is the main energy loss during propagation in the extragalactic space (GZK effect) but also happens in the acceleration region itself. A closer look at the sums of the isospin in the photo pion reaction and calculation of the corresponding Clebsch Gordan coefficients reveal that 66% of neutral π^0 and 33% of positively charged pions π^+ are expected. In case of neutrons, one would expect the same type of reaction which would cause the creation of negatively charged pions π^- - due to charge conservation. In case of the proton-proton collisions the ratio of π^0, π^+, π^- is 1:1:1 for large multiplicities, that is high energies, due to isospin conservation. Note, charge conservation introduces a suppression of π^- for smaller multiplicities n_π at lower energies. The neutral pions decay into photons ($\pi^0 \rightarrow \gamma\gamma$). They are called GZK photons if they originate in reactions with extragalactic background photon fields during propagation. These photons can also produce electromagnetic cascades in alternating e^+e^- pair production and inverse Compton scattering processes with the low energy background photons⁹. These electromagnetic cascades have already been discussed in context with the TeV photon emission from distant blazars, cf. section 1.2.1. In case of media which are reasonably thin, the charged pions will decay into neutrinos via

$$\pi^+ \rightarrow \mu^+ \nu_\mu \rightarrow e^+ \nu_e \bar{\nu}_\mu \nu_\mu \quad \text{and} \quad \pi^- \rightarrow \mu^- \bar{\nu}_\mu \rightarrow e^- \bar{\nu}_e \nu_\mu \bar{\nu}_\mu. \quad (1.13)$$

Hence, assuming that positively and negatively charged pions are produced with the same rate, the ratio of e, μ, τ neutrinos and anti neutrinos are expected to be 1:2:0 - no τ neutrinos from the source or during propagation. However, due to neutrino flavor oscillation a ratio of 1:1:1 is expected for propagation distances larger than the size of the solar system [54].

⁸At high energies, the production of heavier mesons, such as Kaons, is possible in both of these reactions.

⁹Note, leptons that originate from pair production of photons in the Coulomb field of the proton will induce electromagnetic cascades, too. Hence, pair production is source for some UHE photons, too.

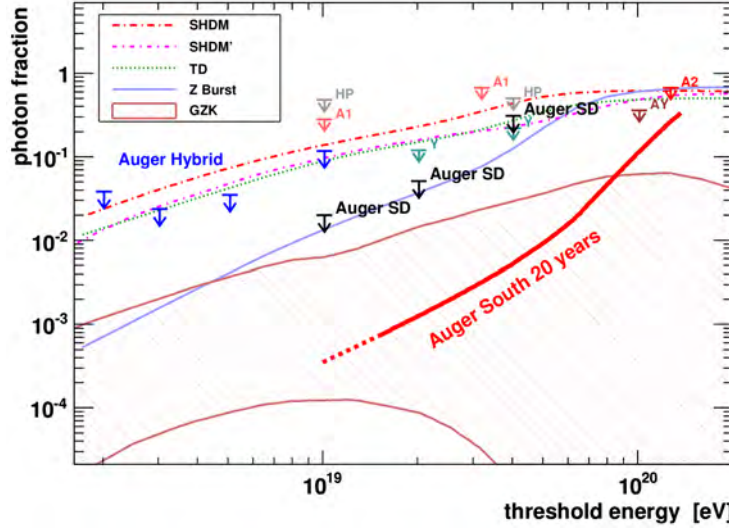


Figure 1.9.: Compilation of recent upper limits on the fraction of UHE photons as function of their threshold energy. A line showing the expected sensitivity of the Auger south observatory after 20 years of operation is given (thick black line). The expected photon fractions for some models are shown, too. [67].

UHE-nuclei with mass number A can create secondary UHE neutrinos and photons in the same reactions if the nuclei's energy is approximately higher by a factor of A . This is because the energy per nucleon E/A corresponds to the energy of a single UHE-nucleon energy in this case. Correspondingly, the onset of pion production on one nucleon from a nucleus is shifted to higher energies. In this way, a heavier composition would e.g. reduce the expected number of neutrinos.

These simple considerations predict a link between UHE-nucleons and nuclei, photons and neutrinos and is the basis for the so called *multi messenger* approach. That is, a possible cosmic ray source might also be linked with neutrino or photon observations in different energy regimes. Thus, the complete multimessenger picture of a source, including neutrino and photon observations, might help to reveal the mechanism of UHECR acceleration.

Air showers which are induced by UHE-photons are mainly electromagnetic and hence have only very few muons. Furthermore, they have a deeper shower maximum X_{\max} if compared to nuclei. The different development and particle content of photon induced air showers also effect observables like the *radius of curvature* of the shower front r_c or the so called *signal rise time* $\tau_{1/2}$. For the modeling of photon air showers two additional physical effects have to be taken into account: photons can start a “prematurely” electromagnetic cascade due to a pair production outside the atmosphere. Here, the momentum is conserved by an interactions with a photon from Earth’s magnetic field. The second effect that occurs is the *LPM effect* [68, 69]. Qualitatively, it is an interference effect that happens if at high energies the distance between the interaction targets is of the order of the interaction length. This can cause “multiple” scattering which suppresses the cross section of Bremsstrahlung and pair production and leads to a deeper X_{\max} .

Until now, no photons at the highest energies have been found. Figure 1.9 summarizes some upper limits on the diffusive UHE photon fraction. Today’s most constraining limits come from the Pierre Auger observatory using observations of the longitudinal shower profile up to 10^{19} eV and r_c , $\tau_{1/2}$ measurements with the surface array at higher energies. It is noteworthy that the presented photon

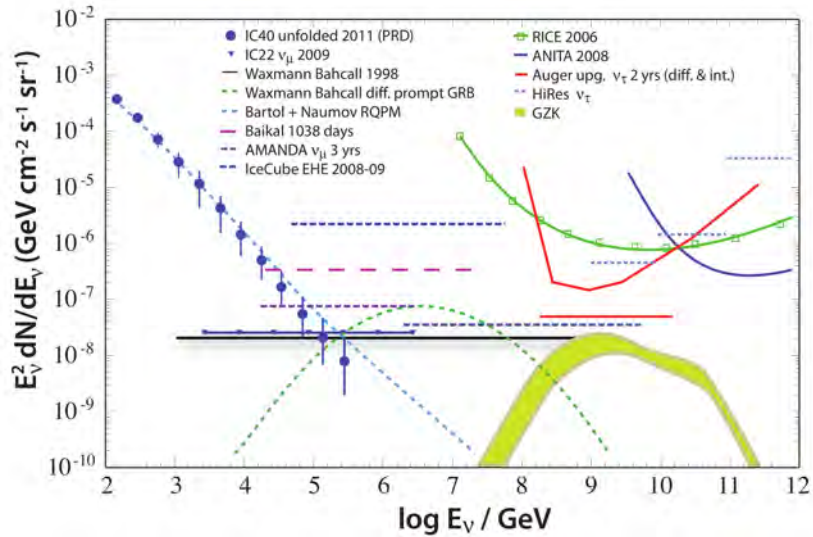


Figure 1.10.: Collection of diffusive upper limits on the flux of neutrinos, originally from [9] and modified with data from [70, 71] by [72]. Additionally, some flux predictions are given e.g. due the modeling of the GZK-effect. The measured and expected neutrino background is shown, too.

limits already rule out some top down models which usually predict a huge fraction of photons. But still, the sensitivity is too low to test for the photons which are expected due to the GZK effect.

A collection of recent diffusive neutrino flux limits is shown in figure 1.10. At lower energies the measured atmospheric neutrino flux is given which acts as background for neutrino telescopes like IceCube. But at higher energies neutrinos from non thermal processes in astrophysical source might become dominant as they presumably are linked with a harder energy spectrum. At the highest energies neutrino flux predictions are given for “cosmogenic” neutrinos which originate in GZK reactions. It is noteworthy that current upper limits are already close to become sensitive enough to restrict model predictions.

Indeed, a diffusive neutrino flux might be observed in case of dim, far away sources. In this case it might not help that neutrinos directly point back to their sources. This is different for UHE photons which can only reach Earth from very nearby sources due to fast energy losses in reactions with ambient background photons.

1.5. Anisotropy and UHECR Astronomy

A main issue for cosmic ray astronomy are deflections of the charged UHECR in Galactic and extra-galactic magnetic fields which have a strength of the order of $\sim \mu G$ and $\sim nG$, respectively¹⁰. Thus, the directional information which could hint the source of the UHECR might be lost. Unfortunately, magnetic deflections are less of a problem only for primary particles at the highest energies where the available data set is the smallest. On the plus side, if a GZK-like suppression exists, it will act as a filter to very nearby sources at the highest energies, too.

¹⁰It should be noted that measurements and predictions of extragalactic and Galactic magnetic field strength is subject to very-high uncertainties. For a review of magnetic fields and cosmic rays see e.g. [74]

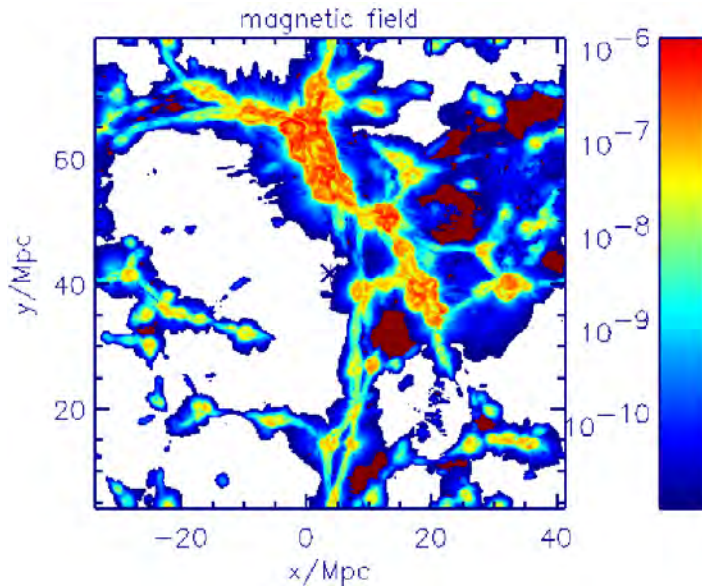


Figure 1.11.: Two dimensional cross section of a three dimensional, large scale structure, extragalactic magnetic field simulation. The magnetic field strength in units of Gauss is color coded. Taken from [73].

The r.m.s. angular deflection $\bar{\Psi}$ of a UHECR with charge Z and energy E over a propagation distance d in a random magnetic field with r.m.s. strength B and coherence length λ can be parametrized as [75]

$$\bar{\Psi} = 0.8^\circ Z \left(\frac{E}{100 \text{ EeV}} \right)^{-1} \left(\frac{d}{10 \text{ Mpc}} \right)^{1/2} \left(\frac{\lambda}{\text{Mpc}} \right)^{1/2} \left(\frac{B}{\text{nG}} \right). \quad (1.14)$$

For a particle traveling with the speed of light, this deflection is linked with an average propagation time delay $\bar{\Delta}\tau$ if compared with the propagation on a straight line to the observer [75]

$$\bar{\Delta}\tau = 1.5 \cdot 10^3 Z^2 \left(\frac{E}{100 \text{ EeV}} \right)^{-2} \left(\frac{d}{10 \text{ Mpc}} \right)^2 \left(\frac{\lambda}{\text{Mpc}} \right) \left(\frac{B}{\text{nG}} \right)^2 \text{ yr}. \quad (1.15)$$

These formulas do not take into account the energy- and mass losses which occur during the propagation of the UHECR to Earth. The assumption of a random magnetic field is presumably another oversimplification. Indeed, large scale structure (LSS) cosmological simulations suggest that the extragalactic magnetic fields are linked with the distribution of matter and hence are inhomogeneous in our Galactic neighborhood up to distances of the GZK horizon. This is illustrated in figure 1.11. In dependency of the position of the UHECR sources and the observer in such a highly structured magnetic field environment, the arrival direction, propagation time, composition and spectrum of UHECR may be strongly affected and modified. This is one major reason to provide a public, numerical tool to study the propagation of UHECR nuclei in 3D large scale structure simulations, as discussed in chapter 3.

Many analyses were presented in the past that studied possible anisotropies in the UHECR arrival directions, for instance: The AGASA collaboration reported a clustering of events above 40 EeV on an angular scale of 2.5° in an auto correlation study [76]. This observation could not be confirmed by HiRes data [77]. The HiRes collaboration e.g. claimed a correlation of their events with energies above

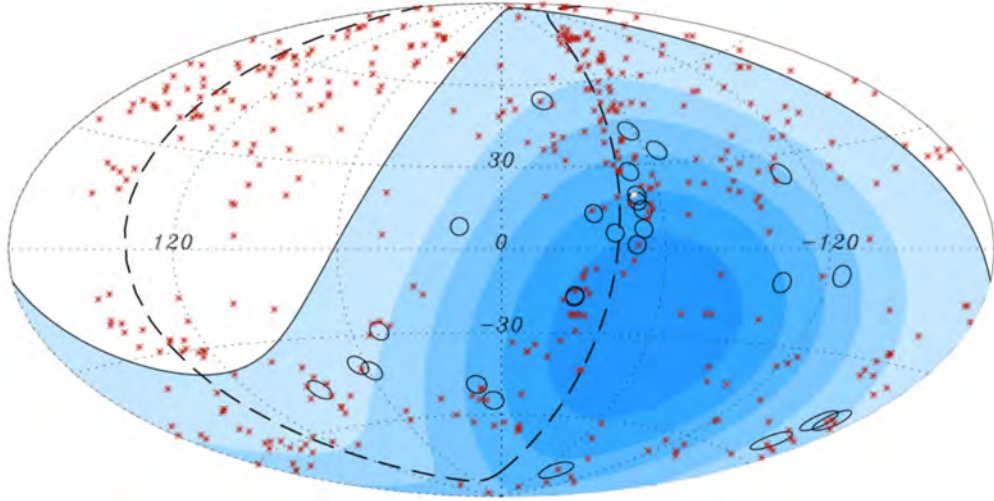


Figure 1.12.: Arrival directions of UHECR data (circles) and positions of AGN (stars) from the VC-V catalog within the correlation parameters as prescribed by the Pierre Auger collaboration [5]. The relative exposure of the Pierre Auger observatory is marked in shades of blue.

10^{19} eV with BL Lacertae objects from the Veron-Cetty Veron catalog on the northern hemisphere for angular scales of 0.8° . Using observations of the southern hemisphere, the Pierre Auger collaboration could not support this finding [78]. Many similar results on the anisotropy of UHECR have been published in the past, but none of them could be verified by a second and independent observation. An independent confirmation is crucial, as there are a lot of statistical pitfalls hidden in these studies, e.g. multiple trials by using different astronomical catalogs, analysis approaches and selection criteria.

An observation of anisotropy (99% confidence interval) which was confirmed with an independent data set was published by the Pierre Auger collaboration [5]. A maximal discrepancy from anisotropy was found in the arrival directions of UHECR with energies above 56 EeV with respect to the position of AGN with a maximum redshift $z = 0.018$ on an angular scale of 3.1° . These parameters were found in an optimization procedure after which 12 out of 15 events correlated with a VC-V AGN. In a second step these parameters were fixed and the hypothesis of isotropy was tested with a new and independent data set: 6 out of the 8 following events verified the correlation in a statistical test which was fixed a priori. The Pierre Auger collaboration pointed out that this correlation does not prove that AGN are actual sources of UHECR - any class of objects that follow the same mass distribution in the sky could create a similar signal. The resulting skymap of the events and AGN selected by the prescribed parameters are shown in figure 1.12. These findings and some of the consequences will be discussed in more detail in the next chapter. Here, it should just be noted that the HiRes collaboration could not find a correlation of their data with VC-V AGN applying the parameters prescribed by the Pierre Auger collaboration [79]. A reason for that might be a shift in the reconstructed UHECR energy by 25% - there is no correlation at 40 EeV in the Auger data, too. Furthermore, the HiRes experiment has less statistics at the energies of interest. In general, aiming for a comparison of Auger and HiRes results, one should always keep in mind that these two experiments observe different hemispheres of the sky, and might see a somewhat different UHECR picture due to that.

For a larger dataset up to December, 31th 2009, the Pierre Auger collaboration reported a decreased correlation fraction of $38^{+7}_{-6}\%$, with 21% expected in case of an isotropic distribution [80].

As already stated, the onset of anisotropy at energies similar to the one where a flux suppression

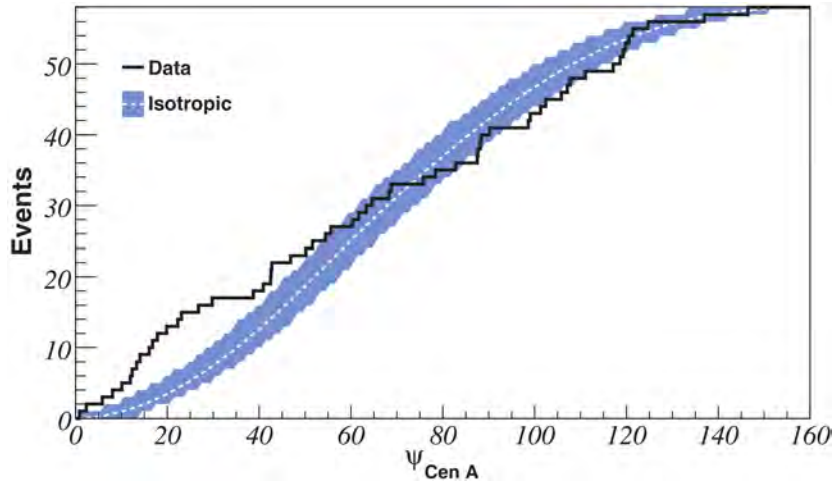


Figure 1.13.: Cross correlation function of Auger data above 57 EeV with the position of Centaurus A. The blue area corresponds to the 68% confidence interval in case of isotropy [82].

appears in the energy spectrum is a noteworthy indication for the existence of a GZK-like effect.

Applying equation 1.14 and 1.15 using $E = 56$ EeV and $d = 75$ Mpc in a random magnetic field of r.m.s. strength $B = 1$ nG and a coherence length $\lambda = 1$ Mpc, one finds an angular deflection $\bar{\Psi}$ of the order of some degrees and a time delay of $\sim 3 \cdot 10^5$ yr for protons. The angular separation is in a reasonable agreement with the correlation parameters as stated by the Pierre Auger collaboration. But, problematic might be the fact that the elongation rate suggest that UHECR at the highest energies are nuclei, cf. figure 1.8. In this case, e.g. for iron the expected deflection of equation 1.14 would be by a factor of $Z = 26$ larger and not in the range of the angular window size $\Psi = 3.1^\circ$. Furthermore, it follows from UHECR propagation simulations, that the 99%-GZK sphere of protons with $E > 60$ EeV is probably $\sim 250 - 300$ Mpc and therefore larger than the 75 Mpc which is implied by the results of the Pierre Auger collaboration [11]. Among others, these simple considerations point out a possible disagreement which has been widely discussed in the UHECR community. To conclude on this, a more complex modeling of UHE-nuclei propagation and deflection in realistic extragalactic large scale matter- and magnetic field structures is needed. This can partly be achieved with the CRPropa framework, cf. section 3.

It has been criticized that the Pierre Auger collaboration treated all types of AGN equally and did not take into account their special morphology [42]. Although, this does not weaken the key point of rejection of UHECR-isotropy, taking into account astronomical features of the AGN in correlation studies could be the key for identifying the real sources of UHECR. In this context, studies that discuss a correlation of the Pierre Auger Observatory data with a sample of radio galaxies should be mentioned, e.g. [81, 42].

Among the VC-V AGN which correlate with the Auger UHECR data is Centaurus A, the huge radio galaxy closest to Earth (distance ~ 3.4 Mpc). It might be an especially interesting source candidate as can be seen in figure 1.13 which shows the cross correlation function with the UHECR Auger data. As can be seen the departure from isotropy is maximal for a circular angular window of 18° in which 12 events can be found while only 2.7 are expected in case of isotropy. But, of course there are more potential sources in this region which could be considered as the true UHECR sources. Thus, an alignment of event directions along major axis is an interesting feature [83]. Note, Centaurus A has



Figure 1.14.: On the left, a schematic view of the Pierre Auger Observatory in April, 2009. All surface stations (blue points) in the green area were deployed at this time. The right picture shows one surface detector station in the field with a fluorescence telescope building in the back.

also been discovered to be a source of very-high energy gamma rays by HESS [84].

1.6. The Pierre Auger Observatory

Is there a GZK suppression as measured by the HiRes collaboration, or not - as reported by the AGASA experiment? This aforementioned controversy clearly needed to be answered. A main problem was the understanding of the systematic uncertainties in both measurements and how they compare; while the AGASA experiment was a ground array and measured the secondary particles that reaches Earth, HiRes uses fluorescence telescopes to measure the fluorescence light track of an air shower using the atmosphere as a huge calorimeter. Clearly, both detection techniques go along with assets and drawbacks: Measuring the complete shower profile gives a very good estimation of the primary energy especially at the highest energies. This is because a lot of the primary particle's energy is led into the electromagnetic part of the air shower which in turn creates the observable fluorescence light itself. But of course, the telescopes can only measure in clear dark nights and the "active volume" in which they are sensitive to different sets of showers has to be determined with simulations in order to calculate fluxes. Indeed, this is a challenging task as this simulations strongly depends e.g. on the varying properties of the atmosphere, clouds, aerosols and the excitation reactions that generates the fluorescence light. In case of a ground array the acceptance for the air shower detection can be calculated geometrically for energies above which the detector is fully efficient. Furthermore, those arrays can in principle have a duty cycle of 100%. Unfortunately, one can only observe the footprint of particles on the ground, which can be a mixture of particles from the muonic and electromagnetic parts. This introduces a stronger dependency on the hadronic interaction models which are linked with large uncertainties.

Thus in 1991, Jim Cronin and Alan Watson suggested a detector which benefits from the assets of both detection techniques: a ground array with a manageable acceptance providing huge statistics with an energy calibration based on telescope measurements. Clearly, a good concept to answer the

aforementioned controversy introduced by AGASA and HiRes. Additionally, their plans included two detector sites to allow full sky observations - one in the northern and one in the southern hemisphere.

The concept of Cronin and Watson led to the construction of the Pierre Auger observatory in the province Mendoza near the city of Malargüe in Argentina ($35.1^\circ - 35.5^\circ$ S, $69.0^\circ - 69.6^\circ$ W, 1400 m a.s.l.). The ground array is formed by 1600 ground stations positioned on a triangular grid covering an area of 3000 km^2 . The site is surrounded by 24 fluorescence telescopes which are mounted in 4 buildings each surveying 180° degree in azimuth and 30° in elevation. A scheme of the surface detector array in April 2009 is shown in 1.14(a). A picture showing one of the ground stations and a telescope building is given in figure 1.14(b). Next to its conceptual innovation the Pierre Auger Observatory exceeds former experiments in size. A measure to compare the capability of an air shower experiment is the exposure which is the product of area \times solid angle \times observation time. The data set used in this thesis already corresponds to an exposure of $21758 \text{ km}^2 \cdot \text{sr} \cdot \text{y}$.

The construction of the Pierre Auger observatory with its two complementary detector components started the so called *hybrid era* of air shower detection.

Each of the 24 fluorescence telescopes is equipped with 440 hexagonal photomultiplier tubes (PMTs) with a viewing angle of 1.5° . An example of an air shower measurement as seen by one of the telescopes is given in figure 1.15(a). The shower detector plane, which is fixed by the shower axis and the telescope's position, can be estimated by finding the line along the maximum charge among the triggered PMTs in the camera.

In a very good approximation, the air shower propagates with the speed of light c through the atmosphere. Thus, a nearby shower will pass the field of view faster than a far away one. Hence, the angular speed $\dot{\chi}(t)$ of the air shower in the shower detector plane and a simple geometrical treatment allows one to find the direction of the shower axis

$$t_i = t_0 - \frac{R_p}{c} \tan\left(\frac{\chi_0 - \chi_i}{2}\right). \quad (1.16)$$

Here, R_p is the closest distance to the shower axis at time t_0 , cf. figure 1.16. An example of a fit of this function to a shower profile is given in figure 1.15(b).

Once the shower axis is known, the measured light flux can be corrected for the effects of attenuation in the atmosphere. In this way the energy emitted by the air shower can be determined and converted into the number of particles as function of atmospheric depth X . The energy loss per slant depth dE/dX as function of the atmospheric depth X - the so called shower profile- is shown for an exemplary air shower in figure 1.15(c). Usually, the empirically formula found by Gaisser and Hillas

$$N(X) = N_{\max} \left(\frac{X - X_0}{X_{\max} - X_0} \right)^{(X_{\max} - X)/\lambda} \exp\left(-\frac{X_{\max} - X}{\lambda}\right) \quad (1.17)$$

is fitted to the observed shower profiles [86]. Herein, X_0 is the point of the first interaction which is linked to a mean free path λ . The integral over the Gaisser Hillas profile is used as a measure for the energy E of an air shower $E = \alpha \int N(X) dX = \int dX dE/dX$ with $\alpha \approx 2.2 \text{ MeV/g/cm}^2$ [7].

The reconstruction of the shower geometry can be significantly improved by adding the timing information of the tank with the strongest signal to the geometry fit of equation 1.16. This is called a *hybrid* reconstruction. The hybrid angular resolution of the Pierre Auger observatory has been found to be 0.5° at the highest energies ($E > 3 \text{ EeV}$) [87]. The major contributions to the hybrid energy uncertainty are the fluorescence yield (14%), the calibration of the PMTs (10%), and reconstruction uncertainties (10%). After applying quality cuts, approximately 7% of all showers can be reconstructed in hybrid mode.

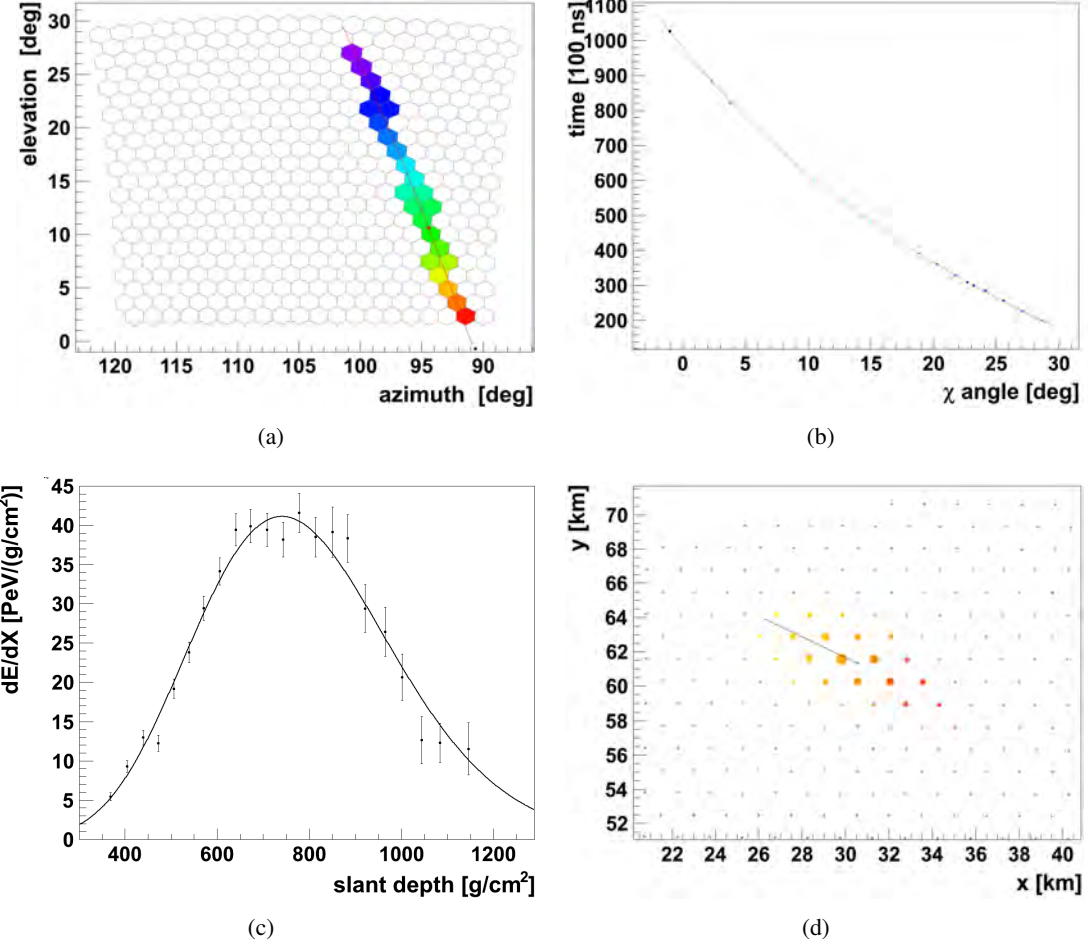


Figure 1.15.: Example event as measured by the Pierre Auger collaboration.

- (a) Picture of an air shower as seen by one telescope of the Pierre Auger observatory. The triggered pixels are marked whereupon the color hints the time ordering of the pixels. The orientation of the shower detector plane is indicated with a red line.
- (b) Observation angle of the air shower as function of time. The red line corresponds to the geometry fit of equation 1.16.
- (c) Reconstructed shower profile with Gaisser Hillas fit, cf. equation 1.17.
- (d) Footprint of an air shower as observed in the surface detector of the Pierre Auger detector. Again, the color indicates the time ordering of the triggered stations. The sizes of the circles illustrate the relative signal strength in the tanks. Black dots mark the position of not triggered surface detector stations.

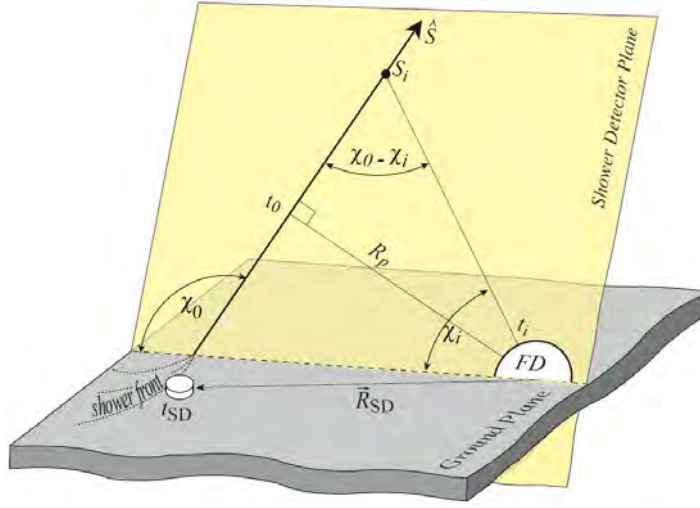


Figure 1.16.: Definition and illustration of the quantities used for the hybrid reconstruction [85].

Each of the 1600 ground stations of the surface array is equipped with three PMTs and filled with 12 m^3 of extremely clean water. In this case, the light used to observe particles in the tank is caused by the Cherenkov effect. A charged particle which moves in a medium can induce light due to polarization effects. If the particle additionally moves faster than the speed of light in the medium, this polarization light can sum up coherently and create a light cone - the so called Cherenkov cone. If many neighbored tanks measure one air shower in coincidence, the trigger time difference can be used to reconstruct the direction of the shower front. The shower axis is perpendicular on the shower front. An example of a footprint of an air shower as observed by the ground array of the Pierre Auger observatory is shown in figure 1.15(d).

The communication between the stations and the data acquisition system is done via a radio connection. The needed electrical power is supplied by solar panels and is charged in a set of batteries. Only signals with at least three stations triggered within $100\mu\text{s}$ are further analyzed. Approximately, 3 events/day are expected above 3 EeV where the detector becomes fully efficient. The angular resolution is found to be better than 1° for energies above 40 EeV which is an important energy threshold for the analysis presented in chapter 2 of this work [87].

The energy of the ground array measurement is calibrated to the hybrid energy using air showers which are independently reconstructed in both detector systems applying the *constant intensity cut* (CIC) method, that is [88]: Reconstruct the signal strength S_{1000} at 1000 m distance to the shower core. It is important to note that the value of S_{1000} is approximately proportional to the energy of the initial cosmic ray [89] - this holds nearly independently of the cosmic ray's mass. Thus, if all cosmic rays showers would arrive with the same zenith angle θ at Earth, one could simply derive their energy from the measured S_{1000} using the hybrid energy and the aforementioned proportionality. Of course, cosmic rays do not arrive with the same zenith angle and thus suffer different attenuation caused by different lengths they have to travel through the atmosphere before reaching the surface detector. Fortunately, it is possible to derive a functional relationship $CIC(\theta)$ which parametrizes the effect of the attenuation as function of θ . The key idea is that without an intervening atmosphere - and thus without attenuation - the number of cosmic ray showers would be constant as function of $\cos^2(\theta)$. This follows from geometrical considerations, as the flux from a given solid angle has to be simply projected to the active area in case of a two dimensional (fully efficient) ground detector, cf. also section 2.1.

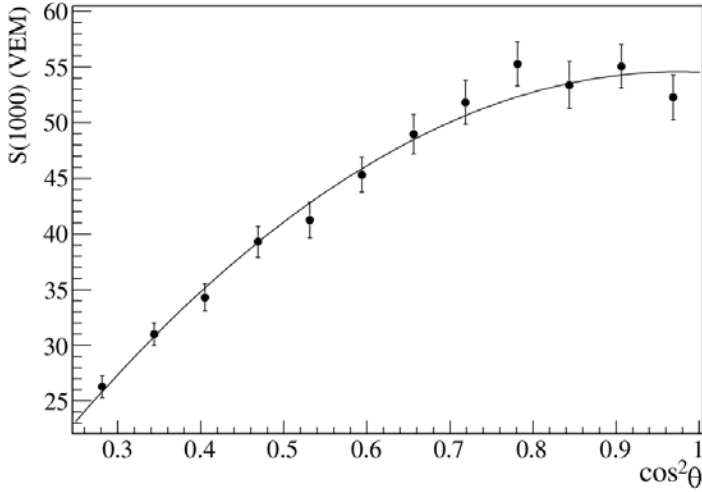


Figure 1.17.: Derived attenuation curve $CIC(\theta)$ using the surface detector data from the Pierre Auger observatory [88].

Thus, the deviation from a constant number of observed showers - or equivalently a constant intensity as measured on ground - as function of $\cos^2(\theta)$ is the needed attenuation function $CIC(\theta)$, see figure 1.17. Once $CIC(\theta)$ is known it is possible to calculate S_{38° for each cosmic ray event which would be the signal strength again in 1000 m distance but for an equivalent shower with a zenith angle of 38° . These S_{38° values are calibrated with the hybrid energies. Calibrating the surface detector with the hybrid energies in this way has the advantage to be less dependent on air shower simulations. A disadvantage is the small number of UHECR events which are simultaneously measured in both detector systems. Only 795 hybrid events were available to perform the calibration in 2009 [88].

There are some extensions planned or already installed to increase the capability of the Pierre Auger observatory for UHECR detection [90]: Recently telescopes have been built which allow for air shower observations from elevation values 30° - 59° . This will help to get a more detailed picture of the longitudinal shower profiles and extends the energy range of the Pierre Auger observatory to lower energies. This will close the gap in energy to air shower experiments like KASCADE-Grande. Additionally, an infill array of muon counters will be installed which will provide additional information on the air shower development and composition. But, also the detection of air showers using their radio signature is under study. Using this technique, it might be possible to get information on the longitudinal shower profile but with a technique that has a 100% duty cycle - like the ground array.

The next and next to next experimental steps in UHECR observation are the larger ground based arrays like the northern Auger observatory with an array of 20000 km^2 [90] and the JEM-EUSO experiment which presumably will be installed on the international space station ISS [91]. The latter aims on gathering UHECR data at energies above the expected GZK threshold.

Source Search Using a Binomial Scan Technique

The Pierre Auger collaboration has established a directional correlation of UHECR data with energies larger than $E_{\text{th}} > 56 \text{ EeV}$ and the distribution of nearby AGN from the Veron-Cetty Veron (VC-V) catalog with redshifts smaller than $z_{\text{max}} < 0.018$ [5]. The angular scale of this correlation was found to be $\psi = 3.1^\circ$. To find these correlation parameters, a scan in energy, redshift and angular separation ((E, z, ψ)) was performed which minimizes the probability that isotropy generates the observed correlation. It uses binomial statistics and considers top hats around the AGN. Due to this features, it is often referred to as *three dimensional binomial scan technique*. More details are given in chapter 2.1.

This chapter describes an extension of the binomial scan technique to take an additional AGN property (here, e.g. the radio luminosity) into account as a fourth scan parameter next to (E, ψ, z) . This might help to further classify the AGN which are the sources of at least some UHECR. Hence, this approach is associated with the points **P1** and **P2** (s. discussion in chapter *Motivation & Preface*). Additionally, a method to exclude the Galactic plane region (GPR) from the binomial scan procedure (referred to as Galactic plane cut GPC) is presented. Due to screening by Galactic matter, the GPR is a likely region for a catalog incompleteness.

A statistical test is introduced which allows to test the hypothesis of anisotropy after each newly measured event in a growing independent data set, see section 2.9.1. This class of test is called sequential probability ratio test (SPRT) and was established by A. Wald [92].

2.1. The Binomial Scan Technique

The binomial scan technique was introduced to search for anisotropies in the arrival directions of UHECR with respect to the celestial position of potential UHECR sources [93], here for example AGN. It is motivated by a set of *flux-assumptions*: due to the predicted GZK effect, UHECR at the highest energies should originate from sources within a volume $V_{\text{GZK}} \propto z_{\text{max}}^3$. In addition, a possible correlation is expected to become significantly diluted below an energy threshold E_{th} (or for large redshifts) by the deflection of the charged UHECR in magnetic fields. Hence, a three dimensional binomial scan in decreasing energy E and in increasing angular separation ψ as well as redshift z has

been performed: Using their redshift z as a rough distance measure $d \propto z$, the AGN were divided into subsets $M(z') = \{\text{AGN} | z < z'\}$ with $z < z'$ and increasing redshift z' . In the next step the isotropic, binomial probability $p(\psi', z')$ has been calculated to measure events inside top hats, that means from the area within ψ' degrees, around the AGN $M(z')$. Using the number of correlations $k(E', z', \psi')$ within top hats of radius ψ' around the AGN $M(z')$ with $N(E')$ events having energies $E > E'$, one can calculate the P -value $P[N(E'), k(E', z', \psi'), p(\psi', z')]$

$$P(N, k, p) = \sum_{j=k}^N \binom{N}{j} p^j (1-p)^{N-j} = I_p(k, N-k+1). \quad (2.1)$$

This is the binomial probability to reject isotropy wrongly given k or more correlations out of N events. Note, that the P -value can be calculated using the incomplete beta function $I_x(a, b)$. The set of *correlation or minimum parameters* $(E_{\text{th}}, \psi, z_{\text{max}})$ are those which minimize the P -value

$$P_{\min}[N(E_{\text{th}}), k(E_{\text{th}}, z_{\text{max}}, \psi), p_0(\psi, z_{\text{max}})] \stackrel{!}{=} \min. \quad (2.2)$$

The evaluation of equation 2.2 for different combinations of the discrete scan parameter values (E', ψ', z') incorporate *multiple trials*. Thus, the observed probability P_{\min} is probably too small and needs to be corrected. The probability which is freed from the effects of multiple trials is referred to as *penalized* probability P_{pen} , see chapter 2.5 in this context. A more detailed description of the binomial scan technique is given in [93].

An important part of this analysis is the calculation of the isotropic probability p to measure events from the area around a set of AGN which are encircled by top hats with an opening angle ψ . Here, this is done by simulating isotropic arrival directions according to the SD exposure of the southern PAO. The mathematical framework needed to do so can be derived easily [94]: The SD array of the Pierre Auger observatory is fully efficient for energies $E > 3$ EeV and inclination angles $\theta < 60^\circ$. In this context fully efficient means that the flux of cosmic rays through the active area of the detector is governed by purely geometrical considerations and, accordingly, decreases proportionally to $\cos(\theta)$. Furthermore, the SD array has a duty cycle of 100%. Thus, assuming that the SD array would be located at the penetration point of the Earth's rotational axis on its surface, far away astronomical objects would run in circles with fixed declination δ . Hence, the exposure would simply be a function of the declination which would coincide with the site system's zenith angle θ . The only difference is that the zenith θ is measured from the z -axis (Earth's rotational axis) down while the declination is measured starting in the $x - y$ plane. In particular, the exposure is independent of the right ascension α . Of course, the PAO is located at a latitude of -35.2° and not at the Earth's poles. Consequently, one can relate the equatorial and detector coordinates using a counter clockwise rotation of $90^\circ + 35.2^\circ$ around the x -axis

$$\begin{aligned} \vec{u} &= \begin{bmatrix} 1 & 0 & 0 \\ 0 & -\sin(35.2^\circ) & -\cos(35.2^\circ) \\ 0 & \cos(35.2^\circ) & -\sin(35.2^\circ) \end{bmatrix} \begin{pmatrix} \sin(\theta) \cos(\phi) \\ \sin(\theta) \sin(\phi) \\ \cos(\theta) \end{pmatrix} \\ &= \begin{pmatrix} \sin(\theta) \cos(\phi) \\ -\sin(35.2^\circ) \sin(\theta) \cos(\phi) - \cos(35.2^\circ) \cos(\theta) \\ \cos(35.2^\circ) \sin(\theta) \cos(\phi) - \sin(35.2^\circ) \cos(\theta) \end{pmatrix}. \end{aligned}$$

Here, $\vec{u} = \{\cos(\alpha)\cos(\delta), \sin(\alpha)\cos(\delta), \sin(\delta)\}$ is in equatorial coordinates. Identifying the z -components and solving for δ gives

$$\delta = \arcsin(\cos(-35.2^\circ) \sin(\theta) \cos(\phi) + \sin(-35.2^\circ) \cos(\theta)). \quad (2.3)$$

As stated above, the effective area of the planar array scales with $\cos(\theta)$. The corresponding solid angle $d\Omega = \sin(\theta)d\theta d\phi$ scales with $\sin(\theta)$. Thus, the measured flux of cosmic rays scales with $f(\theta) \propto \sin(\theta) \cos(\theta)$. Given a uniformly distributed random number r , a function $\theta(r)$ which is distributed according to the density $f(\theta)$ can be found via the equation [95]

$$\int_{0^\circ}^{\theta(r)} f(\theta') d\theta' = r. \quad (2.4)$$

Using $f(\theta) \propto \sin(\theta) \cos(\theta)$ and solving for $\theta(r)$ gives [93]

$$\theta(r) = \arcsin(\sqrt{r}). \quad (2.5)$$

Therefore, a set of isotropic equatorial coordinates (α, δ) can be obtained by choosing a random number r and convert it into an azimuth angle θ according to equation 2.5. Here, r was chosen out of the interval $[0; \sin^2(60^\circ)]$ to restrict the Monte Carlo to zenith angles $\theta < 60^\circ$, as explained above. Then, the declination value δ can be derived from equation 2.3 using θ and a right ascension value α chosen from a uniform distribution $[0^\circ; 360^\circ]$. The isotropic probability $p(\psi', z')$ is the fraction k/N of N simulated isotropic arrival directions (α, δ) if k of them fall into a top hat of radius ψ' around one of the AGN with $z < z'$.

2.2. Extension 1: The Galactic Plane Cut

As is well known, astronomical catalogs of extra-galactic objects tend to be incomplete for Galactic latitudes $|b| < b_{\text{cut}}$, typically with $b_{\text{cut}} \approx 10^\circ - 12^\circ$. In the past, cuts have been proposed (and applied) to discard events and AGN with $|b| < b_{\text{cut}}$. After exclusion of measured events and AGN from this region, the usual scan is performed and, in particular, a value of the angular separation ψ is found that maximizes the correlation [96], by minimizing equation 2.2.

However, there may be events at $|b| > b_{\text{cut}}$ that originate from an AGN at $|b| < b_{\text{cut}}$ missing in the AGN sample. In this case, the angular separation ψ from the scan might be biased, as the actual source of the events can not be “identified” by the scan procedure. To reduce this possible bias, a stronger cut is applied to the event list $|b| > b_{\text{cut}} + \psi$ for the event direction, where ψ is the aforementioned angular separation employed in the current scan (i.e. the event list can change during a scan depending on the current value of ψ). In this way, one avoids the situation that regions of the sky with incomplete catalog information are within an angle of ψ around the events used for the scan.

For a catalog which has no entries in the GPR region by definition, as the one discussed in chapter 4, the GPC is needed. For other catalogs, here e.g. the VC-V catalog, the link between the size of the galactic plane region and angular window ψ might cause a new bias in case of a significant excess of sources - or the presence of at least one extraordinarily strong source - near the GPR.

It is interesting to study the effect of the GPC for the example of the VC-V correlation analysis that has been published by the Pierre Auger collaboration. The same dataset up to March, 27th 2006

was chosen - as it has been done in [5] - but a more recent reconstruction algorithm (Herald v4r6p3c) with an updated energy calibration was applied (cf. [97, 98]). The results of two scans with and without exclusion of the GPR are given in table 2.1. The “shape” of the corresponding minima is shown in figure 2.1(a); that is, two parameters are fixed in the minimum while the P -value P is shown as function of the remaining scan parameter. An Aitoff projected sky map of the events and AGN which are selected by the minimum parameters is presented in figure 2.1(b). It is noteworthy that the exclusion of the GPR ($b < b_{\text{cut}} = 10^\circ$) does not significantly effect the published minimum parameters but increases the correlation fraction to 100% with $k = 10$ correlations out of $N = 10$ events. In contrast, the second scan ended with $k = 11$ correlations out of $N = 14$ events. As one would expect, the higher correlation fraction is linked with a P_{\min} which is smaller by a factor ~ 10 . Note, in comparison with [5], a drop in the energy threshold E_{th} is expected because an updated energy calibration was used here.

2.3. Extension 2: The Additional Scan Parameter

Is there an additional AGN specific property A , next to the redshift, which can be used to strengthen the correlation signal? If, indeed, one could further qualify the AGN that correlate with the UHECR data, one could support the hypothesis that AGN are not only tracers, but likely sources of - at least some - UHECR.

Candidates for intrinsic AGN properties to be considered might be astronomical observables like the *flux density* F or the luminosity L in a preselected frequency band. Also, flux density ratios might be interesting: e.g. the radio to infrared flux ratio $F_{\text{radio}}/F_{\text{infrared}}$, cf. chapter 2.11. Here, it was decided to account for the additional observable A by introducing a forth scan parameter into the binomial scan technique. Furthermore, the flux-assumption was incorporated that high values of A should be linked with a stronger contribution to the UHECR-flux.

More technically the method works as follows: Order the AGN by the 4th scan parameter A and create subsets $R(A') = \{\text{AGN} | A > A'\}$ with a decreasing threshold A' . Start a three dimensional scan for each of the AGN subsets $R(A')$ and find the overall minimum P_{\min} of the corresponding P -values

$$P_{\min}[N(E_{\text{th}}), k(E_{\text{th}}, z_{\max}, \Psi, A_{\text{th}}), p_0(\Psi, z_{\max}, A_{\text{th}})]^! = \min. \quad (2.6)$$

Note, if defined in this way, the P-Value is a function of A and, thus, provides a fourth minimum parameter A_{th} .

I.e., the four dimensional scan is just a sequence of three dimensional scans with decreasing threshold in the additional AGN observable A .

It should be stressed that the binomial scan technique in general has the disadvantage to saturate the binomial probability p for large source numbers and/or large angular separations [5]. This drawback is eased by selecting smaller source numbers due to a further qualification of source candidates in terms of A . E.g., the VC-V catalog contains only 237 radio sources “closer” than $z \leq 0.024$, the catalog of radio and infrared galaxies discussed in chapter 4 will presumably have even less entries.

2.4. Four Dimensional Scan Using VC-V Radio AGN

In this section, the radio luminosity is used as the fourth scan parameter in an analysis which includes VC-V AGN with a listed radio flux $F_{6\text{cm}}$ at 6 cm wavelength. In spite of its lack of statistical com-

Galactic plane cut (GPC)	P_{\min}	E_{th}/EeV	Ψ/\circ	$z_{\max}(<)$	N_{Evt} ($E > E_{\text{th}}$)	N_{gal} ($ b > 10^\circ$)	N ($E > E_{\text{th}}$) ($ b > 10^\circ + \Psi$)	k	N_{exp}	p_0
Yes	$7.52 \cdot 10^{-7}$	52.42	3.2	0.018	17	12	10	10	2.44	0.244
No	$6.20 \cdot 10^{-6}$	55.89	3.2	0.018	14	-	-	11	2.92	0.208

Table 2.1: Results of two three dimensional scans: with exclusion of the GPR (upper row) and without exclusion of the GPR (lower row). The columns 2-5 contain P_{\min} and the obtained minimum parameters. The number of events N_{Evt} with $E > E_{\text{th}}$ and N_{gal} with the same energy threshold but additionally outside the Galactic plane $|b| > 10^\circ$ are given in column 6 and 7. Column 9 yields the number of correlations k with the N events with $(E > E_{\text{th}})$ and $(|b| > 10^\circ + \Psi)$ as given in column 8. Column 10 gives the expected number of correlations N_{exp} for a binomial distribution with probability p_0 (column 11) for N events.

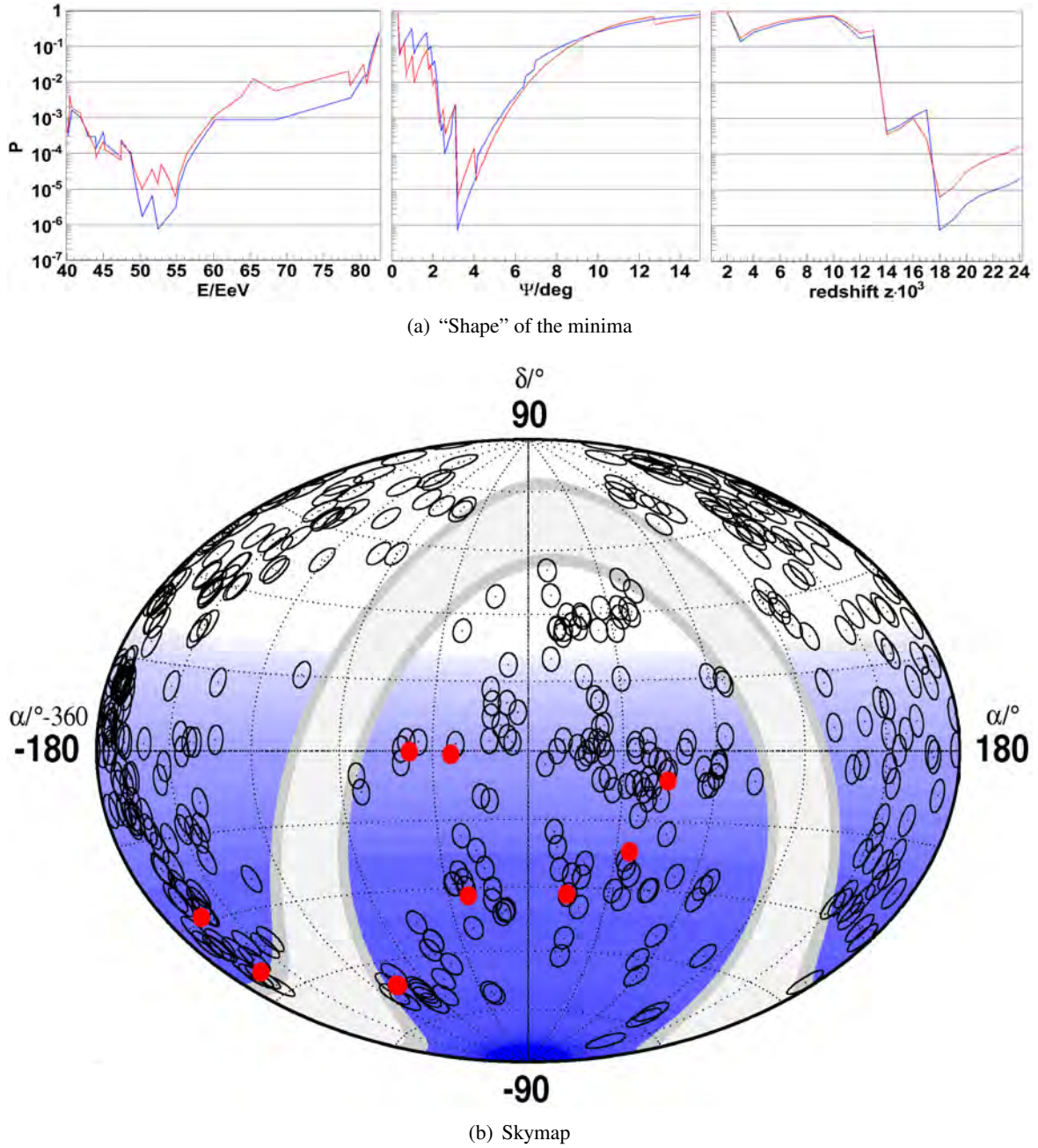


Figure 2.1.:

- (a) Development of P as function of one scan parameter if the other two ones are fixed in the observed minimum values for: a scan with Galactic plane cut $b_{cut} = 10^\circ$ (blue) and without Galactic plane cut (red).
- (b) Skymap of AGN (located in the center of the black circles with radius $\psi = 3.2^\circ$) and events (red dots) until May, 27th, 2006 within the minimum parameters. The gradient of blue represents the relative exposure of the surface detector of the PAO. The white band marks the AGN exclusion area ($|b| < 10^\circ$). The grey band indicates the extended event exclusion area ($|b| < 10^\circ + 3.2^\circ$). The x -axis shows the right ascension α for $\alpha < 180^\circ$ and $\alpha - 360^\circ$ otherwise.

plteness, the VC-V catalog has gained general interest due to its aforementioned correlation with the Auger data at highest energies [5]. In what follows, comments will be given at points in the discussion which might be limited due to the VC-V incompleteness¹.

It should be stressed, that the analysis method itself is independent of the VC-V catalog and can be applied to different sets of source candidates, too.

2.4.1. Data Set

In this section the used AGN set and the UHECR data as well as the corresponding quality criteria are introduced.

Event Set

The UHECR data set has been reconstructed using the Herald v4rp3c framework [98]. In particular, this includes an updated energy calibration if compared to [5]. Here, only events with energies $E > 40$ EeV are included in the analysis. The measurements have to meet the *standard* quality criteria, listed e.g. in [99, 100] That is, only events with zenith angles $\theta < 60^\circ$ are considered. In addition, five of the six SD stations that surround the station with the highest signal needed to be active and the reconstructed shower core has to lay within an equilateral triangle of active stations. These requirements are important as the data taking started before all SD stations were deployed in the field [99]. For example, during the time from January, 1st 2004 to June 2008, the number of installed stations grew from 154 to 1600.

An *exploratory* data set from January, 1st 2004 to March, 2nd 2008 was used to perform a four dimensional scan to fix a set of minimum parameters in chapter 2.4.2. A remaining *independent* data set up to July, 4st 2010 is used to monitor the signal later on (see chapter 2.10). The undivided data set corresponds to an exposure of $21758 \text{ km}^2 \cdot \text{sr} \cdot \text{y}$ [101]. Herein, $11191 \text{ km}^2 \cdot \text{sr} \cdot \text{y}$ is the exposure of the exploratory data set. The remaining $10567 \text{ km}^2 \cdot \text{sr} \cdot \text{y}$ correspond to the independent data set.

Note, events are usually rejected which were measured in periods of high detector instability (so called *bad periods*). A list of this bad periods can be found at [102]. As this cut was not mentioned in [99], [100] or [5] it was not included in the “exploratory” scan in chapter 2.4.2. It would have rejected one additional event with an energy of 41 EeV.

In contrast, the bad period list was applied during the monitoring with the independent data in chapter 2.9.

AGN Set

A subset of 355 AGN from the VC-V catalog closer than $z = 0.04$ and with listed radio flux densities $F_{6\text{cm}} > 0$ at 6 cm have been selected [4]. This collection of AGN will be referred to as *radio AGN*

¹Actually, it might be that a current, complete - that means a volume and flux limited - sample of extra-galactic objects might not contain a significant fraction of UHECR sources due to the limitations of today’s astronomical observations. Additionally, radio catalogs do not provide redshift information and, hence, no clue about the sources’ distance. The redshift has to be taken from different measurements which are likely to be linked with “manual” labor performed by astronomers. That’s why it might be hard to make a quantitative statement about the statistical completeness of an astronomical catalog which can be used as an input for this analysis (s. chapter 4 for details in this context).

Name [ref]	distance d/Mpc	redshift z
M 31 [103]	0.77	0.00019
NGC 3031 [103]	3.63	0.000884
NGC 3607 [104]	19.9	0.00485
Centaurus A [105]	3.4	0.00083

Table 2.2.: Using the listed distances, redshift values have been added to the VC-V catalog (applying a Hubble constant of $H_0 = 73 \text{ km/s/Mpc}$ [106]).

AGN selection (always $z > 0$ and $F_{6\text{cm}} > 0$)	BL Lac	Quasars	AGN
$z \leq 0.04$	9	10	336
$z \leq 0.024$	3	4	230
$z \leq 0.017$ and $\log_{10}(F_{6\text{cm}} \cdot z^2 / \text{Jy}) > -5.36$	1 (Cen A)	1 (3C278)	54

Table 2.3.: The AGN have been selected by their redshifts and radio flux densities (column 1) from the three tables (named: BL Lac, Quasars, AGN) that comprise the full VC-V catalog. The number of sources included from the different tables are given in the columns 2 to 4. Note, the meaning of the subset of AGN defined in row three will become clear in the context of chapter 2.4.2. In the last row the names of the AGN have been added if only one entry remains.

in what follows. But note, these AGN are not necessarily *radio loud* in terms of the astronomical classification as introduced in section 1.2. As in [5], some galaxies are include in the AGN sample which are classified as nuclear HII regions. In the past, they were considered to be AGN, but they were reclassified later [4]. In this chapter, the redshift cut $z \leq 0.024$ has been chosen as in [5]. This selects 237 VC-V radio AGN. Only in section 2.11, the volume has been enlarged allowing for AGN up to $z \leq 0.04$. The redshifts in VC-V are listed with a precision of three internal decimal places. Thus, objects with $z < 0.0005$ might end up with a redshift $z = 0$ in the catalog. Therefore, redshifts with a higher precision were added for entries with a given radio flux density but $z = 0$, see table 2.2. Additionally, a total flux density of $F_{6\text{cm}} = 597 \text{ Jy}$ has been added for Centaurus A according to [105]. See appendix A for the full list of all AGN which were considered here.

It should be outlined that the VC-V catalog consist of three separated tables called BL-Lac, Quasars and AGN. Here, galaxies from all these tables are considered - as has been done in [5], too. The contribution of galaxies from the three individual tables to the full AGN set is summarized in table 2.3.

Note, the VC-V catalog is a collection of optically detected AGN. This fact might already reduce the completeness of radio sources in this sample . The radio flux density $F_{6\text{cm}}$ in the VC-V catalog has been taken from the literature. If more than one measurement was available, one was arbitrarily chosen by Veron-Cetty and Veron. The radio flux at $F_{20\text{cm}}$ is tabulated, too. But, as it is mainly extracted from the NVSS catalog of the northern hemisphere there is a lack of sources for declination $\delta < -40^\circ$ [107] - as the PAO mainly observes the southern hemisphere this information is insufficient. The VC-V catalog is not statistically complete. It is merely a collection of AGN which are known to the literature [4].

2.4.2. Scan in Radio Luminosity

In many bottom-up scenarios, the UHECR acceleration is driven by the electro-magnetic force. Often the particles are thought to be kept and scattered in the acceleration region by magnetic fields. Hence, accompanying electrons are expected to create a radio signal via synchrotron radiation [108], see the corresponding discussions in the sections 1.2.2 and 1.1 for details. Thus, the radio emission of an astronomical object might be a natural indicator in order to identify the sites of UHECR acceleration and, accordingly, radio luminosity or flux are good choices for the fourth scan parameter. Here, luminosity $L = \Delta E_{\text{em}}/\Delta s$ is the amount of energy ΔE radiated per unit time Δs while flux $F = \Delta E_{\text{mes}}/\Delta s/\Delta A$ is the energy ΔE_{mes} measured per unit time and area ΔA on Earth. Note, that the UHECR acceleration capability of an AGN might in general be related to its luminosity (cf. equation 1.4), as the acceleration could require a minimum amount of release in energy per unit time. I.e., a nearby source, such as Centaurus A, might have a strong radio flux but may not have sufficient power to accelerate particles above 50 EeV. On the other hand, the radio- and UHECR flux might drop e.g. proportionally to the squared source distance $\propto d^2$, if emitted isotropically, which favors the flux to further qualify the sites of UHECR acceleration.

As is well known, the radio flux is highly variable - sometimes even on the timescale of days. Speculatively, if this variability would be linked with a *burst* like acceleration of UHECR, one might never observe a correlation of the radio emission of AGN and the measured UHECR due to the big time of flight difference for the synchrotron photons compared to the charged UHECR. This is because the latter ones become deflected in magnetic fields during their voyage to Earth, see equation 1.15 in this context. On the other side, a continuous pre-acceleration might be needed while a burst itself might only push the particles to the highest energies. This continuous pre-acceleration might be linked with a luminosity threshold in the radio emission of UHECR sources.

Here, the main focus is on the case of the radio luminosity L as the fourth scan parameter. In general, to correct for redshift effects, the so called *standard K-correction* needs to be applied to relate the radio flux density F as measured on Earth with the radio luminosity L of a galaxy

$$L = 4\pi D_L^2 (1+z)^{-(1-\alpha)} F. \quad (2.7)$$

Here, D_L is the *luminosity distance* of the galaxy and α is the mean slope of the power law spectra of radio galaxies. Assuming isotropic emission, $D_L \approx cz/H_0$ and that $z \ll 1$ one finds

$$L \approx K F z^2. \quad (2.8)$$

for nearby sources², where $K = 4\pi(c/H_0)^2$. As the galaxies in this chapter are nearby it is reasonable to apply the approximate expression given in equation 2.8. In what follows L and $F z^2$ - that is with $K = 1$ - are used synonymously. The logarithm of the luminosity $A = \log_{10}(F z^2/\text{Jy})$ has been chosen as the fourth scan parameter simply because the luminosity spans many orders of magnitude.

The scan in the redshift z is performed with a step size of $\Delta z = 0.001$ in the interval $(0, 0.024]$. The range of the fourth scan parameter $\log_{10}(F_{6\text{cm}} \cdot z^2/\text{Jy})$ is $[-9, -2.26]$ with a step size of $\Delta \log_{10}(L/\text{Jy}) = 6.74 \cdot 10^{-2}$. This choice ensures that the change in the number of AGN per scan step is smaller than or equals two $\Delta N_{\text{AGN}} \leq 2$ This can be seen in figure 2.2 which displays the change in the number of AGN as function of the redshift and the fourth scan parameter $\log_{10}(F_{6\text{cm}} \cdot z^2/\text{Jy})$. The angular separation ψ is restricted to $[0^\circ, 15^\circ]$ with a step size of $\psi = 0.1^\circ$. Finally, the scan in energy is performed for each event with an energy larger than 40 EeV. The scan steps and ranges are summarized in table 2.4.

²To estimate the distance $d \propto z$ via the inverse redshift z might be inaccurate for very nearby sources because of their proper motion. Hence, it is recommended to work with an improved distance measure in the future.

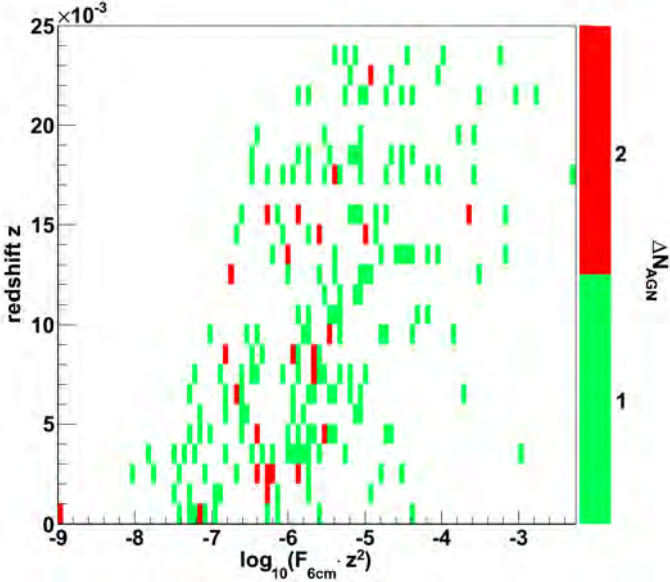


Figure 2.2.: Number of VC-V AGN ΔN_{AGN} (color coded) versus redshift z and logarithmic luminosity $\log_{10}(F_{6\text{cm}} \cdot z^2/\text{Jy})$. The width of the bins corresponds to the step sizes as chosen for the four dimensional scan.

variable	minimum value	maximum value	definition of step size
E/EeV	40	1000	each event
z	0	0.024	0.001
ψ/\circ	0	15	0.1
$\log_{10}(F_{6\text{cm}} \cdot z^2/\text{Jy})$	-9.00	-2.26	$6.74 \cdot 10^{-2}$

Table 2.4.: Scan ranges and step sizes for the four dimensional scan.

Table 2.5 holds the findings of a set of four dimensional scans. In the first row the results of a four dimensional scan are presented with the exclusion of the GPR with the GPC introduced in chapter 2.2. The observed minimum parameters are: $E_{\text{th}} = 51.92 \text{ EeV}$, $\psi = 5.9^\circ$, $z_{\text{max}} = 0.018$ and $\log_{10}(F_{6\text{cm}} \cdot z^2/\text{Jy}) = -5.36$. One can count $k = 17$ correlations out of $N_{\text{Evt}} = 31$ events which gives $P_{\min} = 1.28 \cdot 10^{-7}$. The isotropic, binomial probability is $p_0 = 0.14$. An Aitoff projected sky map of the 31 events and the 56 AGN selected by these minimum parameters is given in figure 2.3(a). This minimum is one of the key results of this chapter and will be often used in what follows.

Including the GPR region, one gets slightly different minimum parameters which mainly differ in the angular separation $\psi = 7.0^\circ$, cf. second row of table 2.5. As a matter of fact, one would expect a smaller angle due to the GPC, as introduced in 2.2, but it might well be just an effect of the reduced average angular distance between the AGN and the UHECR data rather than a reduced bias in ψ . Indeed, one finds a more significant correlation of $P_{\min} = 3.14 \cdot 10^{-8}$ if the GPR is included in the scan. In spite of that, to reduce possible biases in the minimum parameters due to a catalog incompleteness, it was decided to use the scan with exclusion of the GPR in what follows. The development of the P -value as function of one scan parameter, while the remaining three ones are fixed in the minimum, is presented in figure 2.3(b).

For the sake of completeness, some astronomical features of the correlated AGN, as reported in

Galactic plane cut (GPC)	Cen A	P_{\min}	E_{th}/EeV	Ψ/\circ	$z_{\max}(<)$	N_{Evt} ($E > E_{\text{th}}$)	N_{gal} ($E > E_{\text{th}}$) ($ b > 10^\circ$)	N ($E > E_{\text{th}}$) ($ b > 10^\circ + \Psi$)	k	N_{exp}	p_0	$\log_{10}(F_{6\text{cm}} \cdot z^2 / \text{Jy})$	$L_{\text{th}} (\text{WHz}^{-1})$
Yes	in	1.28 · 10⁻⁷	51.92	5.9	0.018	45	36	31	17	4.38	0.14	-5.36	9 · 10²¹
No	in	3.14 · 10 ⁻⁸	54.89	7.0	0.017	35	-	-	19	4.97	0.14	-5.36	9 · 10 ²¹
Yes	out	5.3 · 10 ⁻⁷	51.92	6.3	0.018	45	36	31	18	4.82	0.16	-5.36	9 · 10 ²¹
No	out	2.55 · 10 ⁻⁸	54.89	7.0	0.017	35	-	-	19	4.91	0.14	-5.36	9 · 10 ²¹

Table 2.5.: Results of the four-dimensional radio scans at 6 cm with and without exclusion of the GPR region (column 1) using data until March, 2nd 2008. For both cases a scan with and without Centaurus A in the AGN sample has been performed (column 2). Columns 3 to 6 give the minimum probability P_{\min} and the associated correlation parameters. The number of events N_{Evt} (with $E > E_{\text{th}}$), N_{gal} (with $E > E_{\text{th}}$ and $|b| > 10^\circ$) and N (with $E > E_{\text{th}}$ and $|b| > 10^\circ + \Psi$) are shown in column 7 to 9. The number of observed k and - in case of isotropy - expected number N_{exp} of correlations can be taken from column 10 and 11. $N_{\text{exp}} = N p_0$ can be calculated using the isotropic, binomial probability p_0 as given in column 12. The logarithmic radio luminosity threshold $L_{\text{th}} \propto F_{6\text{cm}} \cdot z^2$ is given in column 13. Finally, the luminosity in the proper units of WHz^{-1} is given in the last column, cf. equation 2.8.

The main results have been highlighted (boldface). These values will be extensively used and discussed in the following sections.

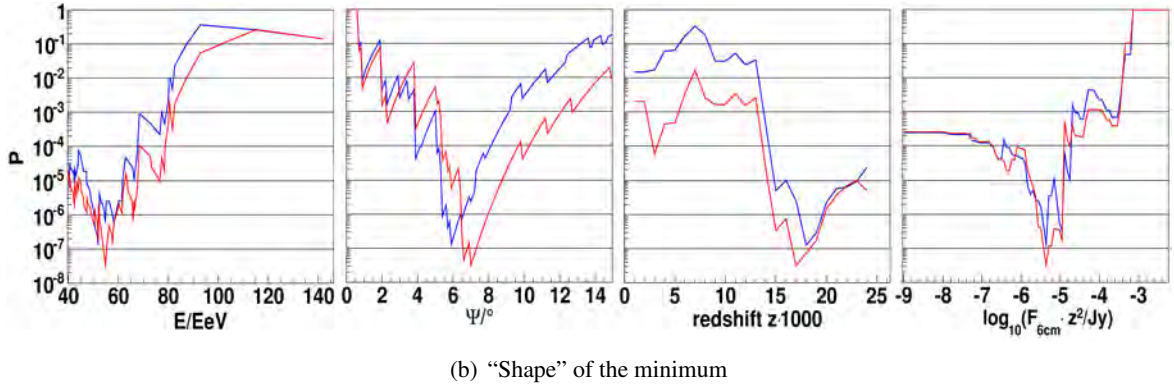
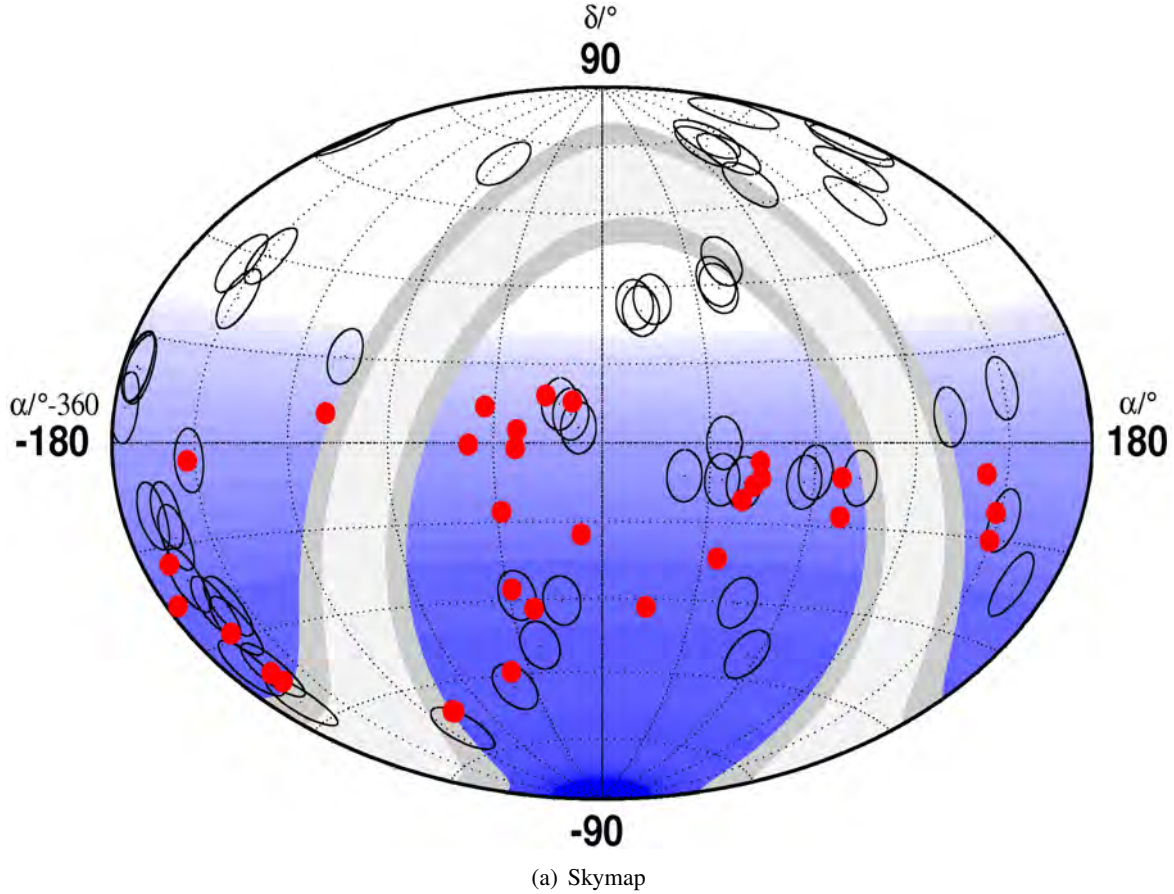


Figure 2.3.: Graphs to visualize the observed minimum if scanning in radio luminosity $L_{\text{th}} \propto F_{6\text{cm}} \cdot z^2$ at 6 cm wavelength including Cen A in the AGN sample, cf. row one and two in table 2.5:

- (a) The exposure of the Pierre Auger observatory is given in shades of blue. The white and grey bands mark the exclusion area for AGN ($|b| < 10^\circ$) and events ($|b| < 10^\circ + 5.9^\circ$) due to the Galactic plane cut which takes ψ properly into account (see section 2.2). The coordinates of the events are marked with a red dot. The positions of the AGN are tagged by a black circle with a radius of $\psi = 5.9^\circ$. The x -axis shows the right ascension α for $\alpha < 180^\circ$ and $\alpha - 360^\circ$ otherwise.
- (b) While three parameters are fixed in the minimum, P is given as a function of the remaining fourth scan parameter. One curve for a scan with/without exclusion of the GPR region is given in blue/red, respectively.

the VC-V catalog, and the number of correlations are listed in table B.1 in appendix B. This kind of table is a good starting point for future analysis work. In particular, the AGN with many correlations, starting with those located in low exposure regions, should be closer looked at.

To check if Centaurus A, the extended radio AGN closest to Earth, plays an important role in this correlations study, the previously discussed scans was repeated excluding Centaurus A from the AGN sample. As can be seen in table 2.5, this does not significantly change the observed minimum parameters. This is due to other radio VC-V AGN which are located in the vicinity of the direction of Centaurus A. The equatorial coordinates of Centaurus A are $(\alpha, \delta) = (201.367^\circ, -43.017^\circ)$.

It should be noted that all scans which are presented in table 2.5, although they slightly differ in $E_{\text{th}}, z_{\text{max}}$ and ψ , found the same threshold in the radio luminosity of $\log_{10}(L_{\text{th}}/\text{Jy}) = -5.36$. This corresponds to a luminosity of $9 \cdot 10^{21} \text{ W Hz}^{-1}$. This value is further discussed in chapter 2.11. Furthermore, it is striking that the minima observed here roughly coincides in E_{th} and z_{max} with the results of the three dimensional scan (cf. table 2.1). Thus, one might just see a signal traced by a correlation with the VC-V AGN in general or both could just be an imprint of a correlation of the UHECR data with the overall matter distribution. It might well be the other way around, too: the radio AGN could be the sources and, hence, one might see a correlation with the full set of VC-V AGN. Indeed, in the case of a tracer signal one would expect a larger angle for the AGN sets which is smaller in number [109]. This is what actually is observed, as there are 56 AGN selected by the radio threshold with $\psi = 5.9^\circ$ compared to 472 AGN with $\psi = 3.2^\circ$. The question “who traces whom” will be addressed in the sections 2.6 and 2.9.2.

In the year 2008, scans in radio flux density and luminosity were performed using the same exploratory time period but a data set which was reconstructed with an older version of the reconstruction software (Herald v4r6p1) [110]. The largest significance for anisotropy was found for the radio luminosity L with $P = 6.79 \cdot 10^{-8}$ compared to $P = 2.51 \cdot 10^{-7}$ in case of a scan in the flux density F . Accordingly, it was decided to focus on the minimum linked with the radio luminosity. When the decision was made to switch to the more recent Herald v4r6p3c this has been retained unchanged. Nevertheless, these circumstances should be kept in mind as they introduce an additional trial factor. Note, that a scan in the flux using the latest reconstruction still has a marginally larger $P_{\min} = 4.56 \cdot 10^{-7}$.

2.5. Penalized Probability

In section 2.4.2 a four dimensional scan has been presented that takes into account the radio luminosity of the VC-V AGN. The significance to reject isotropy wrongly was found to be $P_{\min} = 1.28 \cdot 10^{-7}$ with $k = 17$ correlations out of $N_{\text{Evt}} = 31$ events, see row one of table 2.5. This value is expected to be too small, as the scan procedure creates a huge number of subsets of events and AGN, according to the chosen flux assumptions, and searches for the combination of subsets that maximizes the AGN-UHECR correlation with respect to the P -value (by minimizing equation 2.2). In other words, the multiple trials which are performed amplify the number of correlations and, thus, enhances the significance in terms of P_{\min} . Therefore, the P_{\min} -values, which are the outcome of a scan, are often referred to as *unpenalized* probabilities. In general, this number can be lowered by e.g. increasing the number of trials, by choosing a smaller step size or by introducing an additional scan parameter (larger number of degrees of freedom).

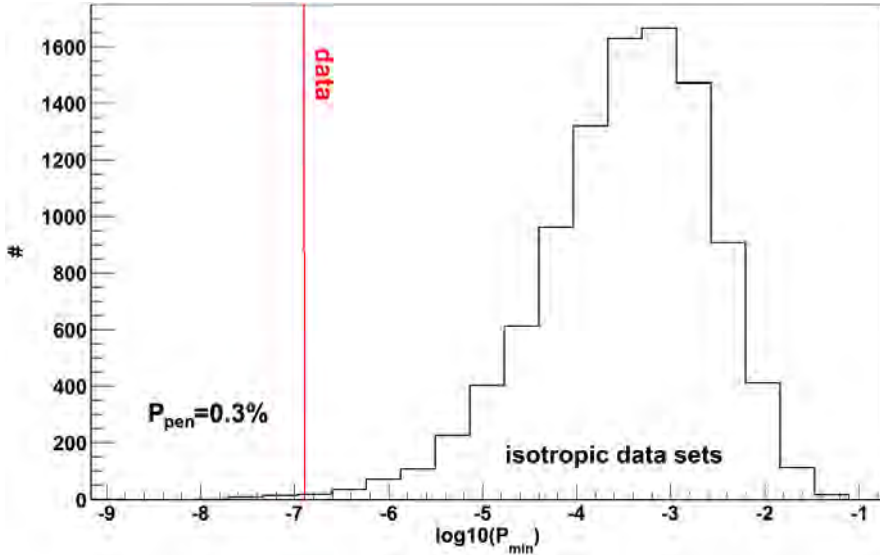


Figure 2.4.: Results from 10000 four-dimensional scans with isotropic data sets. The red line marks the P_{\min} -value as observed with the original event set.

In this subsection, the question is addressed: what was the “amplification factor” of the four dimensional scan? The P -value that takes the amplification of the scan into account is normally called the *penalized probability* P_{pen} . That is why, the penalized P_{pen} is the right choice of a measure to estimate the significance of the scans’ result.

To yield the penalized probability P_{pen} , the four-dimensional scan has been repeated 10000 times but the directions of the events have been distributed isotropically according to the Auger exposure (cf. chapter 2.1). The P_{\min} distributions can be seen in figure 2.4. Here, the vertical, red line marks $P_{\min} = 1.28 \cdot 10^{-7}$ as obtained in the original scan, see first row of table 2.5. One finds smaller P_{\min} values in 0.3% of the random experiments. As each of the P_{\min} values in this figure also suffered the amplification by the scan, this fraction is identified with the penalized probability

$$P_{\text{pen}} = 0.3\%. \quad (2.9)$$

That means: in case of isotropy the probability to find a smaller unpenalized P_{\min} value than the one observed with the measured UHECR data is 0.3%. But, this penalization procedure can not take into account multiple trials introduced by scans with other catalogs in different wavelength or alternative subsets of objects. Hence, a statistically reliable statement should preferably be made with an independent data set. A hypothesis test that can be continuously applied - that is, with each new event - on the basis of an independent data set is presented in chapter 2.9.

2.6. Improvement by the Fourth Scan Parameter?

The penalized probability as discussed in section 2.5 can mainly be used to measure the discrepancy of the UHECR arrival direction to the hypothesis of isotropy on the basis of the chosen AGN sample. But, it does not answer the question whether the introduction of the fourth scan parameter has indeed strengthen the correlation signal. I.e., is the 4d minimum just an imprint of a correlation with the overall distribution of mass or VC-V AGN?

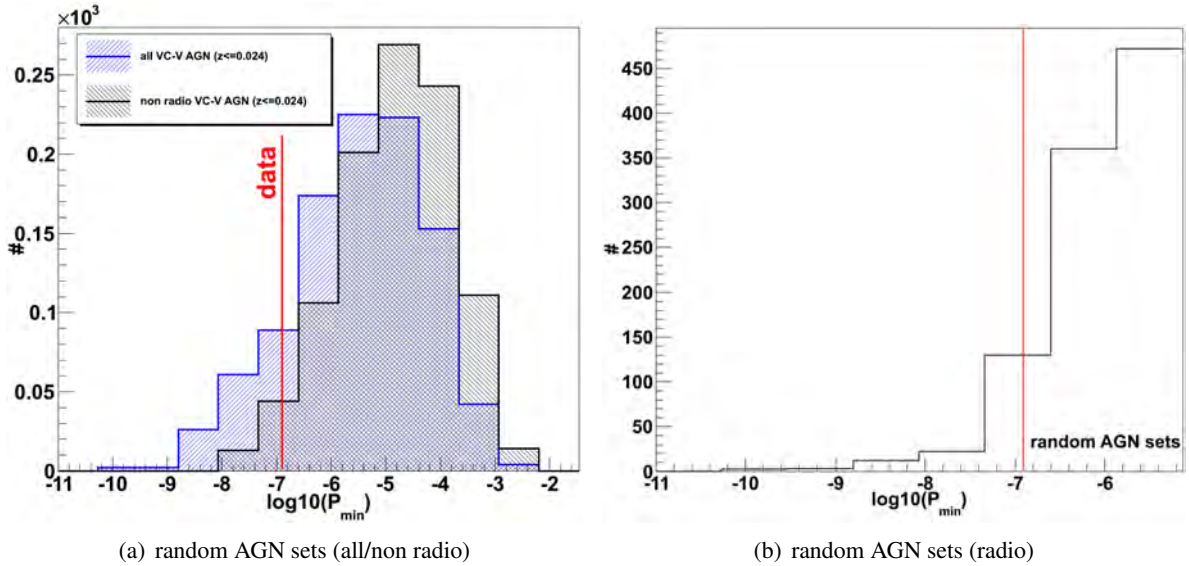


Figure 2.5.: P -value distribution for four dimensional scans with scrambled radio luminosities with
 (a) all (blue) and non radio (black) VC-V AGN,
 (b) radio VC-V AGN,
 always closer than $z = 0.024$.

VC-V AGN subsets	fraction f
non radio	3.2%
radio	10%
all	15%

Table 2.6.: Results of the luminosity shuffling experiments: description of considered subset (column one) and fraction (column two) of shuffled radio set with a smaller P_{\min} value than observed with the true AGN radio luminosity sample.

One way to address this question is to shuffle the radio luminosities among subsets of VC-V AGN N times and apply the scan on each shuffled set. Then, calculate the fraction $f = n/N$ where n is the number of sets with smaller P_{\min} values than observed with the original data. Here, three experiments of this kind were performed which differ in the subsets of VC-V AGN ($z \leq 0.024$) selected for the random shuffling

- *non radio* AGN (complement $F_{6\text{cm}} \leq 0$),
- *all* AGN,
- *radio* AGN ($F_{6\text{cm}} > 0$).

The outcomes of these random experiments for $N = 1000$ are summarized in table 2.6. The corresponding P -value distributions are given in figure 2.5(a) and 2.5(b).

Most importantly, one can see that in case of the luminosity shuffling for the complement (non radio) AGN one only obtains a more significant correlation in 3.2% of the cases. One can consider this an indication that the original configuration of the radio luminosities among the VC-V AGN seems

to fit the UHECR data better. Accordingly, the fourth scan parameter might increase the correlation strength. Note, this approach might be weakened by the catalogs' incompleteness; That is, the degree of statistical incompleteness might differ for the radio and non radio VC-V AGN subsets and that is what slightly favors the subset of radio AGN. Thus, one can only make a conclusion about the VC-V AGN but can not be sure whether it can be transferred to the true population of AGN as manifested in nature.

As stated above, the shuffling was additionally done for two subsets of AGN which include the radio VC-V AGN as well. The corresponding results are given in table 2.6, too. By doing so the fraction f seems to be increased. Thus, the 237 radio AGN in general, without a specific radio threshold, might already tend to increase the significance of the correlation.

2.7. Effect of Reconstruction Uncertainties

Of course, the measured arrival directions and the energies of the used UHECR measurements have uncertainties. Is the minimum stable within these uncertainties? That is, could a different set of minimum parameters be observed if the arrival directions and the energies were allowed to fluctuate within their uncertainties? In particular, this is an important cross check in a situation of low statistics where a possible signal is expected to be fragile to small variations in the reconstructed parameters - the situation one faces in this chapter and in UHECR physics in general.

The Herald reconstruction provides azimuth- ϕ , zenith angles θ and the corresponding uncertainties $\Delta\phi$, $\Delta\theta$. In the same way, it gives the S_{1000} and ΔS_{1000} - the estimated signal strength in a distance of 1000 m to the shower core. Assuming Gaussian fluctuations around the measured values with a standard deviation chosen to be the size of the corresponding uncertainty, one can create scrambled triples $(\phi', \theta', S'_{1000})$. Ignoring uncertainties in the reconstructed core positions and statistical correlations³ between ϕ and θ , one can calculate a scrambled arrival direction in right ascension $\alpha(\phi', \theta')$ and declination $\delta(\phi', \theta')$ in equatorial coordinates. Using θ' , S'_{1000} one can calculate a scrambled energy $E'(\theta', S'_{1000})$ using the usual SD energy calibration function found with the hybrid technique [100]. It should be emphasized that this scrambling only considers statistical reconstruction uncertainties. But, it might also be useful to e.g. scramble the constants of the SD energy calibration function within their uncertainties for each set of scrambled events in the future. 1000 sets of scrambled data sets were created. The used cuts in energy and zenith (cf. section 2.4.1) were released for the scrambling

- $E > 30$ EeV,
- $\theta < 65^\circ$

to allow events to fluctuate inside the boundaries of the original cuts. The differences in the arrival direction and the energy between the original data set and one scrambled realization are exemplary shown in figure 2.6(a) and 2.6(b). In this special case, the 68%-quantile in the arrival direction is 0.2° - 0.3° and the average relative change in energy is 4%.

The variations of the four minimum parameters, as caused by the statistical uncertainties of the UHECR reconstruction, are displayed in figure 2.7. The changes in the P_{\min} and p_0 values as well as the correlation fraction can be seen in figure 2.8. In all graphs, a red line marks the position of the corresponding value which was obtained with the original data set. The main result is that the minimum parameters are narrowly distributed around the ones found using the original data set. Hence,

³Indeed, they are not included in the standard data set.

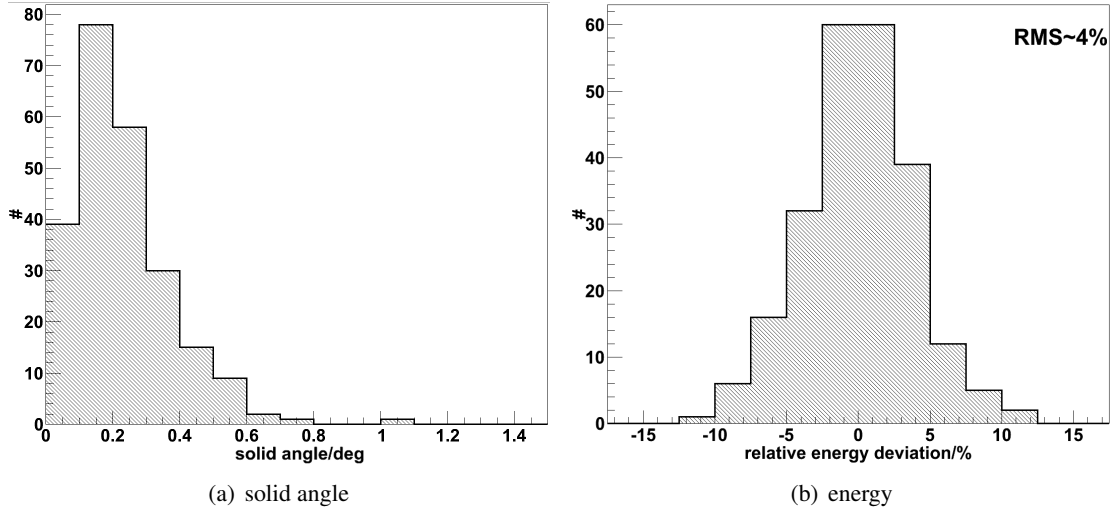


Figure 2.6.: Graphs to illustrate the scrambling of energies and arrival directions of the UHECR data within the statistical reconstruction uncertainties assuming Gaussian smearing around the measured values. Difference in the smeared and true arrival directions (a) and energies (b) for one of the scrambled data sets.

the minimum seems to be reasonably stable given the statistical uncertainties of the reconstruction. A closer look shows an additional peak in the distribution in the ψ , L_{th} and p_0 distributions. It should be noted that, in case of ψ , the two peaks might not be distinguishable with the instrumental resolution of $\sim 1^\circ$ of the Pierre Auger observatory. It is interesting to mention that these additional peaks in ψ , L_{th} and p_0 are not correlated.

2.8. Hide and Seek

To prepare a *faked* data set with a hidden signal and to try to recover it later on, is a common approach to study the reliability of an analysis chain or its response e.g. as function of the event statistic, the signal's strength or the dependence on one or more parameters of a physical model under consideration. As a matter of fact, the motivation of the four dimensional binomial scan is mainly based on qualitative flux assumptions, which are discussed in section 2.1 and 2.3. No quantitative model expectation was made like the angular distance $\psi(E, z, Z, \dots)$ or the GZK-like flux suppression $S_{\text{GZK}}(E, z, Z, \dots)$ as function of energy energy E , redshift z , charge Z , etc. As the modeling of UHECR acceleration and propagation is highly complex, one could consider this rather large model independence as the advantage of the applied binomial scanning technique. Hence, it was decided to refrain distance from model testing with extremely simplified models at this point. As model testing will be crucial for the understanding of the mechanisms of UHECR acceleration and propagation - which is much more than checking for anisotropy or identifying the sources - chapter 3 deals with a modeling tool of UHECR propagation named CRPropa. Hopefully, CRPropa will be one important component in a future simulation chain which includes predictions about UHECR acceleration, propagation and the effects of air shower development and detection. A first analysis of this kind is discussed in chapter 3.9.2. Clearly, if one would feed into the four dimensional binomial scan a proper model prediction, this should clearly result in minimum parameters which are in agreement with the ones that were found using the

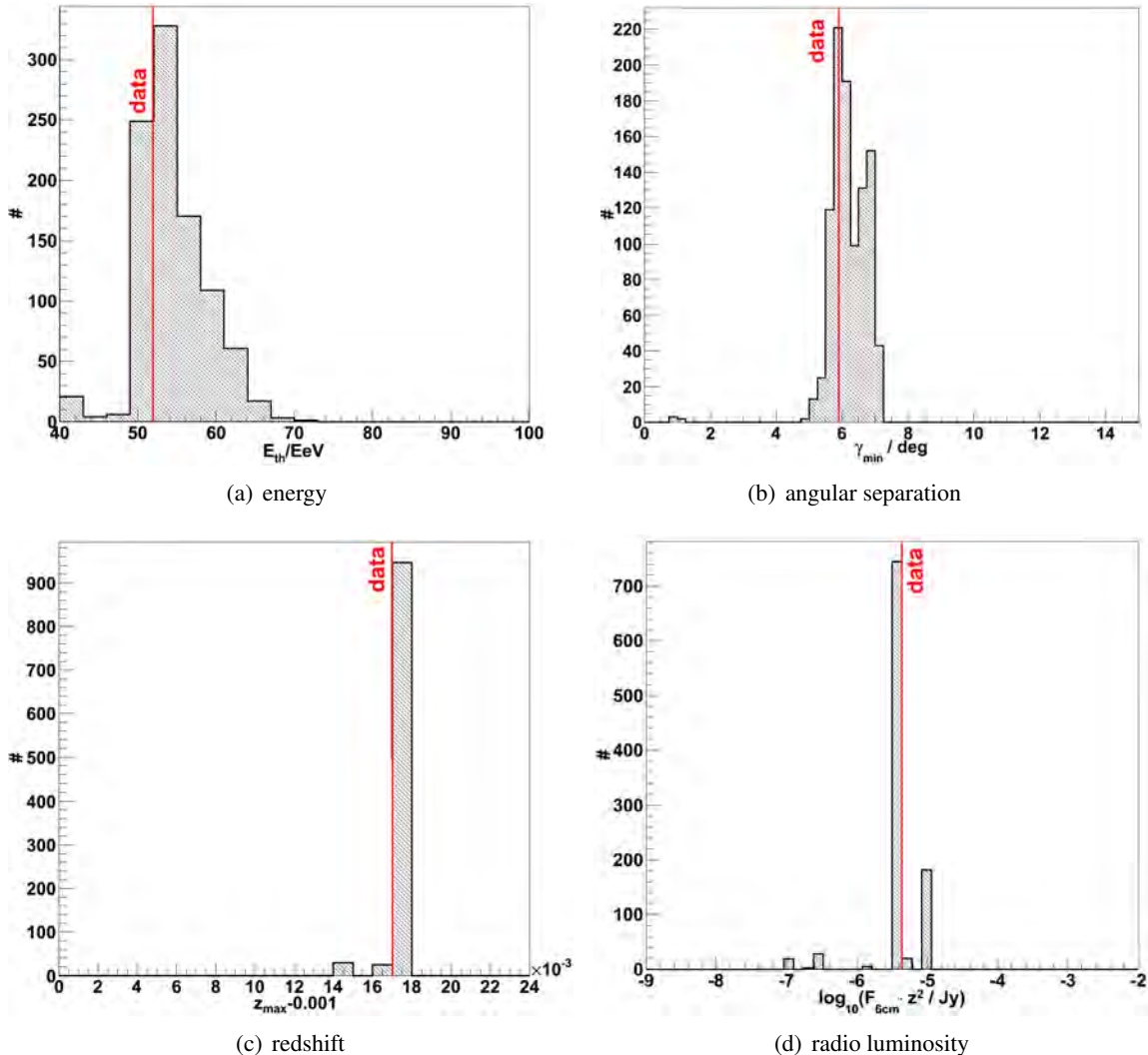


Figure 2.7.: Distributions of the minimum parameters which are observed with the scrambled data sets: energy (a), angular separation (b), redshift (c) and radio luminosity (d). The values which were obtained with the original data have been marked with a red line.

measured data. Hence, it would be interesting to study the outcome of the four dimensional scan if a full CRPropa simulation is used as input.

Here, a signal is hidden in fake data sets according to the aforementioned flux assumptions as follows⁴: Choose a correlation strength p_1 . Divide the events with $E > E_{\text{th}} = 51.92 \text{ EeV}$ and $|b| > 10^\circ$ into a set of correlated \mathcal{M}_{cor} and uncorrelated $\mathcal{M}_{! \text{cor}}$ events using a sequence of uniformly distributed random numbers [0,1] and assuming a correlation strength of p_1 . Then, isotropically distribute the arrival directions of the events out of $\mathcal{M}_{! \text{cor}}$ and of those ones with $E < E_{\text{th}}$ and $|b| > 10^\circ$. Randomly select one AGN outside the galactic plane ($|b| > 10^\circ$) within the range of the scan parameters $z < 0.018$ and $\log_{10}(F_{6\text{cm}} \cdot z^2) > -5.36$ for each event which is an element of \mathcal{M}_{cor} . Finally, choose a correlated

⁴One might already consider the set of flux assumptions a simple model. But, it clearly is only a qualitative and not a quantitative one.

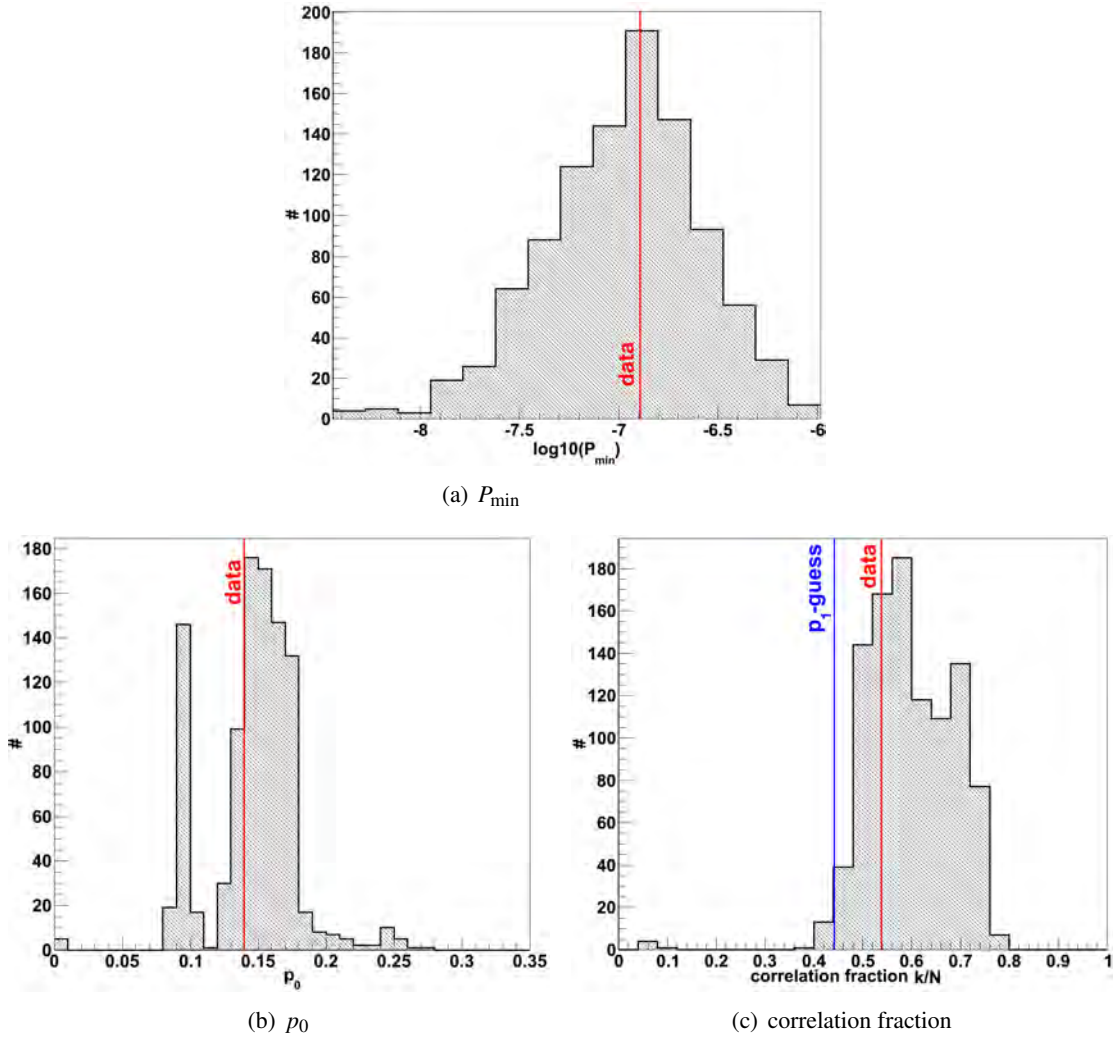


Figure 2.8.: Effect of the statistical reconstruction uncertainties in the UHECR arrival directions and energies on P_{\min} (a), isotropic probability p_0 (b) and the correlations fraction (c). The red line marks the position of the values which were observed with the original data. The blue line indicates the value of a guess of the correlation strength which will be needed and discussed in chapter 2.9 to fix the error of 2nd kind β in order to create a test of hypothesis.

arrival direction within $\psi = 5.9^\circ$ and $|b| > 10^\circ$ around these AGN for the corresponding events. I.e. if one assumes that the parameters which were found in the scan using the real data are the true ones, then the events were, indeed, distributed with a correlation strength p_1 , in agreement with the flux assumptions. Would one measure the same minimum parameters, again?

The arrival directions of 1000 sets of events with a hidden signal of strength $p_1 = 50\%$ are displayed in figure 2.9(a). The distribution of the unpenalized probability P_{\min} and the recovered minimum parameters are shown in figure 2.9(b) - 2.9(f). As the observed correlation fraction of $17/31=55\%$ is unpenalized and presumably too large, these distributions are given somewhat smaller values of $p_1 = 40\%$ and $p_1 = 50\%$. The distribution of the minimum parameters always peak around the values which were used to hide the signal. But as expected, one can see a more significant rejection of

isotropy and a more narrow distribution of the minimum parameters in the stronger signal's case of $p_1 = 50\%$.

Due to the oversimplified assumptions which were used to generate the faked data sets, the main conclusion of this section is that the analysis chain seems to work reliably. This has been carefully checked with additional cross checks which will not be discussed here, too.

Nevertheless, the large width of the distributions in figure 2.9(b) - 2.9(f), especially if combined with the widths of the figures 2.7(a)-2.7(d), might indicate that more UHECR statistic is needed for the scan to converge. Thus, the statistical uncertainties of the minimum parameters might still be too large to prepare a reasonable prescription.

2.9. Prescription Principles and Suggestions

In chapter 2.4.2, a set of a priori minimum parameters were discussed which minimized the probability of rejecting UHECR isotropy wrongly using radio VC-V AGN in a four dimensional scan procedure. Based on this correlation, chapter 2.9.1 deals with the creation of a hypothesis test which can be applied using an independent data set. Here, we focus on a sequential probability ratio test (SPRT) as suggested by A. Wald [92]. The sequential approach allows to check the status of the hypothesis test with each new event. To apply SPRTs in the context of UHECR astronomy has been suggested in [111].

To check if the introduction of the radio luminosity as the fourth scan parameter (cf. chapter 2.3) has improved the significance of the correlation, the luminosity shuffling experiments of the type as presented in chapter 2.6 are repeated but with an independent data set. For details have a look at chapter 2.9.2.

The full data set can be used for the scan to test if the minimum parameters remain unchanged. This is presented in chapter 2.9.3.

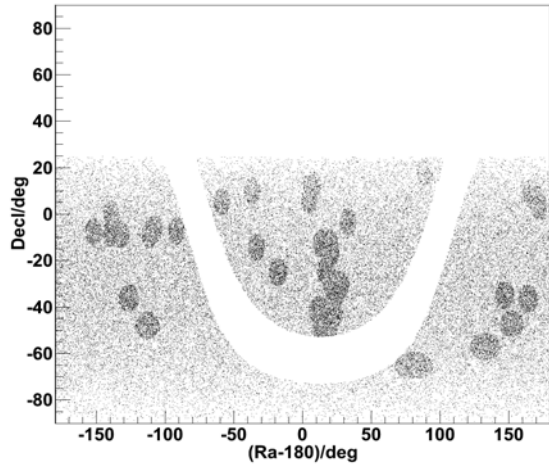
The analysis work presented in chapter 2.9.1 to 2.9.3 has been done in 2009. This is why the focus is on an independent data set only until March 31st, 2009. A short update which is limited to the main results but using the data up to July 4th, 2010 is subject to chapter 2.10.

It should be pointed out that the Pierre Auger collaboration supports the monitoring of a possible correlation with radio VC-V AGN but no *official* prescription has been initiated. The efforts and ideas which are described in this chapter have been mentioned in [80] but without calling numbers.

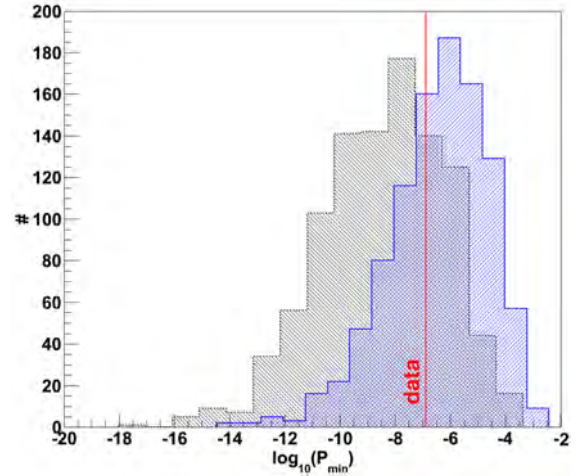
2.9.1. Wald's Sequential Probability Ratio Test

In chapter 2.4.2 a set of minimum parameters ($E_{\text{th}} = 51.92 \text{ EeV}$, $\psi = 5.9^\circ$, $z_{\max} = 0.018$, $\log_{10}(F_{6\text{cm}} \cdot z^2/\text{Jy}) = -5.36$) were found that minimized the probability P to wrongly reject the isotropy of the UHECR arrival directions (see table 2.5 upper row). More precisely, this set of parameters minimizes equation 2.6. In this way a set of 56 VC-V AGN is selected with radio luminosities⁵ at a wavelength of 6 cm with redshifts $z < 0.018$. The binomial probability to measure an event from a top hat with radius ψ around these AGN is $p_0 = 0.14$. The penalized probability for the correlation to arise out of an isotropic distribution was found to be $P_{\text{pen}} = 0.3\%$, see chapter 2.5. As emphasized, the penalization

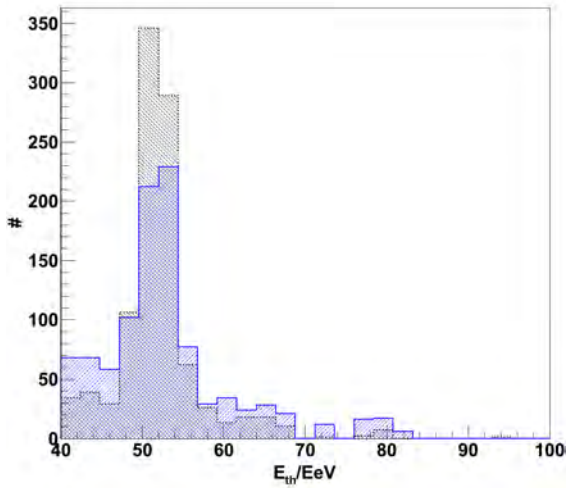
⁵The reader should keep in mind that Fz^2 is proportional to the luminosity L according to equation 2.8 $\log_{10}(F_{6\text{cm}} \cdot z^2/\text{Jy}) > -5.36$. Thus, the radio luminosity threshold can be written as $L > 9 \cdot 10^{21} \text{ W Hz}^{-1}$.



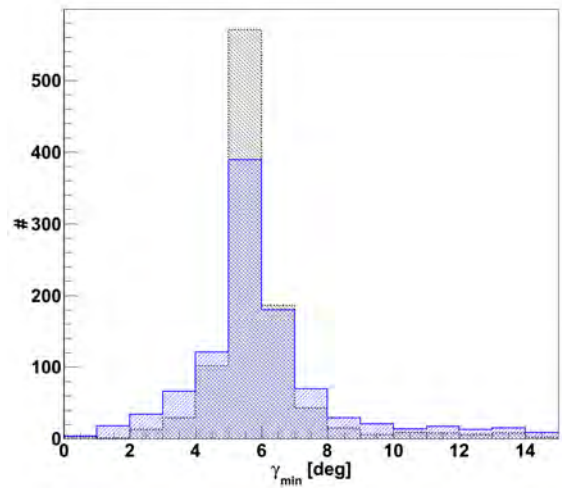
(a) sky map



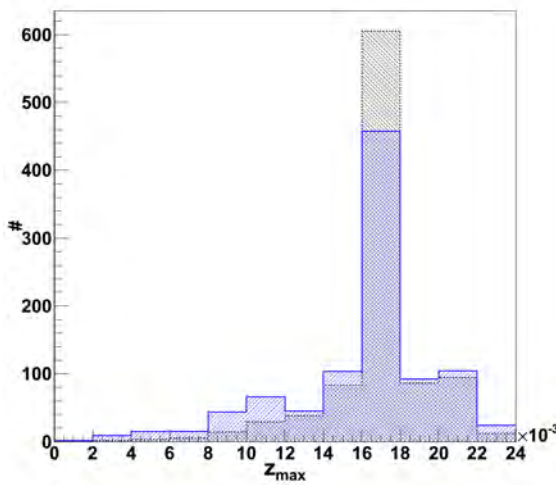
(b) P_{\min} distribution



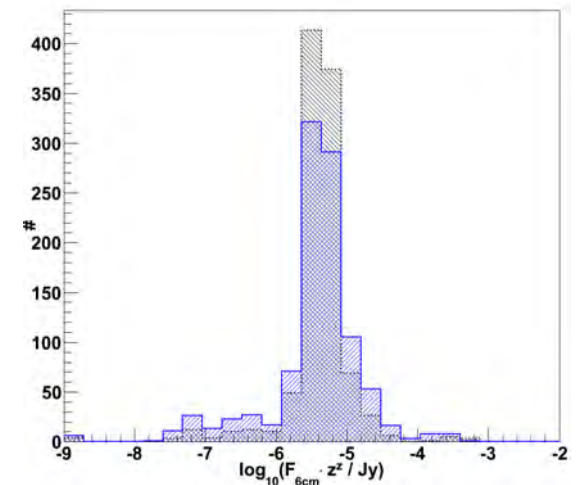
(c) energy



(d) angular window



(e) redshift



(f) radio luminosity

Figure 2.9.: The arrival directions of 1000 sets of events with a hidden signal of strength $p_1 = 50\%$. (a). P_{\min} distribution of scans using the 1000 data sets with a hidden signal (b). Corresponding minimum parameters for: energy, angular separation, redshift and threshold in the radio luminosity (c)-(f). In blue distributions for $p_1 = 40\%$, in black for $p_1 = 50\%$. The red line marks the position of $P_{\min} = 1.28 \cdot 10^{-7}$ as has been found for the real data set, see first row of table 2.5.

can only take into account a bias of the scan procedure itself. It can not include the effects of multiple trials linked with similar studies which were performed elsewhere e.g. with different sets of sources using the same data. Hence, a good way to get an unbiased chance probability is to fix the determined minimum parameters and perform a hypothesis test using an independent data set.

A hypothesis test is generally constructed to decide which of two alternative hypotheses H_0, H_1 is more likely to be present in nature. Here, H_0, H_1 are the hypotheses of isotropy, anisotropy of the UHECR arrival directions with respect to the position of the selected 56 VC-V radio AGN. Naturally, such a decision is linked with two falsities α and β often referred to as error of 1st and 2nd kind. More detailed, α is the probability to reject H_0 (isotropy) although it is true while β is the probability of accepting H_0 (isotropy), although it is wrong.

One class of hypothesis tests, called sequential probability ratio tests, have the advantage that they can be reevaluated with each newly measured UHECR arrival direction [92]. Its key ingredient is the calculation of likelihood ratio R_N after each new event

$$R_N = \frac{P(D|H_1)}{P(D|H_0)} = \frac{p_1^k(1-p_1)^{N-k}}{p_0^k(1-p_0)^{N-k}}. \quad (2.10)$$

As can be seen, the likelihood ratio is just the ratio of the probabilities $P(D|H_i)$ that the data set D more likely originates from a measurement which is determined by H_i . In equation 2.10, $P(D|H_i)$ was already identified with a binomial probability as it will be needed later on. As already stated above, the likelihood ratio will be calculated after each new event. Consequently, it is likely to decrease/increase if the data set favors/disfavors the predictions of H_0 compared to H_1 . For this reason an upper and a lower bound A, B are needed to implement a *stopping rule* for the SPRT

$$\text{stopping rule} = \begin{cases} R_N > A & : \text{accept hypothesis } H_1, \\ B \geq R_N \leq A & : \text{undecided} \rightarrow \text{continue taking data,} \\ B < R_N & : \text{accept hypothesis } H_0. \end{cases} \quad (2.11)$$

A. Wald showed that the bounds $A = A(\alpha, \beta)$ and $B = B(\alpha, \beta)$, that substantiate the stopping rule in equation 2.11, are very nearly independent of $P(D|H_i)$ and, hence, can be derived by only choosing appropriate values for α and β [92]

$$A = \frac{1-\beta}{\alpha} \quad \text{and} \quad B = \frac{\beta}{1-\alpha}. \quad (2.12)$$

This simplicity of calculating adequate *Wald bounds* A, B is an important reason for the popularity of SPRTs. Furthermore, due to the definition of a stopping rule that goes along with the sequential approach, this class of tests is believed to be very economically with respect to the amount of data needed for the test to end.

The isotropic probability $p_0 = 0.14$, linked with top hats around the selected 56 radio AGN, has been calculated during the scan procedure, see chapter 2.1 and table 2.5 for details. The only value needed in order to construct a SPRT is the signal strength p_1 - the binomial probability to measure an event in case of anisotropy (H_1). As one does not explicitly establish a model of UHECR acceleration and propagation p_1 can not be calculated. Thus, an educated guess had to be made. Indeed, it is valid to test against one's personal degree of belief as long as the *power* of the corresponding hypothesis

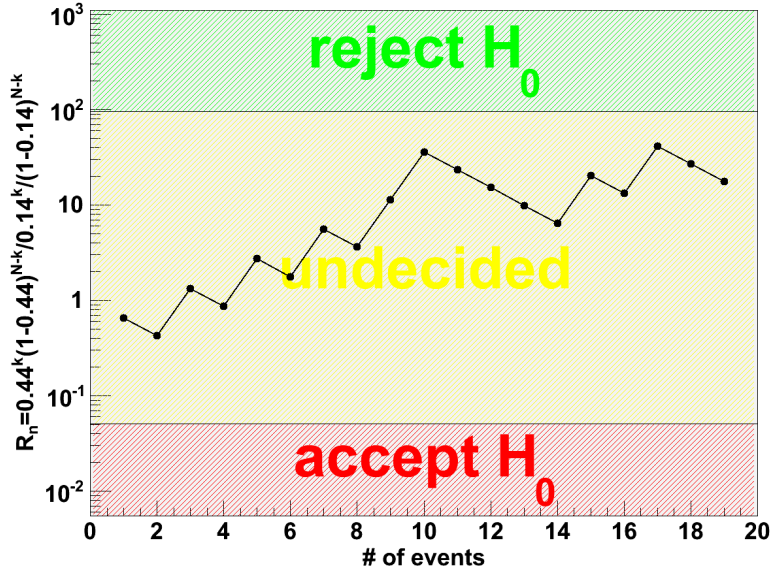


Figure 2.10.: Likelihood ratio R_N as function of the number of events N (independent data until March 31st, 2009). Wald’s bounds A, B (horizontal black lines) are used to divide the y-axis in three parts: acceptance region for hypothesis H_0 (red) and the corresponding rejection region (green). The interval of the likelihood ratio in which the SPRT remains undecided is marked in yellow.

test is specified, see the discussion later on. Note, β as function of p_1 is usually referred to as the power of a statistical test.

The scan found its minimum $P_{\min} = 1.28 \cdot 10^{-7}$ with $k = 17$ correlations out of $N = 31$ events - again these numbers are given in the first row of table 2.5. This corresponds to a correlation fraction of $17/31 \approx 55\%$. As already stated in section 2.5, the true correlation fraction is expected to be lower due to the multiple trials during the four dimensional scan procedure. By varying the minimum parameters within one scan step it is already possible to lower the correlation fraction below 40% - a similar approach has been chosen to estimate the signal strength by the Pierre Auger collaboration [5], additional details are given in [112]. Besides that, the results from the “hide and seek” approach as introduced in chapter 2.8 hints a signal strength⁶ of $p_1 \sim (40 - 50)\%$. Also, as has been shown in chapter 2.7, the uncertainties on the reconstructed parameters of the UHECR data allows for the correlations fraction to drop, too (cf. figure 2.8(c)). Based on this limited knowledge, it was decided to test against $p_1=44\%$. Again, this value can not be derived from underlying principles in absence of a quantitative model of UHECR propagation and acceleration.

Now, one can adjust the general scheme of the SPRT (equation (2.10)-(2.12)) to the case of the four dimensional scan results. Choosing the statistical falsities to be

$$\alpha = 1\% \quad \text{and} \quad \beta = 5\%, \quad (2.13)$$

one can calculate Wald’s bounds via equation 2.12

$$A = 95 \quad \text{and} \quad B = 0.051. \quad (2.14)$$

⁶The difference between correlation/signal strength and correlation fraction should be emphasized. The latter one is just one choice out of a binomial probability distribution $B(p_1, N, k)$ linked with the correlation strength p_1 and $N = 31$ events.

The likelihood ratio, given in equation 2.10, can be calculated by choosing

$$p_0 = 0.14 \quad \text{and} \quad p_1 = 0.44 \quad (2.15)$$

and k being the number of correlations within $\psi = 5.9^\circ$ of the prescribed 56 VC-V AGN with the independent, growing data set ($E > 51.92$ EeV) consisting of N events.

Using the independent data set up to March 31st, 2009 with $k = 7$ correlations out $N = 19$ events, the likelihood ratio is $R_{19} = 17.6$. Note, that for the independent data set one event was excluded which was measured during a period of high detector instability, see chapter 2.4.1. As the likelihood ratio R_N remains in between Wald's bound $0.051 = B < R_{19} = 17.6 < A = 95$, the test is undecided and one has to continue taking data. The likelihood ratio R_N as function of the events N is given in figure 2.10. The y-axis - which displays the value of the likelihood ratio R_N - has been divided into three parts according to Wald's bounds, see equation 2.14. The three divisions have been color coded with respect to the action that has to follow a measured value of the likelihood ratio as prescribed in the stopping rule of the SPRT in equation 2.11. I.e. as long as the likelihood ratio remains in the yellow region no decision has been made and additional data is needed.

The effect of different choices for p_1 on the SPRT is exemplarily illustrated in figure C.1 in appendix C.

It should be noted that the independent data set which was used for this SPRT is simultaneously used for similar studies like the monitoring of the correlation with the overall VC-V AGN [97]. This again should be considered a multiple trial. To really yield a statistically significant chance probability, one has to restrict the monitoring to one potential signal, only.

In general it is important to study what could be summarized as the *characteristics* of the hypothesis test, e.g. the expected number of events needed for the test to end or its statistical power. Here, this has been done by simulating sequences of data for different assumptions of the signal strength p_1 and by studying the response of the SPRT afterward. The results are displayed in figure 2.11.

In graph 2.11(a) the statistical falsities α and β as function of the simulated correlation strength are displayed. From these simulations one can learn that $\alpha = 0.7\%$ and $\beta = 4.4\%$ at $p_1 = 44\%$. The small difference to the chosen values $\alpha = 1\%$ and $\beta = 5\%$ arise from the fact that the Wald bounds A, B are only very nearly independent of p_0 and p_1 . This difference is a small price willingly payed if one considers how simple it was to set up the SPRT in return.

Figure 2.11(b) displays the mean number of events needed for the SPRT to end as function of the simulated signal strength. Furthermore, the 90% quantiles are given. From that one can learn that in 90% of the cases the test would end with 26 events in case of isotropy with $p_0 = 14\%$. Instead, for a correlation strength of $p_0 = 44\%$ one would need 32 events.

At last the correlation fraction at which the SPRT ends as function of the signal strength is shown in figure 2.11(c) in a two dimensional representation. Here, the frequency of appearance of a correlation fraction, given a fixed signal strength, is color coded. The red crosses mark the mean correlation fraction for a fixed signal strength. One can see that the average values do not lay on a straight line. This is expected as e.g. outliers with a high correlation fraction will hit the upper border faster and create the visible bending. Thus, the observed correlation fraction after which the SPRT test ends is a biased estimator for the true correlation fraction and, hence, for the signal strength. Furthermore, there are discontinuities visible in figure 2.11(c) which are simply caused by the fact that the correlation fraction is calculated from integer numbers. Qualitatively speaking, the number of those discontinuities and their distance are expected to depend on the values of p_0 and p_1 . For example, if one would create a test with two very nearby hypotheses $p_0 \approx p_1$ a lot of very narrow discontinuities should show up.

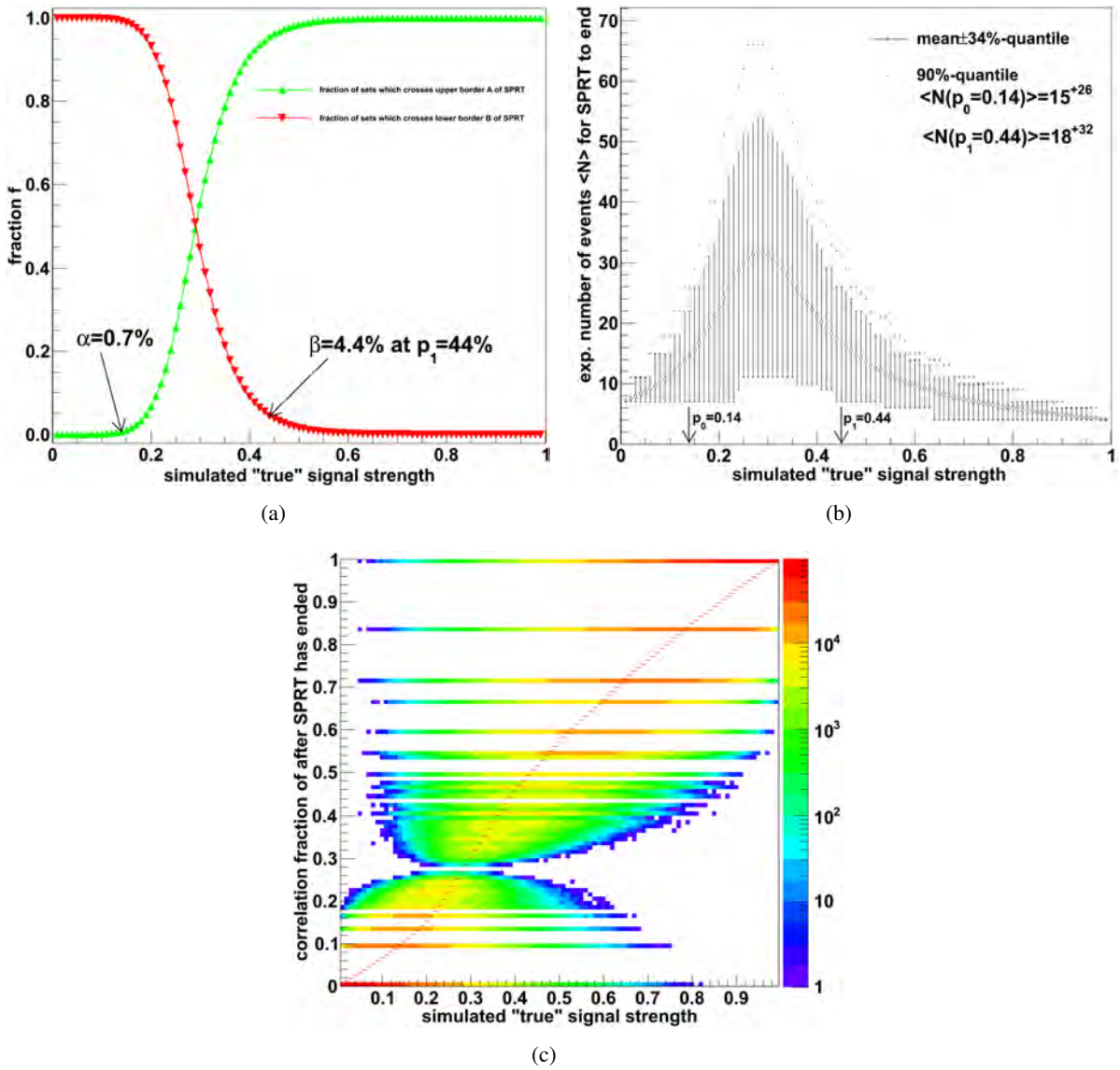


Figure 2.11.: Some characteristics of the SPRT ratio test:

- (a) Fraction out of 10^5 simulated data sets that hit the lower of Wald's bound B of the SPRT (green line) or the upper one A (red line). Thus, the red line refers to the error of 2nd kind as function of the signal strength - the so called power of the hypothesis test.
- (b) Needed number of events for the SPRT to end as function of the signal strength. The crosses are the mean values while the size of the error bars represent the 34%-quantiles with respect to the mean value - in analogy to the Gaussian σ definition. Ten percent of the simulated sets needed more events to come to a conclusion than marked with the red point.
- (c) The color coded frequency of SPRTs' outcomes as function of the signal strength and the correlation fraction k/N is shown. The red crosses mark the mean values for a fixed signal strength.

For two alternative hypotheses which can be more easily distinguished with the SPRT, e.g. $p_1 \gg p_0$, one would expect broader and less discontinuities.

2.9.2. The Luminosity Shuffling

Clearly, it would already be interesting to observe a correlation with the subclass of radio VC-V AGN using e.g. a SPRT and an independent data set as discussed in the previous chapter. But, it might well be that a possible correlation is just traced by a correlation with all VC-V AGN or the matter distribution in the nearby Universe itself. As already stated in chapter 2.6, one can try to study whether accounting for the radio luminosity of the radio AGN as fourth scan parameter really increases the significance of the correlation signal. Therefore, sets of VC-V AGN with randomly shuffled radio luminosities were created in chapter 2.6. Then it was studied whether these random AGN sets showed less significant correlations if they were used as an input for the four dimensional scan.

Here, a similar approach is chosen, but only the independent UHECR data set is used. This has the advantage that one can create subsets of AGN using the minimum parameters from table 2.5. Indeed, this was not allowed if one stuck to the exploratory data, as the minimum parameters were found in an optimization procedure - the four dimensional scan - using this very data.

The procedure will now be exemplary described for the case when the radio luminosities above the radio threshold ($\log_{10}(F_{6\text{cm}} \cdot z^2 / \text{Jy}) > -5.36$) are randomly exchanged with those ones from VC-V radio AGN below the threshold ($\log_{10}(F_{6\text{cm}} \cdot z^2 / \text{Jy}) \leq -5.36$). Only AGN which are closer than $z < 0.018$ are taken into account here. Now one can count the number of correlations k within $\psi = 5.9^\circ$ with these subsets for the $N = 19$ events above the energy threshold and outside the GPR $|b| > 15.9$, see figure 2.12(a). Surely, the number of correlations k itself is not a good measure in order to compare the correlation strength of *random luminosity AGN sets* with the true AGN set. This is, because the binomial probability value p_0 might change for an alternative set of 56 AGN. In other words, the AGN in the random sets might be located at different exposure regions and, hence, have a different isotropic expectation value $E[k] = Np_0$. This can be seen in figure 2.12(b). For this reason, the P -value $P'(k, N, p)$ has been calculated for all random AGN sets. P' can be compared with the $P(k = 7, N = 19, p_0 = 0.14) = 1.13\%$ as observed with the original radio AGN sample. The fraction of random AGN sets with $P' < 1.13\%$ is 0.59%. The color coded frequency as function of the number of correlations k and the P -value P is displayed in figure 2.12(c). Multiple peaks can be seen. They originate from the fact that the random sets are not independent and, hence, individual AGN are expected to be a part of more than one set. The procedure will then randomly distributes the correlated AGN among the set. Here, one finds between 0 and 8 correlations with the 19 events which are linked with one peak in the P -value distribution.

This procedure has been applied to different subset of VC-V AGN to perform the luminosity shuffling with and without taking into account the radio luminosity threshold value. The results are summarized in table 2.7. Again, the original AGN set shows a stronger correlation than the random sets. Furthermore, it is interesting to note that as soon as the radio luminosity threshold is included into the shuffling, the fraction of radio AGN sets which show a stronger correlation seems to drop (cf. row 1., 3. to row 2., 4. in table 2.7). Both facts indicate that the radio luminosity and the corresponding threshold might increase the correlation strength with the independent event set. As already outlined in section 2.6, care has to be taken if one intends to interpret these results due to the statistical incompleteness of the VC-V catalog.

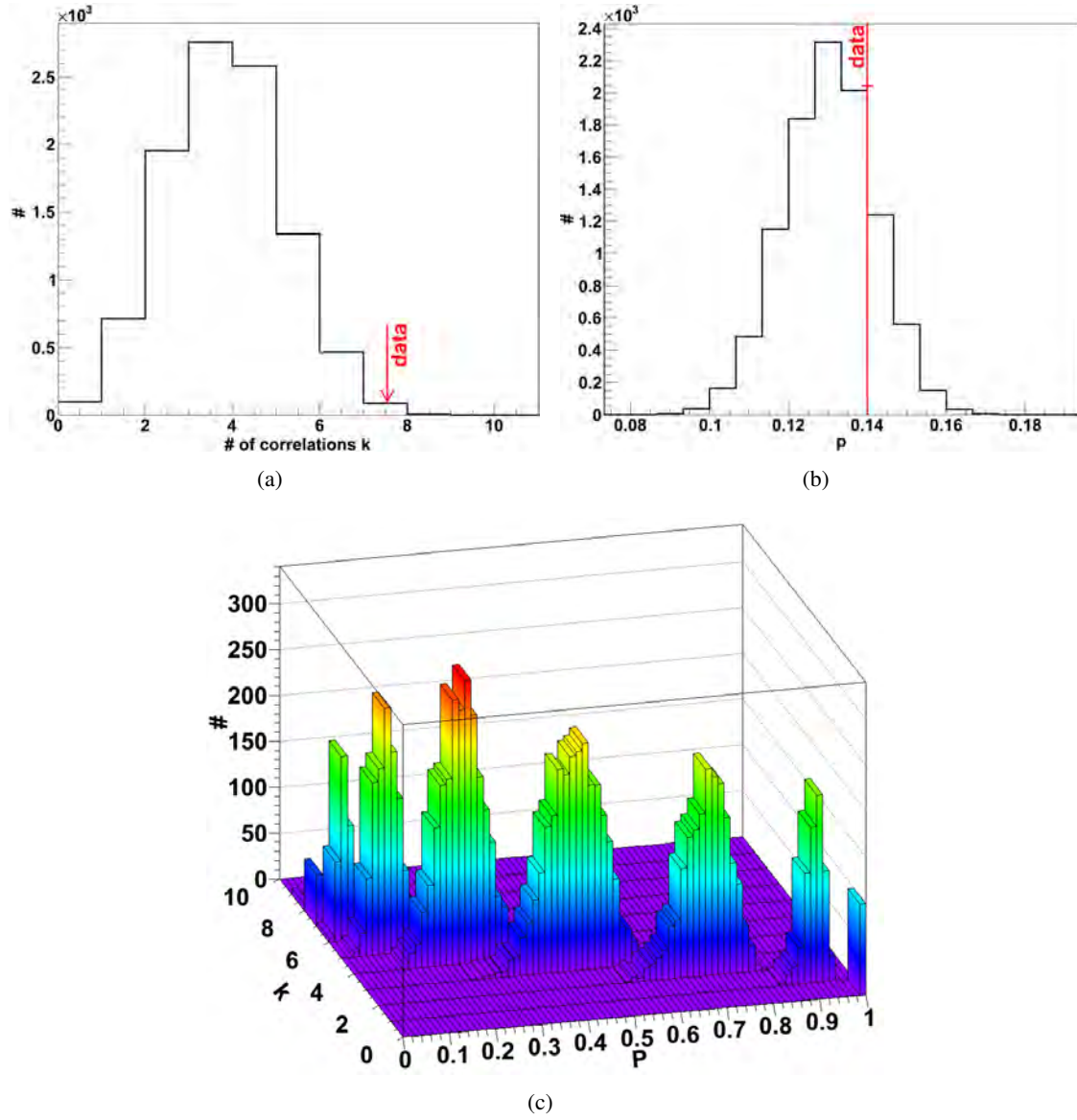


Figure 2.12.: Graphs to demonstrate the procedure for the luminosity shuffling using the independent data set up to July, 4th 2010. The graphs are exemplary for the case where the radio luminosity of radio AGN above the threshold is randomly replaced with those ones from the radio VC-V AGN below the threshold:

- (a) number of correlations k with the random AGN set,
- (b) distribution of the isotropic, binomial probability p_0 ,
- (c) frequency (color coded) of random AGN sets in the analysis as function of their number of correlated events k and the corresponding P -value.

data type	fraction $f / \%$
VC-V radio AGN (below radio lum. threshold)	0.64
VC-V radio AGN (all)	2.95
VC-V AGN (below radio lum. threshold)	0.59
VC-V AGN (all)	16.01

Table 2.7.: Results of the luminosity shuffling experiments with independent data. The first column describes the used AGN set while the second column gives the fraction out of 10000 AGN sets with a higher correlation strength than with the original AGN set.

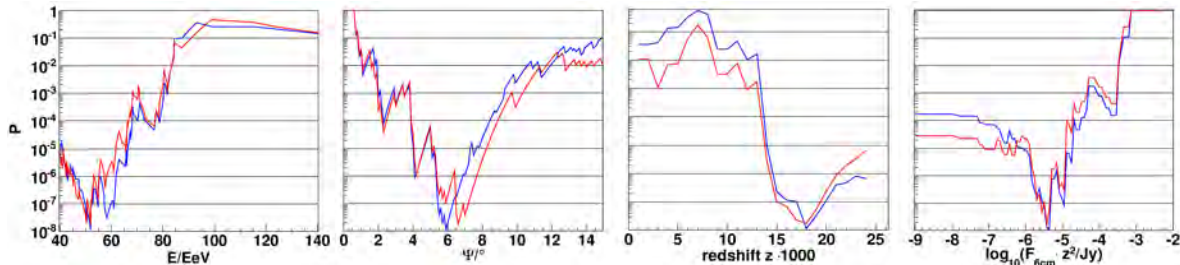


Figure 2.13.: The unpenalized probability P as function of one scan parameter while the other three scan parameters are kept fixed in the global minimum. The data set up to March, 31st 2009 was used. The blue curves corresponds to a scan with exclusion of the galactic plane region. The red lines represent the results of scan which takes the galactic plane region into account.

2.9.3. Rescanning Using an Enlarged Data Set

An important question is if the four dimensional scan finds the same minimum parameters if applied to the enlarged data set up to March 31st, 2009. This is why two scans were performed: one with and one without the rejection of the galactic plane region. The observed minima are given in table 2.8. The listed values can be compared with the results which were presented in table 2.5. The minimum found in a scan with exclusion of the GPR has slightly changed in all four minimum parameters. But, these changes are small and thus do not need to be discussed in detail. Aside from that, the main focus here is on the scan which excludes the GPR. In this case, the inclusion of the additional data does not change the minimum parameters. This agreement of the new data with the old minimum parameters is linked with a decreased $P_{\min} = 1.12 \cdot 10^{-8}$. The behavior of P as function of one scan parameter, while the other three ones are fixed in the minimum, is shown in figure 2.13. The conclusion at this point is that the minimum is stable in the light of the complete data set.

A scan which is restricted to the independent data set is not performed at this point due to the small event number.

Using 10000 sets of events with isotropic arrival directions, one only finds 5 sets with a more significant correlation than obtained with the real data. That corresponds to a fraction of $f = 5 \cdot 10^{-4}$. Using poison statistics, one can derive an upper limit $P 1.2 \cdot 10^{-3}$ (99% confidence) on the “penalized”

Galactic plane cut (GPC)	P_{\min}	E_{th}/EeV	ψ/\circ	z_{\max}	N_{Evt} ($E > E_{\text{th}}$)	N_{gal} ($E > E_{\text{th}}$, ($ b > 10^\circ$))	N ($E > E_{\text{th}}$, ($ b > 10^\circ + \psi$))	k	N_{\exp}	p_0	$\log_{10}(F_{6\text{cm}} \cdot z^2/\text{Jy})$	$L_{\text{th}}/(\text{WHz}^{-1})$
Yes	$1.12 \cdot 10^{-8}$	51.9	5.9	0.018	71	58	50	24	7.07	0.14	-5.36	$9 \cdot 10^{21}$
No	$1.72 \cdot 10^{-8}$	51.9	6.6	0.018	71	58	-	30	10.4	0.15	-5.43	$8 \cdot 10^{21}$

Table 2.8: Results of the four dimensional scan using data up to March, 31st 2009. The columns are (from left to right) GPC cut in/out, minimum probability P_{\min} , minimum parameters (energy, angular separation, redshift), number of events (above energy threshold $E > E_{\text{th}}$, above threshold and outside Galactic plane $|b| > 10^\circ$ as well as outside galactic plane plus the angular window $|b| > 10^\circ + \psi$), number of correlations k , expected number of correlations, isotropic binomial probability, logarithm of the flux threshold and the corresponding flux threshold in unit of Watts.

VC-V AGN subsets	fraction f
non radio	0.4%
radio	1.8%
all	9.4%

Table 2.9.: Results of the 1000 four dimensional scans using AGN sets with scrambled radio luminosities. The approach is explained in section 2.6. Here, a larger data set up to March 31st, 2009 was used. The columns provide a description of the considered subset for the luminosity shuffling (column 1) and the corresponding fraction (column 2) of AGN set with a more significant P -value than observed with the true AGN radio luminosity sample.

probability (cf. chapter 2.5).⁷ This indicates that using the enlarged data set increases the significance of the correlation, too.

In chapter 2.6, random sets of AGN with scrambled radio luminosity values were created and used as input for the scan procedure. The scrambling seemed to induce a weakening of the correlation signal. This was interpreted as a hint that the sorting of the AGN with respect to their true radio luminosity increases the correlation strength, see table 2.6. Here, this analysis was applied to the larger data set, too. The corresponding results are summarized in table 2.9. In summary: all numbers have decreased using the enlarged data set. Hence, the suspicion is strengthened that sorting the AGN by their radio luminosity increases the correlation signal. But it should be noted again that the conclusions based on scrambled AGN properties might be limited by the VC-V's statistical incompleteness.

2.10. Status of the Prescription Using the Latest Data Set

Using the correlation parameters of the radio AGN correlation study as presented in chapter 2.4.2, a sequential probability ratio test to test the hypothesis of isotropy was discussed in section 2.9.1. As the sequential method allows to check the status of the correlation with each new event, it is updated using the latest available dataset up to July, 4th 2010, see figure 2.14. Thus, there is more than one year of additional data available if compared to section 2.9 where the SPRT was introduced and firstly applied. Here, The current Likelihood ratio for $k = 12$ correlation out of $N = 39$ events is

$$R_{39} = 8.66. \quad (2.16)$$

Accordingly, the likelihood ratio is within Wald's bound $B = 0.051 < 8.66 < A = 95$ and more data is needed for the test to end.

It is noteworthy that in 90% of repetitions, the SPRT should end after 26, 32 events in case of isotropy ($p_0 = 0.14$), anisotropy ($p_1 = 0.44$) respectively, cf figure 2.11(b). Hence, it is interesting to note that the SPRT has not ended with the available $N = 39$ events. As the number of needed events is larger for $p_1 \in I = (0.14, 0.44)$, this might be an indication that the true signal strength is in this interval I . In this case the guess for the true signal strength $p_1 = 0.44$ would have been overestimated. Unfortunately, values $p_1 \in I = (0.14, 0.44)$ are linked with large errors of the 2nd as can be seen in figure 2.11(a). In other words, the probability to reject anisotropy wrongly would be large.

⁷Creating a larger numbers of isotropic data sets is difficult due to a limitation in CPU time.

data	P_{\min}	E_{th}/EeV	$\Psi/^\circ$	$z_{\max}(<)$	N_{Evt} ($E > E_{\text{th}}$)	N_{gal} ($E > E_{\text{th}} \wedge b > 10^\circ$)	N ($E > E_{\text{th}} \wedge (b > 10^\circ + \Psi)$)	k	N_{exp}	p_0	$\log_{10}(F_{6\text{cm}} \cdot z^2 / \text{Jy})$	$L_{\text{th}}/(\text{W Hz}^{-1})$
All	$1.55 \cdot 10^{-8}$	40.42	6.2	0.018	190	154	138	48	21.2	0.15	-5.36	$9 \cdot 10^{21}$
2nd half	$1.90 \cdot 10^{-5}$	40.4	7.0	0.018	109	90	83	19	6.52	0.08	-4.62	$5 \cdot 10^{22}$

Table 2.10: Results of two four dimensional scans: using all data up to July, 4th 2010 (upper row) and a scan restricted to the independent data after March, 2nd 2008 (lower row). The columns 2–5 contain P_{\min} and the obtained minimum parameters. The number of events N_{Evt} with $E > E_{\text{th}}$ and N_{gal} with the same energy threshold but additionally outside the Galactic plane $|b| > 10^\circ$ are given in column 6 and 7. Column 9 yields the number of correlations k with the N events with $(E > E_{\text{th}})$ and $(|b| > 10^\circ + \Psi)$ as given in column 8. Column 10 gives the expected number of correlations N_{exp} for a binomial distribution with probability p_0 . The logarithmic threshold value in radio $L_{\text{th}} \propto F_{6\text{cm}} \cdot z^2$ is given in column 13. Finally, the luminosity in units of W Hz^{-1} is given in the last column.

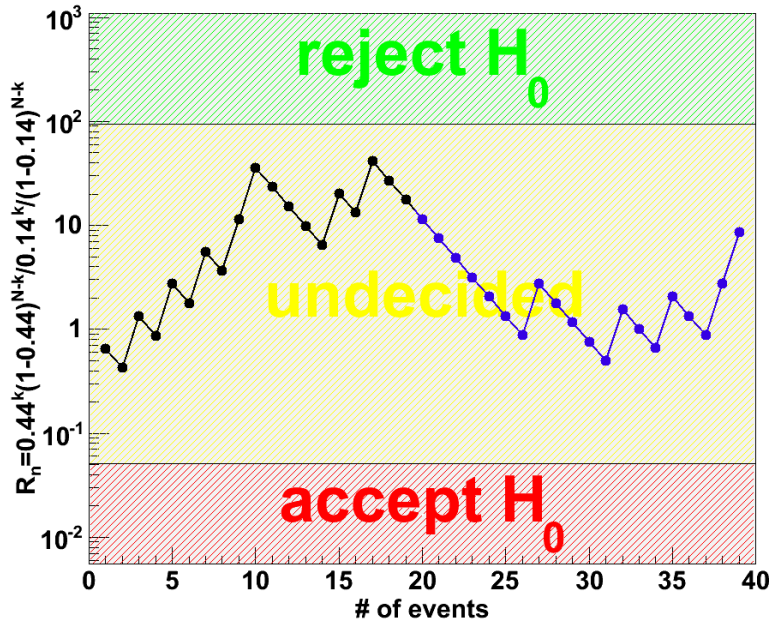


Figure 2.14.: Sequential probability ratio test as described in chapter 2.9.1. The likelihood ratio R_N is given as function of the number of events for the independent data set up to July, 4th 2010 (blue and black). The independent data set until March, 31st 2009 (black) was already displayed in figure 2.10 which is updated here. The y-axis is divided into three regions: rejection (green), acceptance (red) of the hypothesis of isotropy (H_0). The yellow band marks the region where no decision has been made and one has to continue taking data.

Furthermore, the scan has been redone using the full data set and only the independent data set. The results are summarized in table 2.10.

In case of the full data set one finds the same minimum parameters for the redshift and the radio threshold. The angular window is only larger by 0.3° . A value which is smaller than the angular resolution of the Pierre Auger observatory. Hence, this change should not be considered problematic. A more drastic variation might be the drop of the threshold energy from 51.92 EeV to 40.4 EeV. Due to the lower energy threshold, there are $N = 138$ events with $k = 48$ correlations which give a P -value $P_{\min} = 1.55 \cdot 10^{-8}$. Indeed, the prescribed minimum parameters with $k = 12$ and $N = 39$ have a similar $P_{\min} = 2.3 \cdot 10^{-8}$. The fact that two minimum parameters ($\psi, \log_{10}(F_{6\text{cm}} \cdot z^2/\text{Jy})$) do not significantly change allows one to study the P -value as function of the remaining two scan parameters (E, ψ), see figure 2.15. Note, if more than one scan step fall into one bin of this two dimensional histogram, only the smallest of the corresponding P -values is filled. A region of small P -values is visible for angular separations $\psi \in (5^\circ, 7^\circ)$ and energies $E \in (40 \text{ EeV}, 60 \text{ EeV})$. Maybe this behavior continues for lower energies $E < 40 \text{ EeV}$, but this energy range is not included in the scan. The minimum seems to be stretched parallel to the x -Axis and, in particular, there is no dependence between the change in ψ as function of E .

A scan which is restricted to the independent data results in a different minimum if compared with the exploratory phase. Indeed, only the redshift parameter remains unchanged. Again one observes a drop in the energy threshold to 40.4 EeV while the angular window increases to $\psi = 7.0^\circ$. At last, the radio threshold jumps to $\log_{10}(F_{6\text{cm}} \cdot z^2/\text{Jy}) = -4.62$. With $k = 19$ correlations with the $N = 83$ events and $P_{\min} = 1.9 \cdot 10^{-5}$ the correlation is weaker than with the exploratory data set. This

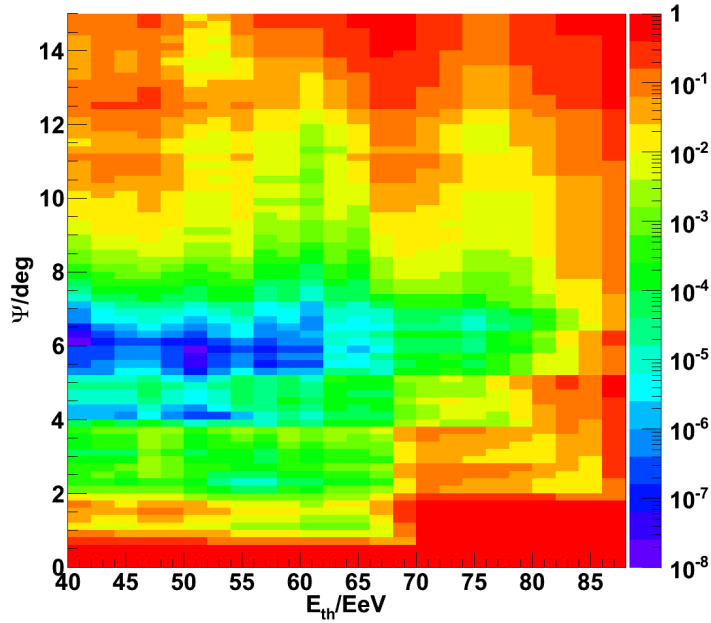


Figure 2.15.: The probability P of the scan as function of the UHECR energy threshold E_{th} and the radius of the angular window ψ . The remaining two parameters have been fixed in the minimum parameters, cf. first row of table 2.10. Here, the complete (exploratory and independent) data set up to July, 4th 2010 has been used.

fluctuation might be explained by the fact that the scan using half of the data set is not converged as discussed in chapter 2.8. It should be noted that the signal with the minimum parameters from the exploratory data has a P -value of only $P = 0.006$ using the 2nd half of the data.

The scrambling of the radio luminosities among the radio AGN, as described in chapter 2.9.2, has been repeated with the independent data set, too. The results are given in table 2.11 which can be compared with table 2.7. All values have decreased. That means, the radio AGN above the threshold seems to have a stronger correlation than the class of radio VC-V AGN or VC-V AGN in general (both closer than $z < 0.018$) within an angular window of $\psi = 5.9^\circ$.

Note, this should not be confused with the shuffling experiments as introduced in chapter 2.6 where the exploratory data set is used and a four dimensional scan is performed for each new random luminosity AGN set. As this would require time demanding calculations it is not reasonable redo this kind of analysis after each new event. It is presumably enough to redo it when the SPRT will have ended. The same is true for the calculation of the penalized probability P_{pen} .

2.11. The Radio Threshold and Additional Astronomical Properties

The radio luminosity threshold that maximized the correlation of VC-V radio AGN and the UHECR data reported in chapter 2.4.2 was found to be $9 \cdot 10^{21}$ W at a wavelength of 6 cm, compare first row of table 2.11. Assuming a power law index with a slope of -0.5, one can estimated the corresponding threshold of 2×10^{22} W at 1.4 GHz. Is this threshold value physically reasonable and in agreement with available theoretical expectations? As already discussed in context with equation 1.4, simplified models of UHECR acceleration allow for basically all radio loud galaxies to be sources of UHECR if

data type	fraction $f/\%$
VC-V radio AGN (below threshold)	0
VC-V radio AGN (all)	1.54
VC-V AGN (below threshold)	0.07
VC-V AGN (all)	0.62

Table 2.11.: Results of the luminosity shuffling experiments with independent data until July, 4th 2010. The 1. column describes the used AGN set while column 2. gives the fraction out of 10000 AGN sets with a higher correlation strength than with the true AGN set. More details can be found in chapter 2.9.2 where the method was introduced.

the latter ones are heavy nuclei. As a matter of fact, most known radio loud galaxies with a reasonable huge lobe and jet morphology in this context seem to have a luminosity larger than 10^{23}W , one can check e.g. the FRI/FRII galaxy sample in [113]. But, radio structures up to $\sim 250\text{ kpc}$ have been used to e.g. to calculate a lower radio luminosity limit in 1.1 - this is also the case for many alternative models in general. Indeed, checking the VC-V classification of the AGN above the luminosity threshold of the four dimensional scan reveals that most of them are astronomically classified as *radio quiet* - mostly of Seyfert type. Hence, from models of the type which led to equation 1.4, the measured radio luminosity threshold seems unexpectedly low. Of course, an appealing hand wave argument to keep things consistent would be a time variability of the UHECR emission and evolution of the sources. That is, due to magnetic deflections, *burst like* emitted UHECR might reach Earth much later than the corresponding radio signal, cf. equation 1.15. This might dilute a correlation signal.

But, what about Seyfert galaxies with a radio signature as UHECR sources? Clearly, they are morphologically different from radio loud galaxies of e.g. FR I/II type. Nevertheless, there have been indications for jet activity on sub-pc/pc-scales and a jet driven radio signal in some low luminosity AGN, see [42] for additional information on this or the argumentation of this passage. Note, care should be taken at this point: AGN of Seyfert type are often hosted in spiral galaxies and are maybe linked with enhanced *starburst* activity. This activity might induce a radio signal which originate in supernova driven super winds and might get confused with a jet driven radio signature. It has been suggested that starburst activity is correlated with the emission of infrared light and, hence, that the infrared to radio flux density ratio R_{FIR} could be used to separate it from jet activity.

Figure 2.16 holds the $R_{\text{FIR}}^{20\text{cm}}$ distribution for those 56 VC-V AGN which were selected by the four dimensional scan⁸ and with known flux densities $F_{60\mu\text{m}}$ and $F_{20\text{cm}}$. It should be mentioned that the infrared flux densities at 60 microns $F_{60\mu\text{m}}$ are not listed in the VC-V catalog. They have been collected using the NED database [115] and are listed in the appendix A.1. Note, that the radio flux densities at a wavelength of 1.4 GHz are used here. In this way the sample can be compared with a set of starburst galaxies from [114]. Clearly, some of the VC-V AGN populate the region of the starburst sample.

In general, the question arises if R_{FIR} is a possible alternative to the radio luminosity as the fourth

⁸ $z < 0.018$ and $\log_{10}(S_{6cm} \cdot z^2) > -5.36$, cf. first row table 2.5

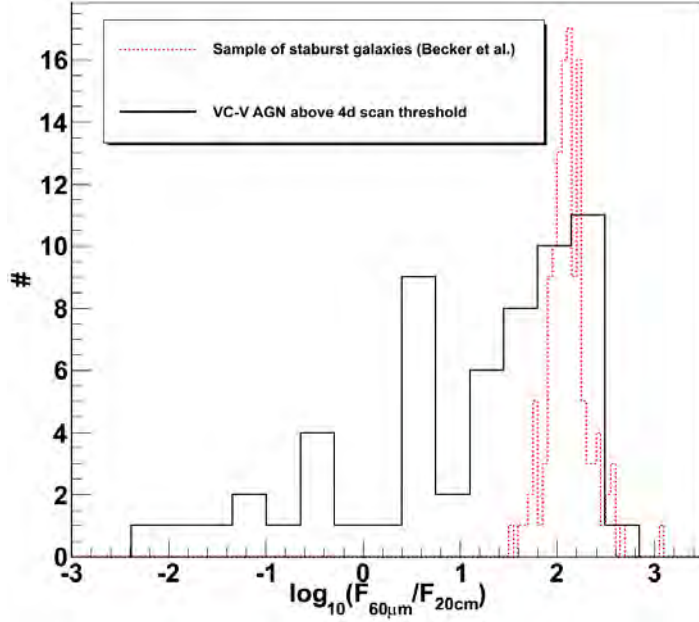


Figure 2.16.: The infrared to radio ratio $R_{\text{FIR}}^{20\text{cm}}$ distribution is shown for VC-V AGN which where selected by the four dimensional scan procedure (black solid line) and a starburst galaxy sample (red dashed line) as given in [114].

scan parameter. Unfortunately, it might be that some radio VC-V AGN are not detected in the infrared and thus would be excluded from the scan. A disadvantage of this would be that AGN with a very weak infrared but very strong radio luminosity might not enter the analysis, but are the most promising UHECR source candidates. To avoid this, it was decided to perform a set of N four dimensional scans in the radio luminosity but with exclusion of radio AGN with $R_{\text{FIR}}^{6\text{cm}} < R_{\text{FIR}}^{6\text{cm}}(N)$. This approach reduces a possible “background” of starburst driven AGN on the one hand (large R_{FIR}), but still considers very strong radio AGN without a measured infrared flux - which would correspond to very small values of R_{FIR} .

The result of this analysis approach is summarized in figure 2.17. Shown is the $R_{\text{FIR}}^{6\text{cm}}$ distribution of VC-V AGN with given flux densities $F_{60\mu\text{m}}$ and $F_{6\text{cm}}$. Again, the corresponding distribution for all VC-V AGN as selected by the four dimensional scan in the radio luminosity is given, too. Furthermore, the minimum probability $P_{\min}(N)$, cf. equation 2.6, of the aforementioned four dimensional scans with exclusion of VC-V AGN with $R_{\text{FIR}}^{6\text{cm}} < R_{\text{FIR}}^{6\text{cm}}(N)$ is shown as function of $R_{\text{FIR}}^{6\text{cm}}(N)$. It is an important difference that the scan range has been extended here to: $0 < z < 0.04$ and $0^\circ < \Psi < 25^\circ$. One can see that P_{\min} drops by two orders of magnitude for AGN with $1 < R_{\text{FIR}}^{6\text{cm}} < 2$. The global minimum of $P_{\min} = 4.69 \times 10^{-9}$ is found for $R_{\text{FIR}}^{6\text{cm}} = 2.05$. The minimum parameters are: $E_{\text{th}} = 58.18$ EeV, $\psi = 5.8^\circ$, $z_{\max} = 0.016$ and $\log_{10}(F_{6\text{cm}} \cdot z^2/\text{Jy}) = -5.43$. It is noteworthy that for $R_{\text{FIR}}^{6\text{cm}} > 2.88$ the minimum parameters do not change and that the parameters are the same than what has been found in the four dimensional scan given in the first row of table 2.10 where the same dataset up to July, 4th 2010 was used. Especially, the redshift and angular separation values remain unchanged although the scan range was increased.

One possible interpretation of these findings might be: the VC-V AGN with $1 < R_{\text{FIR}}^{6\text{cm}} < 2$ play an important role in this correlation study - although many of those are of the unsuspicious Seyfert

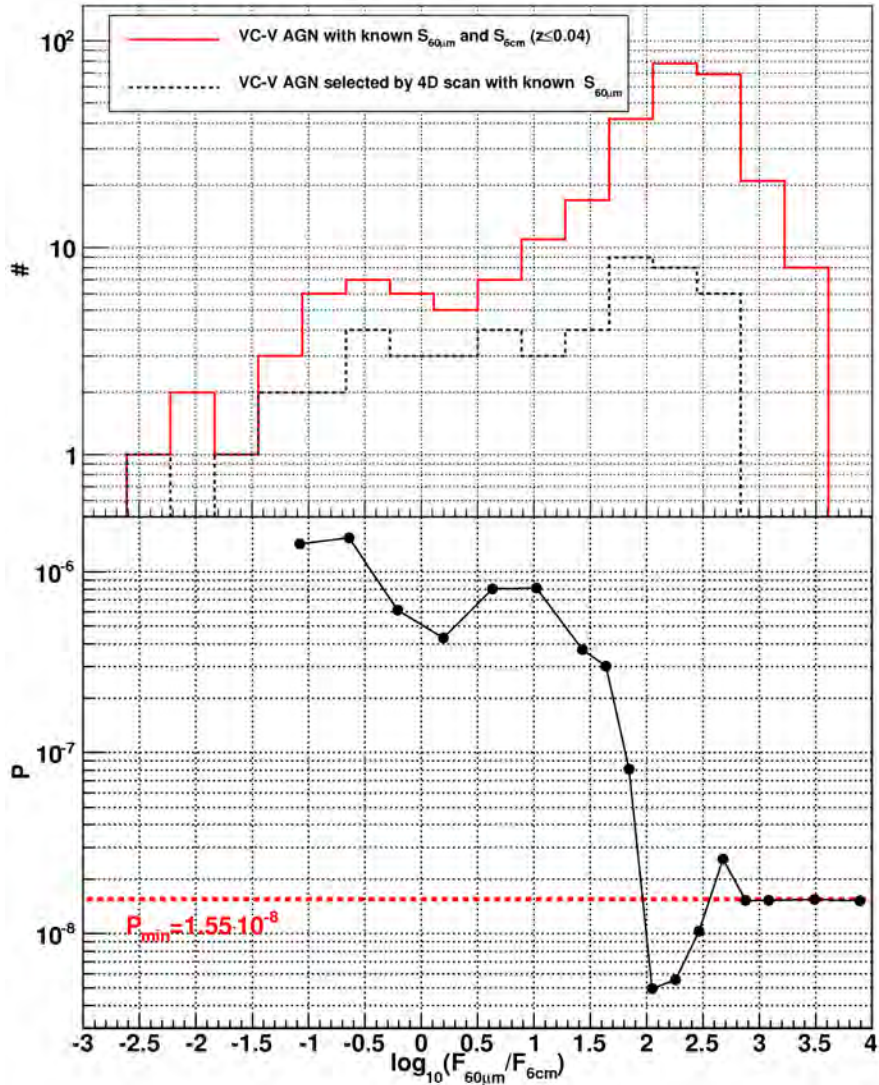


Figure 2.17.: Upper panel: The infrared to radio ratio $R_{\text{FIR}}^{6\text{cm}}$ distribution is shown for VC-V AGN which were selected by the four dimensional scan procedure (black dashed line) and all VCV AGN with $z \leq 0.04$ and known flux densities $F_{60\mu\text{m}}$ and $F_{20\text{cm}}$ (red solid line).

Lower panel: Minimum probability P_{\min} of 17 four dimensional scans (black points) using radio luminosities as the fourth scan parameter with rejection of AGN with a radio to infrared ratio lower than R_{FIR} (which is given on the x axis). The red line marks $P_{\min} = 1.55 \cdot 10^{-8}$ which was found in the four dimensional scan using the complete (independent and exploratory) data set and all radio VC-V AGN ($z \leq 0.024$, c.f. table 2.10).

type. Hence, it is an interesting question if a slightly increased radio to infrared ratio $R_{\text{FIR}}^{\text{6cm}}$ above the starburst average value, presumably interpreted as an indication for jet activity, can be used to further identify the sources of UHECR - a starting point for future analysis work.

Additionally, it might be interesting to exclude the anyway small number of radio loud galaxies from the sample to check whether they contribute to the significance of the correlation signal, or not.

Clearly, the analysis in this sections is a step towards a five dimensional scan procedure. Thus, it is needed to calculate the penalized probability which takes the corresponding, additional trial factors into account. Furthermore, one should redo the luminosity shuffling experiments in order to see if indeed taking into account an upper border on R_{FIR} strengthen the correlation with the UHECR data. These approaches would be close to what has been done in the chapters 2.5 and 2.6 just extended to include a fifth scan parameter.

Summary and Outlook

The three dimensional binomial scan technique as introduced by the Pierre Auger collaboration has been extended to exclude the GPR and to take into account a fourth scan parameter next to energy E , redshift z and angular window ψ . The method has been used to study the correlation between radio VC-V AGN using the radio luminosity $L \propto F_{\text{6cm}} \cdot z^2$ at a wavelength of 6 cm as the fourth scan parameter. With data up to March, 2nd 2008, the observed minimum parameters are: $E_{\text{th}} = 51.92 \text{ EeV}$, $\psi = 5.9^\circ$, $z_{\text{max}} = 0.018$ and $\log_{10}(F_{\text{6cm}} \cdot z^2 / \text{Jy}) = -5.36$. In proper units, this corresponds to a luminosity of $L = 9 \cdot 10^{21} \text{ W Hz}^{-1}$, see equation 2.8.

The penalized probability for this to happen is $P_{\text{pen}} = 0.3\%$. This penalization does not account for multiple trials with different astronomical catalogs or subsets of those.

Random experiments have been performed during which the radio luminosities have been shuffled among subsets of VC-V AGN. They indicate that the radio luminosity indeed increases the correlation strength. Clearly, the results of these shuffling experiments might be effected by the VC-V incompleteness.

The minimum parameters seem to be reasonable stable within the statistical reconstruction uncertainties. But, it seems difficult to estimate the uncertainties on the minimum parameters due to the limited number of events. This is also due to the fact that no physical model is tested and, hence, no predictions about the signal strength can be made.

A SPRT has been constructed to test the hypothesis of isotropy on the basis of the prescribed minimum parameters and an independent data set. This test can be applied after each newly measured event. The error of 1st kind is 0.8% while the error of 2nd kind is smaller than 4.4% for a correlation strength larger than 44%. Using independent data up to July, 4th 2010, the hypothesis test remains undecided.

The radio luminosity shuffling approach has been repeated using only the independent data set. This has the advantage that the prescribed minimum parameters can be incorporated into this analysis. For example the radio luminosity threshold can directly be tested by separating the AGN into a bright and dim class. Furthermore, no complete scan needs to be started as the minimum parameters were already fixed with the exploratory data set. Doing so, an indication is found that the AGN above the threshold show a stronger correlation with the UHECR data than the ones below it.

Note, the SPRT can only test the hypothesis of UHECR isotropy on the basis of the prescribed minimum parameters and the VC-V radio AGN. But, to show that AGN are likely sources of at least some UHECR, one would need a proof that taking into account an intrinsic property (e.g. the radio

luminosity) of the AGN increases the significance of the correlation. The latter is indeed what might be achieved with the luminosity shuffling type of experiments. Ie., if one aims for a prescription, one could combine both analysis tools: the first step would be to confirm anisotropy with the SPRT. The second to show that indeed the radio luminosity can be used to strengthen the correlation signal by applying the luminosity shuffling approach.

Redoing the scan using the complete data set, the energy threshold mainly drops to 40.4 EeV. But, the original minimum with a threshold of 51.92 EeV has a similar significance. Restricting the scan only to the independent data changes the minimum parameters and shows a weaker correlation of $P_{\min} = 1.9 \cdot 10^{-5}$. This might mean that the scan is not yet converged - or that there is no strong correlation with the UHECR data.

It is recommended to further study the correlation of UHECR with radio AGN with a growing data set because the scan might need more data to converge. Furthermore, one could include different catalogs or use different AGN properties as fourth scan parameter. Additionally, it might be interesting to compare some astronomical features of the correlated and uncorrelated AGN or give a closer look to those AGN which have a large fraction of correlations. Similar studies should be done with the subset of correlated and uncorrelated events with respect to their energies and indicators for the UHECR mass, e.g. rise time or curvature.

The radio luminosity threshold for the AGN which was found in the four dimensional scan is $9 \cdot 10^{21} \text{ W Hz}^{-1}$ at a wavelength of 6 cm. This is unexpectedly low and selects VC-V AGN that are no radio loud galaxies in the sense of standard astronomical and morphological classification. Many of these galaxies are of Seyfert type. Thus, the question arises if they show any indication of jet activity - at least on small scales. Indeed, jet activity is the engine of UHECR acceleration in many models and the motivation for the four dimensional scan. A radio signal from jet activity can be separated from one induced by enhanced star forming activity in terms of the infrared to radio ratio $R_{\text{FIR}}^{6\text{cm}}$. To do so, a set of $N = 17$ four dimensional scans with exclusion of AGN with $R_{\text{FIR}}^{6\text{cm}} > R_{\text{FIR}}^{6\text{cm}}(N)$ has been performed. The results indicate that AGN with $1 < R_{\text{FIR}}^{6\text{cm}} < 2$ contribute to the significance of the correlation signal of the four dimensional scan. This approach could be extended to a five dimensional scan procedure. Another interesting point is to explore if the radio AGN are needed in this study or if the tame Seyfert galaxies alone give the major contribution to the correlation in question.

Chapter 3

Towards a Model Testing Procedure

There is one key ingredient missing in today’s UHECR physicist’s toolkit: a complete simulation chain including the modeling of the acceleration, propagation and detection of UHECR [116]. For man made particle accelerators this full simulation chains are standard. For example at the LHC (CERN) the measurement procedure is fully simulated including the full response of the detector assuming a model for the high energy particle interaction. This allows one to give a prediction which can be compared to the measured data.

In case of UHECR physics a comparable simulation chain would have to include a simulation of the acceleration region/model, the voyage of the particle through extragalactic and Galactic environments, the development of the initiated air showers and the detector’s response. In case of Auger a tool which predicts the detector’s response to air showers is available [117]. The high number of particles in these particle cascades can be tracked with the CORSIKA framework which is based on Monte Carlo generators like: QGSJet, Sybill or EPOS [118]. The first release of CORSIKA was in 1989 which was based on routines from the 1970s. On the contrary, for a “similar”, public tool to study the effects of the propagation in extragalactic magnetic fields and background photons fields one had to wait until 2006 when the CRPropa framework was released [119]. This framework was restricted to the simulation of nucleons. As the elongation rate as measured by the Auger collaboration indicates the existence of a component of heavy nuclei at the highest energies [3], an extension of CRPropa to nuclei is needed.

In this chapter, the extension of CRPropa to the propagation of nuclei is described. It starts with a short description of the publicly available CRPropa version 1.3., see section 3.1. This is because many of its features can be inherited to the propagation of nuclei. A guideline how to propagate nuclei within CRPropa is given in section 3.2. One of the major challenges here is the photo disintegration of nuclei which was the main focus of this work. The corresponding procedure is explained in the sections 3.3-3.7¹. Historically, the photo disintegration of UHE-nuclei was studied e.g. in [37]. A recent discussion of the subject is given e.g. in [120]. In the last section, two first applications of nuclei propagation with CRPropa will be presented.

¹Note, no technical details will be discussed here. For those kind of information see e.g. the Doxygen documentation within the CRPropa framework version 2.0.

3.1. A Short Introduction to CRPropa version 1.3

Version 1.3 of CRPropa is a simulation tool to study the propagation of neutrons and protons in the infrared (IRB) and cosmic microwave (CMB) background light [119]. For nucleons the production of electron-, positron pairs (pair production), the photo pion production and neutron decay are taken into account. CRPropa allows for the tracking of secondaries (photons and neutrinos). A module is included that follows the electromagnetic cascades which are initiated by electrons, positrons or photons taking into account: single-, double- and triple pair production as well as upward scattering of low energy background photons by the inverse Compton effect. Synchrotron radiation along the line of sight can be simulated, too. CRPropa provides a one dimensional (1D) and three dimensional (3D) mode. In the latter one, magnetic field- and source distribution can be defined on a 3D grid. This is useful to perform simulations in a realistic source scenario with a highly structured magnetic field configuration as provided by e.g. cosmological simulations. In 1D mode, magnetic fields can be defined to realistically take into account the energy losses due to synchrotron radiation for electromagnetic cascades, too. Furthermore, it is possible to consider the cosmological and the source evolution as well as the redshift scaling of the background light intensity in 1D simulations.

3.2. Propagation of Nuclei with CRPropa: A Guideline

Similar to the case of protons, nuclei carry charge and are linked with an electric field in which the photons from the CMB and IRB background light can be converted into electron-positron pairs. This can happen if the photon energy boosted into the rest frame of the nucleus is of the order of $\epsilon' \sim 1$ MeV. At higher photon energies of the order of the nuclear binding energy or above $\epsilon' \gtrsim 9$ MeV several light nuclei can become photo disintegrated from the nucleus. Starting at energies of ~ 145 MeV the quark structure of single nucleons can be excited to produce pions - similar to the case of free nucleons. In the last two reactions the species of the nucleus is altered and an unstable element might be produced. Hence, nuclear decay has to be taken into account, too. In CRPropa the nucleus is considered as a superposition of A nucleons with an energy E/A . Here A is the mass number. Thus, in case of a mass loss the initial energy E will be equally distributed among the outgoing nucleons and nuclei. Energy E and momentum $|\vec{p}|$ can be related to each other via $E = pc$ at UHE energies. Furthermore, the direction of the initial particle will be given to its nuclear reaction products. This is reasonable as the boost from the rest into the laboratory frame is linked with a strong forward collimation of the particle's direction. Ie., the assumptions is made that the photon provides exactly the right amount of energy to disintegrate parts of the nucleus without changing its momentum. This approach of extending CRPropa to allow for the propagation of nuclei was already outlined in [121]. The remaining features of CRPropa version 1.3 can be reused for the propagation of nuclei with comparably small changes.

Photodisintegration

The photo disintegration of nuclei has no analogy for free nucleons. Hence, it is one of the main changes needed for the propagation of nuclei within CRPropa. It was implemented as a part of this thesis and, hence, will be discussed in much detail in the following sections. A recent publication on the subject is [120]. At this point it should just be mentioned that the mean free path for photo disintegration can be ~ 0.01 Mpc which is essentially smaller than the mean free path for photopion

production on a proton which can become ~ 4 Mpc. Thus, the propagation algorithm of CRPropa was changed in a way that the spatial resolution is automatically adjusted to the interaction length of the particle which is simulated. This is crucial in order to perform simulations on reasonable time scales, s. section 3.8.

Photopion production

Here a simple superposition model is assumed: Due to the needed high energy per nucleon E/A , the nuclear binding energy is neglected and the nucleus is treated as a combination of free nucleons. Following this spirit, the nucleus' cross section $\sigma_{A,Z}$ for photopion production can be based on the corresponding cross sections for free proton σ_p and neutron σ_n

$$\sigma_{A,Z}(E) = Z\sigma_p\left(\frac{E}{A}\right) + (A - Z)\sigma_n\left(\frac{E}{A}\right). \quad (3.1)$$

Here A and Z are the mass- and the atomic number of the nucleus and E is its energy. In section 3.3 a formula will be given to calculate the mean free path for a reaction with a photon from an isotropic photon density for a given cross section, see equation 3.13. Applying this to the cross section of equation 3.1, one yields an expression for the mean free path $\lambda_{A,Z}$ of a nucleus using the mean free paths for neutron and proton λ_p, λ_n

$$\lambda_{A,Z}^{-1}(E) = Z\lambda_p^{-1}\left(\frac{E}{A}\right) + (A - Z)\lambda_n^{-1}\left(\frac{E}{A}\right). \quad (3.2)$$

This simplified the implementation as λ_p, λ_n are already available in version 1.3 of CRPropa. Presently, it is assumed that the excited nucleon leaves the nucleus after a pion production took place. Unstable nuclei which might be created by this approach will be dealt with by a nuclear decay routine which is described later on.

It should be acknowledged that the detailed outcome of pion production reactions in elementary particles as well als the corresponding energy and momentum distributions in CRPropa are predicted with the Monte Carlo generator SOPHIA [122].

Pair production

The pair production is treated as a continuous energy loss in CRPropa. The energy loss e.g. in the CMB can be parametrized as [37]

$$-\frac{dE_{A,Z}^{e^+e^-}}{dt} = 3\alpha\sigma_T h^{-3}Z^2(m_e c^2 kT)f\left[K\frac{A}{E}\right]. \quad (3.3)$$

Here, $K := c^4 m_e m_p / 2/k/T$, σ_T is the Thomson cross section, m_e, m_p are the masses of electron and proton, α is the fine structure constant, and T is the temperature of the CMB. $f(x)$ is a function which was parametrized by Blumenthal [123]. This can be used to express the energy loss $dE_{A,Z}^{e^+e^-}/dt$ of nuclei in terms of the energy loss for protons $dE_{1,1}^{e^+e^-}/dt$. One finds

$$\frac{dE_{A,Z}^{e^+e^-}}{dt}(E) = Z^2 \times f\left(\frac{K}{E}A\right) f^{-1}\left(\frac{K}{E}\right) \times \frac{dE_{1,1}^{e^+e^-}}{dt}. \quad (3.4)$$

According to this scaling relation, the existing routines of CRPropa version 1.3 can be extended to allow for the propagation of nuclei.

Note, the same scaling relation is used for the case of the IRB.

Nuclear decay

In principle it is easy to handle the nuclear decay: the half life times $t_{1/2}$ can be taken e.g. from [124] and can be transformed from the rest frame into the laboratory frame. The decay length is $\lambda_{\text{decay}} = \gamma c t_{1/2} \ln(2)$ where $\gamma = E/M$ is the Lorentz factor. But, it remains an open question how to proceed with nuclei which have a lifetime governed by electron capture as this decay mode can not take place in the UHECR regime - the UHE-nuclei are ionized. Note, in this case the half life time due to another decay channel might not be accessible to a laboratory measurement.

At this point it should be mentioned that the extensions of CRPropa for pion production, pair production and decay of nuclei have been implemented by Jörg Kulbartz from the University of Hamburg.

3.3. Mean Free Path in an Ambient Photon Field.

Photons out of low energy background photon fields can cause interactions of UHECR and UHE-nuclei. This is, because the Lorentz boosted photon energy in the nucleon's rest frame can become large enough to cause e.g. the production of electron positron pairs, the production of mesons - by an excitation of a nucleons' quark structure - or the disintegration of a nucleus. In this section, a formula is derived which allows one to calculate the mean free path λ of a reaction with a known cross section σ in an isotropic photon density. The expression itself was already given in [125]. The derivation was sketched in [126].

The mean free path in case of a fixed target density η (in units of $\#/m^3$) for a reaction with a cross section σ (in units of $1/m^2$) is

$$\lambda = \frac{1}{\eta \sigma}. \quad (3.5)$$

In case of UHECR one deals with the propagation in an ambient photonfield $n = n(\varepsilon)$, e.g. the CMB which can be parametrized by the Planck distribution, see [125] or appendix D

$$\eta(\varepsilon, d\varepsilon) = n(\varepsilon) d\varepsilon = \frac{\varepsilon^2 d\varepsilon}{\pi^2 \hbar^3 c^3 (e^{\varepsilon/kT} - 1)}. \quad (3.6)$$

Here, k is Boltzman's constant and $T = 2.7$ K is the temperature of the CMB. Additionally, an infrared background as parametrized by Primack et al [127] or by Kneiske et al [128] will be available in CRPropa, see figure 3.1. Furthermore, the cross section in equation 3.5 $\sigma = \sigma(\varepsilon')$ is given as a function of the photon energy ε' in the nucleus' rest frame. The energies of the photon in the two considered reference frames can be related to each other via the Doppler equation

$$\varepsilon(\theta, \varepsilon)' = \gamma \varepsilon (1 - \beta \cos \theta) \quad (3.7)$$

$$=: \gamma \varepsilon g(\theta). \quad (3.8)$$

Here θ is the incident angle in the laboratory frame. Due to the angular dependence $g(\theta)$ in equation 3.8, photons from a homogenous, isotropic photon field in the rest frame would appear not isotropic in the nucleus' rest frame. Thus, the differential mean free path $d\lambda$ for $n(\varepsilon_0) d\varepsilon_0$ photons per m^3 in an energy interval $d\varepsilon_0$ at energy ε_0 can be found via equation 3.5

$$d(\lambda^{-1}) = n(\varepsilon_0) d\varepsilon_0 \bar{\sigma}[\varepsilon'(\varepsilon_0, \theta)] \quad (3.9)$$

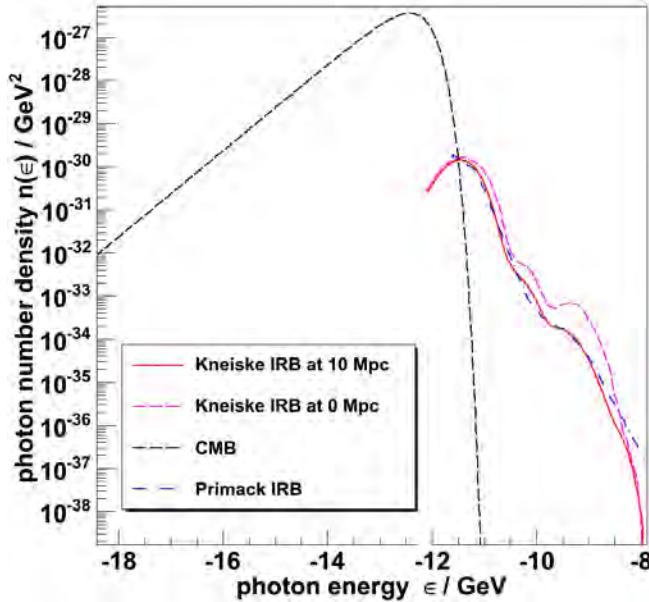


Figure 3.1.: The low energy photon fields are shown which will be available for reactions with nuclei in version 2.0 of CRPropa. Note, Kneiske et al. spherically model the IRB light in the vicinity of a galaxy and, thus, as function of the distance to the galaxy's center. For small distances a contribution from the galaxy itself is added. For very large distances the extragalactic background light becomes dominant. Here, exemplary two distances 0 Mpc, 10 Mpc were chosen. At 10 Mpc the extragalactic background light is the major contribution.

were the averaged cross section $\bar{\sigma}$ is used

$$\bar{\sigma} = \frac{\int d\Omega \sigma[\epsilon'(\epsilon_0, \theta)] g(\theta)}{\int d\Omega g(\theta)} \quad (3.10)$$

$$= \frac{1}{2} \int d\theta \sin(\theta) \sigma[\epsilon'(\epsilon_0, \theta)] (1 - \beta \cos \theta). \quad (3.11)$$

By substitution of equation 3.8, the latter integral can be rewritten as

$$\bar{\sigma} = \frac{1}{2\gamma^2 \beta} \frac{1}{\epsilon_0^2} \int_{\gamma\epsilon_0(1-\beta)}^{\gamma\epsilon_0(1+\beta)} \epsilon' \sigma(\epsilon') d\epsilon'. \quad (3.12)$$

The final expression for the mean free path λ follows from equation 3.9 and equation 3.12 after integration over the photon energy ϵ_0 in the laboratory frame

$$\lambda^{-1} = \frac{1}{2\gamma^2 \beta} \int_0^\infty \frac{n(\epsilon_0) d\epsilon_0}{\epsilon_0^2} \left\{ \int_{\gamma\epsilon(1-\beta)}^{\gamma\epsilon(1+\beta)} \epsilon' \sigma(\epsilon') d\epsilon' \right\} d\epsilon \quad (3.13)$$

In CRPropa $\beta = 1$ is used which changes the borders of the inner integral to start at 0 and end at $\epsilon'_{\max} = 2\gamma\epsilon$. The expression in curly brackets will be called the *averaged* cross section $\sigma_{\text{avg}}(\epsilon'_{\max} = 2\gamma\epsilon)$ in what follows. Note, equation 3.13 depends on the energy E of the nucleus because of the $\gamma = E/M$ factor.

3.4. The Numerical Evaluation

For the numerical evaluation of the mean free path λ it is handy to rewrite equation 3.13

$$\lambda^{-1} = \frac{1}{2\gamma^2} \int_0^\infty \frac{n(\varepsilon, z)}{\varepsilon^2} \cdot \sigma_{\text{avrg}}(\varepsilon'_{\max}) \cdot d\varepsilon, \quad (3.14)$$

$$\sigma_{\text{avrg}}(\varepsilon'_{\max} = 2\gamma\varepsilon) = \int_0^{\varepsilon'_{\max}=2\gamma\varepsilon} \varepsilon' \sigma(\varepsilon') d\varepsilon'. \quad (3.15)$$

Here, $\beta = 1$ was used. Once the cross section σ is given the averaged cross section σ_{avrg} , defined in equation 3.15, can be tabulated as function of the upper border $\varepsilon' = 2\gamma\varepsilon$ of the integral once and for all. Under no circumstance it has to be calculated during a CRPropa simulation. That is the reason for the splitting of equation 3.13 into the two terms 3.14 and 3.15. For given $\sigma_{\text{avrg}}(\varepsilon'_{\max} = 2\gamma\varepsilon)$ the mean free path λ can be calculated with equation 3.14. Indeed, the mean free path λ can be tabulated to gain performance in case of homogenous photon fields, too. But, for an isotropic photon density that scales e.g. as function of the redshift or the spatial coordinates equation 3.14 has to be calculated *on the fly* during a simulation. But, in this case the assumptions that have been made while deriving equation 3.13 should be kept in mind; the photon field should be approximately isotropic in the laboratory frame on scales of the interaction length or propagation step.

The integrations are solved with an 8th order Gauss-Legendre algorithm² using 8 sampling points. For faster convergence, it turned out to be useful to first perform a substitution $t = \ln(\varepsilon/\varepsilon_0)$ in the outer integral of equation 3.14 before calculating it. But still, higher precision is needed to guarantee “overall” convergence for all nuclei. Thus, the integration interval is disjoint into N pieces which become integrated separately (linearity of the integral), cf. section 3.6. One finds

$$\lambda^{-1} = \frac{1}{2\gamma^2} \int_{t_{\min}}^{t_{\max}} \frac{n(\varepsilon(t), z)}{\exp^2(t)\varepsilon_0^2} \cdot \sigma_{\text{avrg}}(\varepsilon'_{\max}(t)) \cdot \exp(t)\varepsilon_0 dt \quad (3.16)$$

$$= \frac{1}{2\gamma^2} \sum_{i=1}^N \int_{t_{\min} + (t_{\max} - t_{\min})(i-1)/N}^{t_{\min} + (t_{\max} - t_{\min})i/N} \frac{n(\varepsilon(t), z)}{\exp(t)\varepsilon_0} \cdot \sigma_{\text{avrg}}(\varepsilon'_{\max}(t)) \cdot dt. \quad (3.17)$$

Here, $\varepsilon(t) = \exp(t)\varepsilon_0$ and $t_{\min/\max} = \ln(\varepsilon_{\min/\max}/\varepsilon_0)$ where $\varepsilon_{\min} = 4 \cdot 10^{-19}$ GeV and $\varepsilon_{\max} = 12.4 \cdot 10^{-9}$ GeV are fixed for the CMB and IRB. The photo disintegration routines can handle variable photon fields by using the tabulated averaged cross sections and solving the outer integral of the last equation on the fly. But, this feature is switched off in version 2.0 of CRPropa where the redshift dependency is approximately taken into account by assuming a *cmb-like* creation and development for CMB and IRB. In this case the mean free path scales as [119]

$$\lambda^{-1} = (1+z)^3 \cdot \lambda[(1+z)E, z=0]^{-1} \quad (3.18)$$

where z is the redshift. According to the last equation, the mean free path at a redshift $z \neq 0$ corresponds to the mean free path calculated with a photon density at $z=0$ and a nucleus energy $E' = E(1+z)$ but scaled with $(1+z)^{-3}$. Combining the last two equations and using $\gamma = E/M$, one finds

²This algorithm was already implemented in version 1.3 of CRPropa. The corresponding FORTRAN routines were just translated to C++.

$$\lambda^{-1} = \frac{M^2(1+z)^3}{2E^2(1+z)^2} \sum_{i=1}^N \int_{t_{\min} + (t_{\max} - t_{\min})(i-1)/N}^{t_{\min} + (t_{\max} - t_{\min})i/N} \frac{n[\exp(t)\epsilon_0, z=0]}{\exp(t)\epsilon_0} \cdot \sigma_{\text{avg}}[2 \cdot \exp(t)\epsilon_0 E(1+z)/M] dt. \quad (3.19)$$

Where M is the mass of the UHE-nucleus. This is exactly the form which is used in the code - that justifies the lengthy notation.

3.5. The Photo-Nuclear Cross Sections

In the previous section, an expression was given to calculate the mean free path λ for a reaction with a cross section σ in an ambient homogenous, isotropic photon field with $n(\epsilon)d\epsilon$ photons per m^3 , see equation 3.13. This expression has to be numerically calculated for the case of the photo disintegration of nuclei. The needed photo nuclear cross sections for the photo disintegration reactions can be evaluated using the publicly available TALYS framework [129]. According to the authors, the nuclear models therein are reliable for mass numbers $A \geq 12$. In spite of that, TALYS can be started for nuclei with $A > 5$ and $N > 2$ where N is the number of neutrons. The TALYS output for $A \leq 56$ has been compared with available measured data. A reasonable agreement was found within a factor of 2 for the integrated cross sections [120]. Note, due to equation 3.13 an uncertainty of a factor of 2 in the cross section σ translates directly to the mean free path. The mass range $A \geq 12$ of TALYS is not sufficient for the UHECR propagation which has to include light nuclei. Beneficially, many light nuclei are unstable. In [130] the photo disintegration cross sections for five nuclei with a mass $A \leq 10$ are given which are considered “stable” in the context of UHECR physics: beryllium-9 (${}^9\text{Be}$), helium-4 (${}^4\text{He}$), helium-3 (${}^3\text{He}$), triton (T) and deuteron (D). Additionally, a parametrization of the total photo nuclear cross section of nuclei as function of the mass number A are given in [131]. A selection out of these cross section parametrizations are the basis for the handling of the photo disintegration in CRPropa.

More precisely, TALYS version 1.0 was started for all light isotopes up to iron³. The list of isotopes was generated using the data from [124]. TALYS was configured to use the models and settings as suggested in [120]. If compared to [120], there might be difference in the cross sections due to a difference in the used TALYS versions. Only nuclei in their ground state were considered. All cross sections were calculated in 500 linear energy bins in the photon energy interval (0.001, 250) MeV. TALYS can be used to predict the disintegration of light nuclei (or combinations of those): neutron (n), proton (p), deuterium (D), tritium (T), helium-3 (${}^3\text{He}$) and helium-4 (α). These are called *exclusive channels*. Here, 78449 exclusive channels were extracted from the TALYS output for all the isotopes of interest. Clearly, not all of this channels need to be tracked in CRPropa. Thus, section 3.7 deals with a rejection procedure for less important channels to allow for a faster simulation.

Here, it was decided to use all available TALYS output ($A > 5$ and $N > 2$). That explicitly includes the output for mass numbers $A \leq 12$. Then the TALYS cross sections were replaced by the cross sections for: ${}^9\text{Be}$, ${}^4\text{He}$, ${}^3\text{He}$, T and D as given in [130]. Note, ${}^9\text{Be}$ was fitted again using data from [132] and the following function up to $\epsilon' = 90$ MeV

$$\sigma_{{}^9\text{Be}}(\epsilon') = A_0 \frac{\sigma_{Tp}}{\alpha_e} \frac{m_p c^2}{B} \frac{(\epsilon'/B - 1)^{3/2}}{(\epsilon'/B)^4} + \sum_{i=1}^3 \frac{A_i \Gamma_i^2}{(\epsilon' - \epsilon_i)^2 + \Gamma_i^2}. \quad (3.20)$$

³In principle it would be no problem to add nuclei heavier than iron to the calculations. Usually, this is not done probably because there is no significant contribution of heavier elements in the measured composition at lower energies, and secondly because iron has the maximum binding energy per nucleon.

Description	value
Γ_1/MeV	$7.277 \cdot 10^{-2}$
ε_1/MeV	2.907
A_1/mbarn	1.200 (fixed)
Γ_2/MeV	3.835
ε_2/MeV	8.527
A_2/mbarn	1.448
Γ_3/MeV	5.199
ε_3/MeV	$2.247 \cdot 10^1$
A_3/mbarn	$8.716 \cdot 10^{-1}$
A_0	$4.985 \cdot 10^1$
B/MeV	$1.686 \cdot 10^1$

Table 3.1.: Results of the fit of equation 3.20 to the total ${}^9\text{Be}$ photo disintegration cross section data from [132].

nucleus	parametrization	comment
D	Rachen [130]	-
T	Rachen [130]	rescaled by factor 1.7
${}^3\text{He}$	Rachen [130]	rescaled by factor 0.66
${}^4\text{He}$	Rachen [130]	-
${}^7\text{Li}$	measured data [133, 134]	linear approximation between measured data points
${}^8\text{Li}$	Geant4 [131]	loss of 1 neutron
${}^9\text{Li}$	Geant4 [131]	loss of 1 neutron
${}^9\text{Be}$	Rachen [130]	parametrization taken from [130] (refitted with data from [132])
${}^7\text{Be}$	Geant4 [131]	loss of 1 proton
${}^{10}\text{Be}$	Geant4 [131]	loss of 1 neutron
${}^{11}\text{Be}$	Geant4 [131]	loss of 1 neutron
${}^8\text{B}$	Geant4 [131]	loss of 1 proton
${}^{10}\text{B}$	Geant4 [131]	loss of proton or neutron (both with the same rate)
${}^{11}\text{B}$	Geant4 [131]	loss of 1 neutron
${}^9\text{C}$	Geant4 [131]	loss of 1 proton
${}^{10}\text{C}$	Geant4 [131]	loss of 1 proton
${}^{11}\text{C}$	Geant4 [131]	loss of 1 proton

Table 3.2.: Photo disintegration cross sections of nuclei with mass number $A < 12$ should not be calculate with TALYS. Here, the light nuclei which were used to replace and supplement the TALYS predictions in this case are listed and the source of the parametrizations are given.

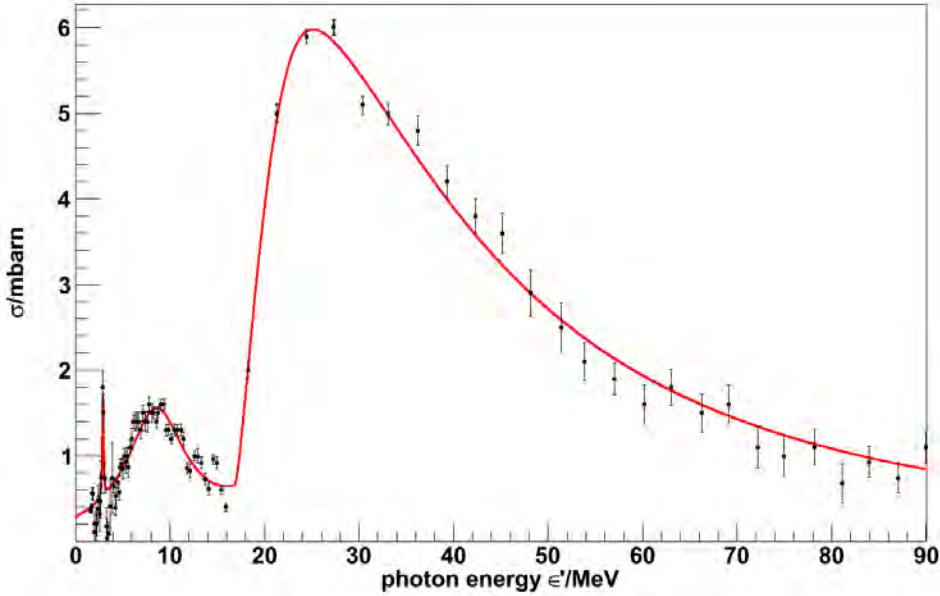


Figure 3.2.: Photo disintegration cross section parametrization for ${}^9\text{Be}$ as obtained by fitting equation 3.20 (red line) to measured data (black dots) from [124].

This parametrization was suggested in [130]. The sum consist of one Lorentz curve L_i for each peak in the cross section, cf. figure 3.2. The peaks are labeled with a growing integer from small to large photon energies ϵ' . The first term of equation 3.20 is important to describe the decrease after the 3rd peak. $(\epsilon'/B)^4$ instead of $(\epsilon'/B)^3$ has been used in the denominator of the first term because it fits the data better. The free parameters are: Γ_i , ϵ_i , A_i , B and A_0 . In order for the fit to work, the amplitude $A_1 = 1.2 \text{ mbarn}$ of the first peak had to be fixed. The remaining constants have been taken as given in [130]. The fit results are summarized in table 3.1. Clearly, this is not a proper model for the ${}^9\text{Be}$ cross section but a reasonable parametrization for what follows. The yielded ${}^9\text{Be}$ cross section parametrization is shown in figure 3.2. Additionally, the available measured exclusive channel data for Lithium-7 (${}^7\text{Li}$) has been collected [133, 134] and a linear approximation between the measured points is used instead of a parametrization. Moreover, the TALYS output for some light nuclei has been replaced using the parametrization of the total photo nuclear cross section as given in [131]. In this cases the loss of one proton, neutron is assumed if $N < Z$, $N > Z$ respectively. If $N = Z$, the loss of one neutron or proton is modeled with equal probability.

A list of all nuclei for which the TALYS output had been replaced or supplemented is given in table 3.2. If this collection of cross section is *complete* in the sense that no light nuclei will be created which are subject to a photo disintegration but with no available or trustworthy cross section, will be cross checked in section 3.9.1. Graphs which show the cross sections which are listed in table 3.2 can be found in appendix E.

3.6. Overall Convergence of the Mean Free Path Calculations

Once the photo disintegration cross sections for the interesting isotopes are available, the mean free path λ can be calculated by firstly evaluating equation 3.15 and tabulate the yielded average cross

section σ_{avg} . Then, these tables can be used to calculate the inverse mean free path λ^{-1} itself using equation 3.14 in a second step. Both integrals are numerically solved by applying an 8th order Gauss Legendre algorithm with 8 sampling points.

As the first integration - the one to yield σ_{avg} - never has to be performed during a CRPropa simulation, one can perform a very time consuming, accurate calculation and store the values for later usage. Here, this is done by dividing the integration interval into $N = 63$ parts and call the integrator for each division. As each of these calls provides 8 sampling points S , one ends up with $S(N = 63) = 504$ sampling points. This number roughly corresponds to the number of linear photon energy bins for the cross sections tables created with TALYS. Hence, a larger number of sampling points would not increase the accuracy.

In case of the integration of equation 3.14, which folds σ_{avg} with a photon field to calculate λ , the situation is a little bit different. Firstly, the number of needed sampling points will surely depend on the chosen integration interval $(\epsilon_{\min}, \epsilon_{\max})$ which can replace the integration interval $(0, \infty)$ because the photon density goes to zero in both of these limits. Secondly, in case of variable photon fields this integration has to be performed on the fly. Thus, it is important to adjust the number of sampling points to yield the needed accuracy but also have fast simulations⁴. Thus equation 3.14 was rewritten again by subdividing the integration region in N division which are integrated separately, see equation 3.19. Accordingly one can calculate the inverse mean free path $\lambda_i^{-1}(E)$ for all i exclusive channels and $N = 1, 2, 3 \dots 30$. For the cases $N = 1, 3$ and 30 the iron total mean free path $\lambda(E, N) = (\sum_i \lambda_i^{-1})^{-1}$ for a redshift $z = 0$ and 200 energy bins is shown in figure 3.3(a). Clearly, a choice of $N = 1$ or 3 is not sufficient. To become more quantitatively, the relative difference $\Delta\lambda_N(E) = |\lambda(E, N) - \lambda(E, N + 1)|/\lambda(E, N + 1)$ can be calculated. As an example this is done for all isotopes and for $N = 29$ in figure 3.3(b). That means that there are entries for 287 isotopes in each γ bin. Herein, the maximum $\max_{E, A, Z}(\Delta\lambda_N(E))$ for all energies E and isotopes (A, Z) has been marked in red. To get a better idea about the convergence, figure 3.3(c) holds a graph showing $\max_{E, A, Z}(\Delta\lambda_N(E))$ as function of N . Exemplary, four power law functions fixed at the point for $N = 1$ are given, too. Qualitatively the calculations converge somewhat faster than N^{-2} . For $N = 30$ the maximum relative difference already dropped below 10^{-3} . But, this is the maximum, whereas figure 3.3(b) suggest that the average relative deviation is much lower.

Thus, the mean free path tables for the case of constant photon fields have been calculated using $N = 30$. For the on the fly calculation, the user can adjust N according to his needs when configuring his CRPropa simulation. $N = 17$ seems to be a reasonable default value.

3.7. The Thinning Options

In section 3.5 a collection of photo disintegration cross sections for 287 isotopes up to iron were presented. It consists out of 78449 exclusive reaction channels. But, just because TALYS can predict the cross section for this huge amount of channels does not mean that they are likely to be triggered during a simulation. Clearly, the Monte Carlo procedure rapidly slows down with an increasing number of channels to be sampled. That suggests that a thinning procedure for the exclusive channels is needed to sort out unlikely ones. This is illustrated in figure 3.4(a) where the mean free path for iron (color coded) as function of mass and charge loss for an energy of $E = 1.2 \cdot 10^{21} \text{ eV}$ is displayed. The corresponding mean free path values range over many decades and surely not all of these reaction

⁴In case of variable photon fields it might be useful to try an integration routine of higher order in the future.

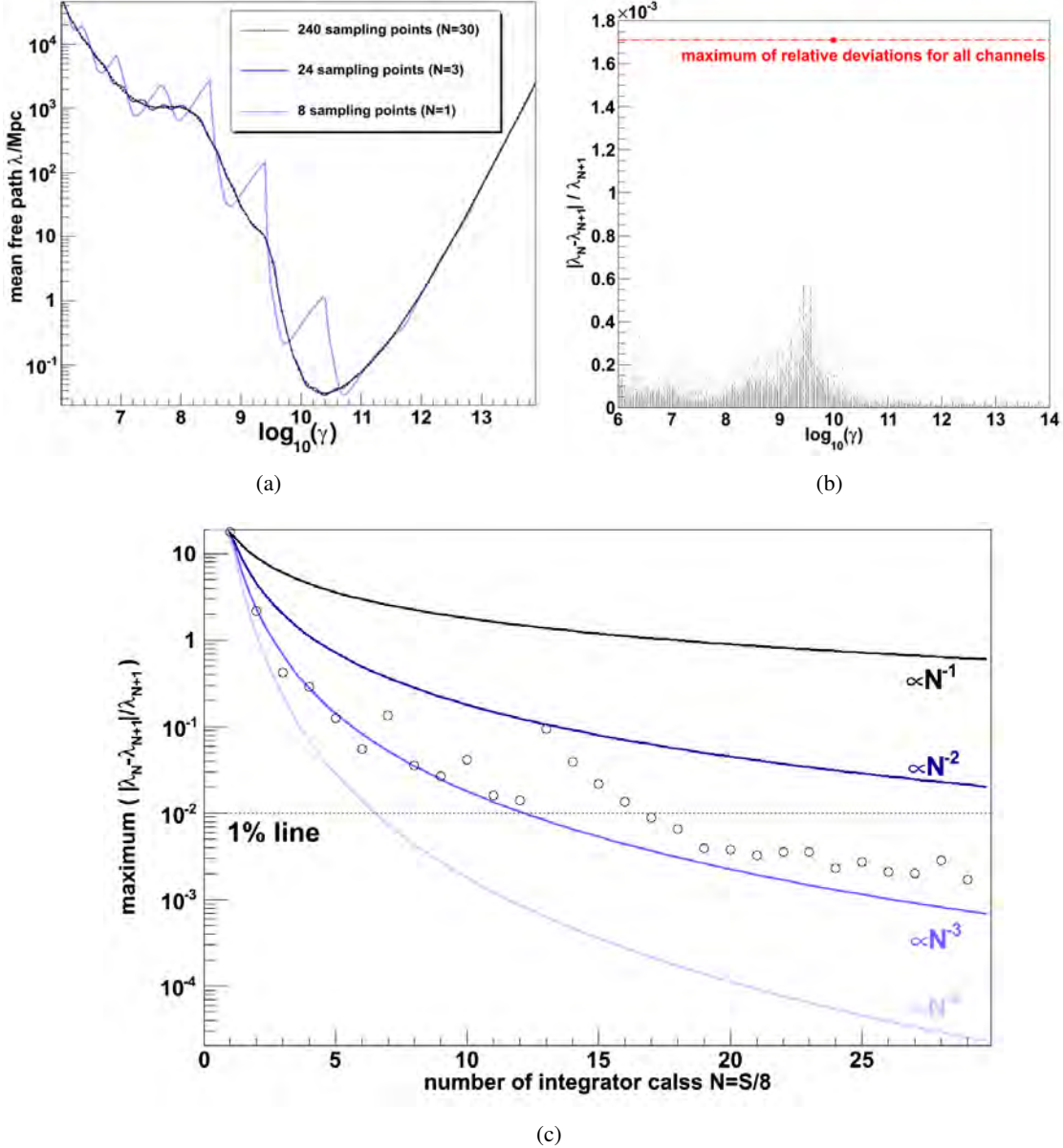


Figure 3.3.: (a) The mean free path λ at redshift $z = 0$ for iron using different numerical accuracies: 8, 24 and 240 sampling points S (which corresponds to $N = 1, 3$ and 30 integrator calls). Note, as each call of the integration routine adds eight sampling points to the numerical integration, the number of sampling points is $S = 8 \cdot N$. The relative deviation of the total mean free paths $\Delta\lambda$ for 232 and 240 sampling points for all nuclei is given in (b). The maximum deviation $\max[(\lambda_N - \lambda_{N+1})/\lambda_{N+1}]$ is marked with a red dot. This maximum deviation is given as function of the number of sampling points in graph (c).

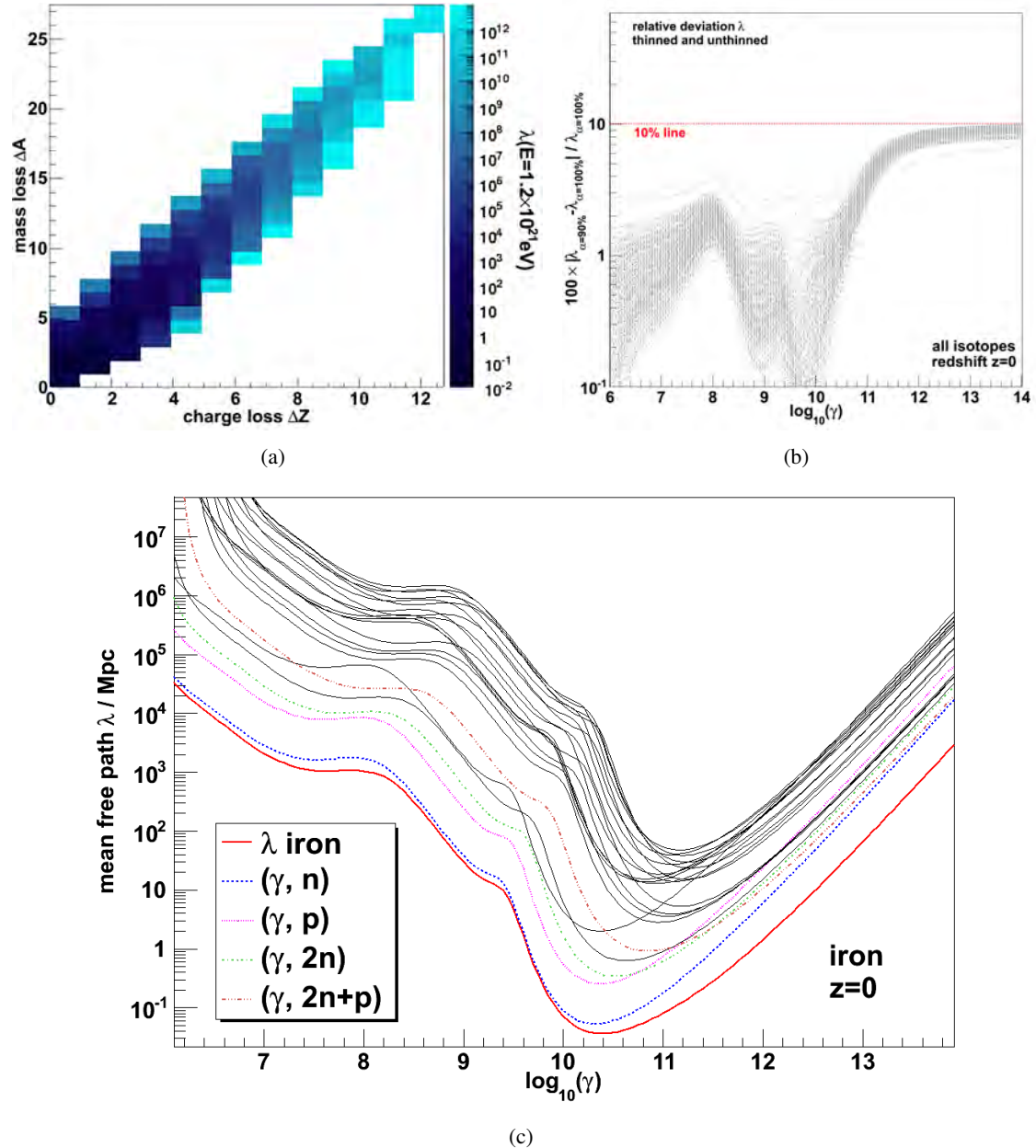


Figure 3.4.: Loss of mass ΔA and charge ΔZ for iron in photo disintegration reactions in the CMB at redshift $z = 0$. The mean free path λ is color coded for a primary iron energy of $E = 1.2 \cdot 10^{21} \text{ eV}$ (a). The relative deviation of the total mean free path λ in CMB and IRB for the thinned ($\alpha = 90\%$) and not thinned case is given for all isotopes (b). Total mean free path λ for iron and the contributions from the exclusive channels - only the most important channels are labeled (c).

channels are needed. Here, the following approach is applied to select *important* exclusive channels: For each isotope

- order the N exclusive channels using σ_{avrg}^N (descending) for each energy,
- calculate the total cross section $\sigma_{\text{avrg}}^{\text{tot}} = \sum_i^N \sigma_{\text{avrg}}^i$ for the isotope,
- select the $n < N$ channels which contribute to the ordered sum $\frac{\sum_i^n \sigma_{\text{avrg}}^i}{\sigma_{\text{avrg}}^{\text{tot}}} > \alpha$ in *one* energy bin.

Herein, α is the thinning factor. Of course, this approach can also be applied to the inverse mean

Description	# no thinning	# thinning (90%)
# exclusive channels	78449	6440
# cross section data points	15689800	1288000

Table 3.3.: Comparison of the amount of data linked with the thinned and not thinned cross section data.

free path tables - the case which will be considered now: here, with a thinning factor of $\alpha = 90\%$. The relative difference between the thinned and not thinned mean free path tables for all isotopes is given in figure 3.4(b). The maximum relative deviation is $\sim 10\%$. To avoid confusion, channels are considered important - i.e. are included - if they are of importance in at least *one* energy bin. Thus, a $\alpha = 90\%$ thinning can be linked with a relative deviation of $< 10\%$ of the mean free path in some energy bins.

Finally, figure 3.4(c) shows the total mean free path λ for all important iron channels at a redshift of $z = 0$ as function of the nucleus' logarithmic γ factor. It can be seen that the loss of one nucleon dominates the total mean free path λ at low energies while at larger energies the boosted photon can provide enough energy to disassociate more and/or heavier nuclei.

Exemplary, the mean free path of five nuclei which have a high abundance in Galactic cosmic rays are given in figure 3.5. The effect of different assumptions for the IRB are illustrated, too.

3.8. Propagation Algorithm (Automatic Step Size)

A different propagation algorithm has been implemented in version 2.0 of CRPropa compared to version 1.3⁵. The underlying assumption is that the considered photon fields are approximately constant within each propagation step. From that it follows that the mean free path is only a function of the particle's energy $\lambda = \lambda(E)$. Indeed, the energy can be modified during the propagation by the continuous energy loss via pair production. Thus, the propagation algorithm has to make sure that the step size is kept small enough so that no significant energy loss occurs. More concrete the algorithm works as follows:

Given the mean free path λ_i for nuclei interactions where i enumerates e.g. decay λ_{decay} , pion production λ_π and photo disintegration λ_{PD} :

⁵This has been done in cooperation with J. Kulbartz and G. Sigl from DESY Hamburg who also suggested this approach.

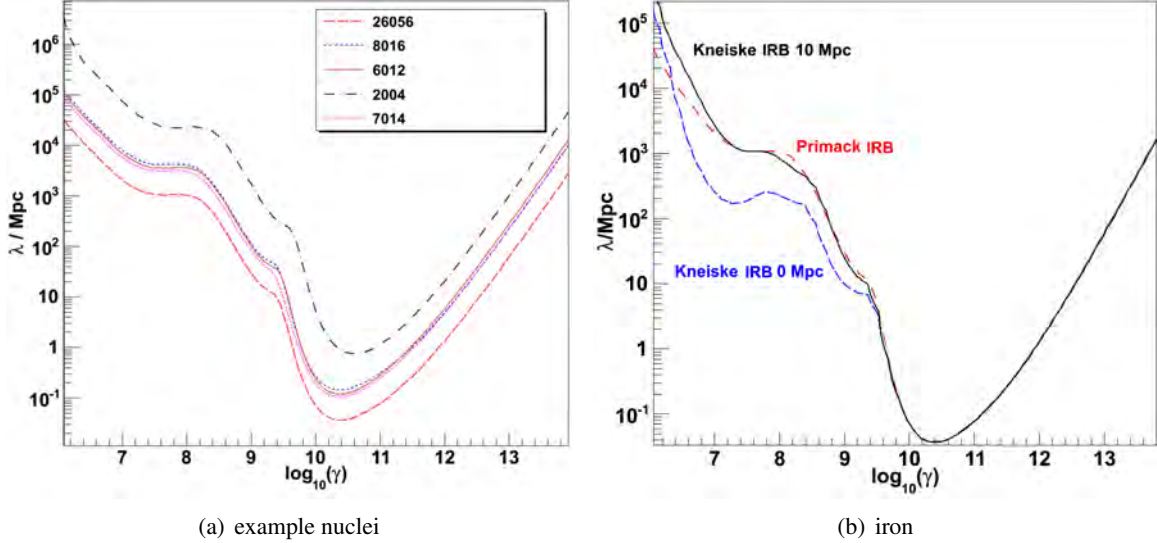


Figure 3.5.: The mean free path λ as function of the nucleus $\gamma = E/M$ is exemplary given for some stable nuclei at redshift $z = 0$ in (a). Herein, the nuclei are labeled with an identifier $Z \cdot 1000 + A$ where Z, A are atomic- and mass number. The mean free path for iron with different parametrizations for the IRB is shown in (b), cf. figure 3.1.

- Calculate the inverse overall mean free path $\lambda_{\text{tot}}^{-1} = \sum_{i=1}^3 \lambda_i^{-1}$ and toss a distance Δx to the next reaction using a uniform random number $r \in (0, 1)$ via

$$\Delta x_1 = -\lambda \ln(1 - r). \quad (3.21)$$

Note, this equation can be easily derived assuming an exponential path length distribution and using equation 2.4.

- Guarantee a constant particle energy by using a constraint for the relative energy loss by pair production

$$\frac{\int_x^{x+\Delta x_2} dx \frac{dE_{A,Z}^{e^+ e^-}}{dx}(E)}{E} < \delta. \quad (3.22)$$

This should be understood as a conditional equation to determine Δx_2 . For small δ the energy E will be approximately constant on the propagation distance Δx_2 and so will be the mean free path $\lambda(E)$, cf. section 3.2 for details on the treatment of pair production.

- Propagate the particle by a distance

$$\Delta x = \min(\Delta x_1, \Delta x_2, \Delta x_3), \quad (3.23)$$

where $\Delta x_1, \Delta x_2$ are explained above and Δx_3 is an upper limit on the propagation step which can be given by the user - usually ~ 1 Mpc.

- Choose an interaction by finding the index i' of the reaction that obeys

$$\sum_{a=1}^{i'} \frac{\lambda_{\text{tot}}}{\lambda_a} > w \quad (3.24)$$

again on the basis of an uniform random number $w \in (0, 1)$.

Thus, if at least one of the interaction has a small mean free path λ_i , the step size of the propagation will adjust itself automatically.

Clearly, this approach can also be applied to organize the selection of an exclusive channel in case of a photo disintegration. That is, if a photo disintegration is chosen to be the next reaction by the propagation algorithm the exclusive channel is chosen by the use of equation 3.24. In analogy, here $\lambda_{\text{tot}} = (\sum_i \lambda_i^{-1})^{-1}$ is the total mean free path for the isotope under consideration. The λ_i are the mean free path values for the exclusive channels of the corresponding isotope.

3.9. Applications of CRPropa

After the preliminary version of CRPropa 2.0 (beta) was ready, a huge number of simulations were started using a large variety of possible settings. The results were compared with results for CRPropa 1.3., in the case of proton simulations, or with the literature if available. A reasonable agreement was found. Not all these example applications can or should be discussed here. Anyway, as a proof of principal a selection of two interesting example applications will be discussed in this section.

3.9.1. Completeness of the Photo Disintegration Cross Section Data

In section 3.5 a compilation of photo disintegration cross sections for nuclei up to iron was introduced. It is difficult to decide which nuclei have to be included into the reaction chain because this depends on their probability to be created and on their half life time. If the compilation of cross section as presented in section 3.5 is consistent in this sense, can be cross checked using an exemplary simulation.

In a one dimensional test simulation 10000 iron nuclei with an E^{-1} spectrum were injected from an uniform source distribution up to a distance of 1000 Mpc from the observer. The energy range of the particles was $[1; 56 \cdot 10^3]$ EeV. During the simulation run all particles that were created and propagated within CRPropa are tracked using a two dimensional histograms displaying the occurrence of particles as function of mass and atomic number A, Z , see figure 3.6-3.8. All figures hold symbols which mark nuclei that have photo disintegration cross sections within CRPropa. Note, the type of the marker indicates the source of the cross section as listed in section 3.5, too. In each graph, lines are given which indicate the reliability limits of TALYS according to [129] (green), Allard et al. [120] (yellow) and the working range of TALYS: $A > 6$ and $N := A - Z > 2$ (green).

- In figure 3.6, one can see atomic and mass numbers Z, A of all nuclei which **undergo a photo disintegration reaction** during a simulation. Of course, nuclei with missing photo disintegration cross section can not appear in this plot. Anyway, one can see that many light nuclei which were considered unstable by the authors of [130] add a small contribution. Furthermore, some light nuclei which were added are not triggered at all in this example simulation.
- In figure 3.7 the mass and atomic numbers of nuclei were tracked which were **altered in a photo disintegration reaction** during the simulation. Most importantly three nuclei (${}^5\text{He}$, ${}^5\text{Li}$ and ${}^9\text{B}$) are created for which no photo disintegration cross sections are available. As their half life time is smaller than 10^{-15} s this is not problematic [124] - they will decay.

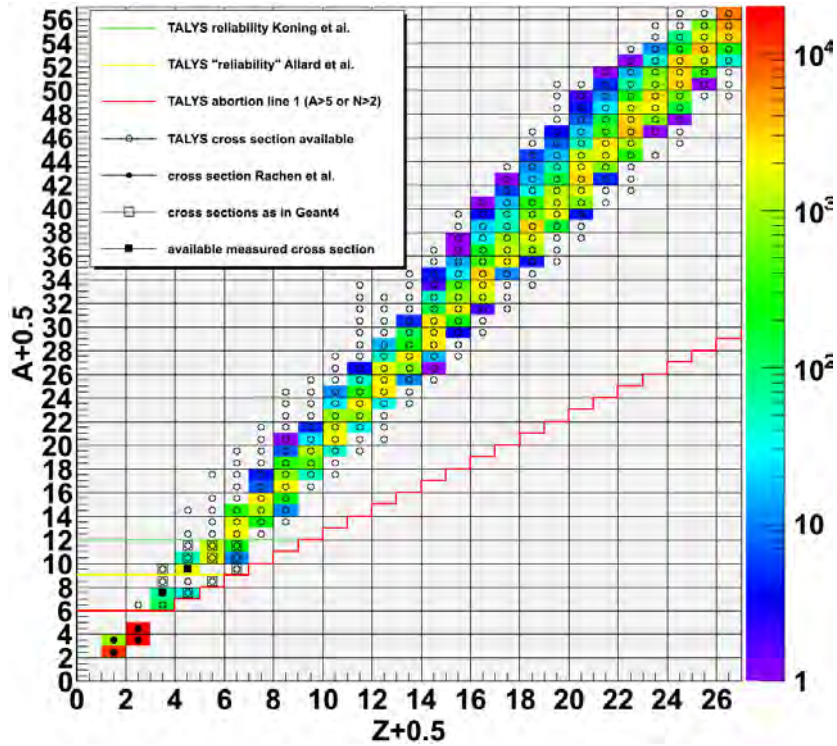


Figure 3.6.: Color coded the number of occurrence of nuclei which suffer a photo disintegration in a CRPropa simulation is given as function of atomic- Z and mass number A . See text for further explanation.

- At last, figure 3.8 holds nuclei which were **created in all kind of reactions** which are tracked in CRPropa. Above the green and red lines are some nuclei which become created but do not have a photo disintegration cross section. This is not problematic as all of them are far of the valley of stability and can be expected to decay very fast. A closer look at the remaining light nuclei suggest that five of them become created which can not be treated due to unavailable cross section data: ${}^5\text{He}$, ${}^5\text{Li}$, ${}^9\text{B}$, ${}^7\text{He}$ and ${}^6\text{Be}$. Again, all these nuclei have a half life time smaller than 10^{-15} s and, hence, are not a subject to photo disintegration, too. Note, due to mass- and charge loss by pion production “nuclei” which consist only out of neutrons or protons can be observed. This is a technical artifact and those nuclei will immediately decay in CRPropa, too [135].

Thus, this basic example simulation suggests that the compilation of cross sections is complete for an application in UHECR physics. Clearly, the injection of other isotopes might alter the figures which were discussed in this chapter. So, it might be useful to create the presented plots by default during a simulation to allow for a fast verification. Note, that it is possible for the experienced users themselves to add photo nuclear cross section data if needed.

3.9.2. Propagation Matrix and X_{\max} Interpretation

Already in the foreword of this thesis and later in the introduction to this chapter, the need for a full simulation chain in UHECR physics has been emphasized. This Monte Carlo chain should take into

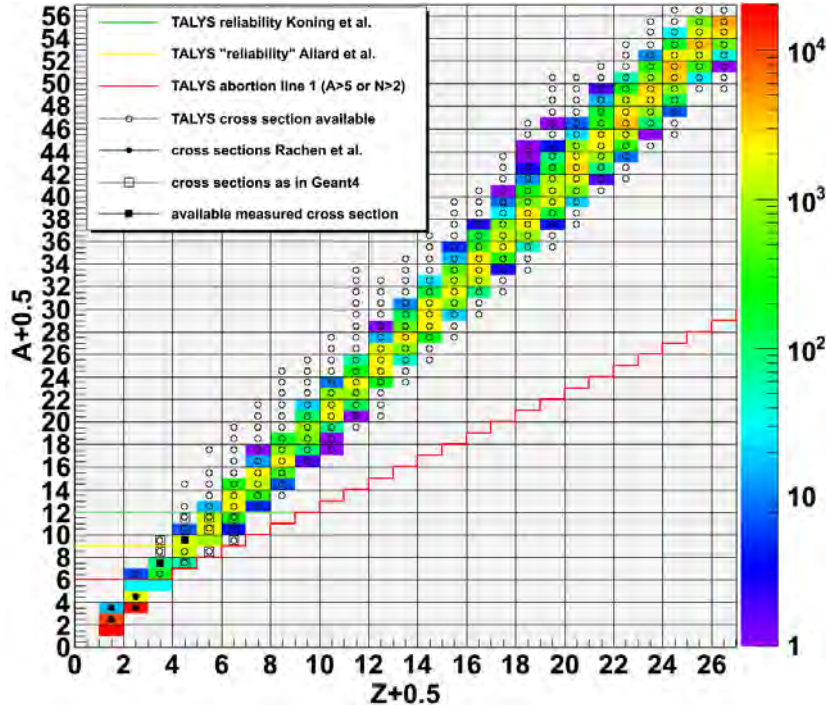


Figure 3.7.: Distribution of altered atomic and mass numbers of mother nuclei that were undergoing a photo disintegration reaction. The number of occurrences is color coded. See text for further explanation.

account the injection, propagation and detection of UHECR. A first analysis of this kind is currently performed by the Pierre Auger collaboration. Here, the aim is to simultaneously fit the measured energy spectrum and X_{\max} data to constrain the spectrum's slope α , the cut off energy E_{cut} , and the abundance a_i of an element i at the UHECR source [136]. One ingredient to this analysis is the so called *propagation matrix* which will be explained in more detail later. Shortly, all effects of the propagation of UHECR are summarized in this matrix. Hence, it can be used to predict the energy spectrum $N(E_{\text{cut}}, \alpha, \vec{a}|E_{\text{obs}})$ and the mass distribution $A(E_{\text{cut}}, \alpha, \vec{a}|E_{\text{obs}})$ on top of our atmosphere. Here, the abundance of the individual elements a_i is summarized in the vector \vec{a} , and E_{obs} is the energy of the UHECR at Earth. The mass distribution A can then be transformed into a X_{\max} distribution using CORSIKA air shower simulations and a PAO detector simulation. The best guess for the parameters $E'_{\text{cut}}, \alpha', \vec{a}'$ at the source are those which minimize a χ^2 -function $\chi^2(E'_{\text{cut}}, \alpha', \vec{a}')$ which test the degree of agreement between the predicted and measured UHECR data. For more details on the general scheme of this analysis see [136].

Recently a propagation matrix on the basis of the code presented e.g. in [120] was used in this analysis. Here, an alternative matrix is derived with the beta version of CRPropa 2.0. This is a valuable cross check of the previous results which will presumably contribute to a full author list paper by the Auger collaboration. In this paragraph the definition and creation of a propagation matrix with CRPropa will be explained. At first four charge groups are defined: proton $p=\{0 \leq Z \leq 1\}$, Helium $\text{He}=\{2 \leq Z \leq 3\}$, CNO $=\{4 \leq Z \leq 13\}$ and iron $\text{Fe}=\{14 \leq Z \leq 26\}$. Then, one dimensional CRPropa simulations have been performed with a continuous source distribution, an initial spectrum of E^{-1} and a cut off energy $E_{\text{cut}} = Z \cdot 10^3 \text{ EeV}$ which depends on the atomic number Z . As a simulation

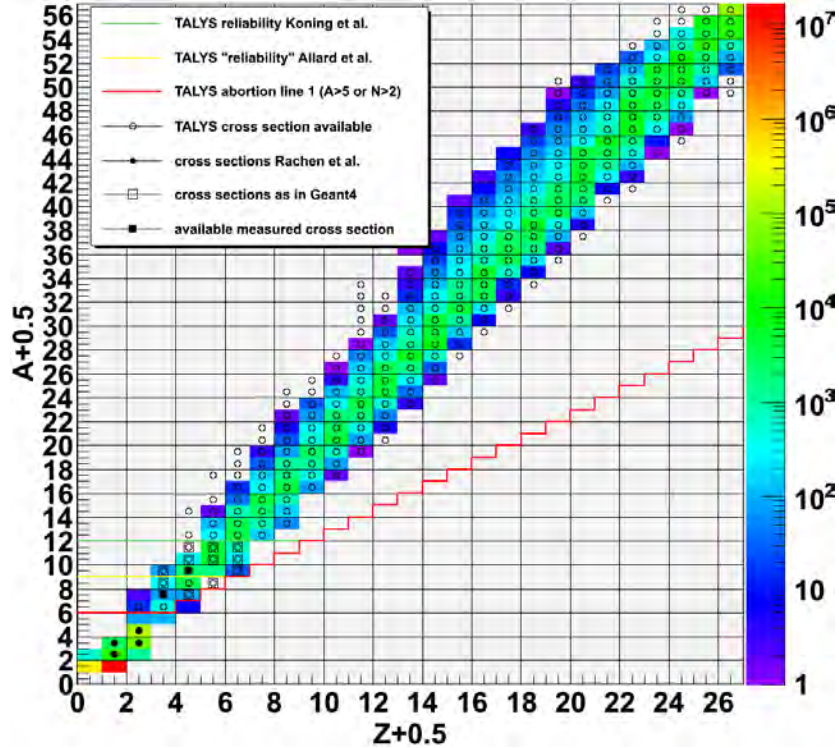


Figure 3.8.: Number of particles that were part of the CRPropa simulation as function of mass- and atomic number. Color coded the number of occurrences is given. See text for further explanation.

of all elements would be too time exhaustive, it was decided to focus on seven representatives with a high abundance at lower cosmic ray energies: p, He, O, C, Mg, Si and Fe. Thus O, C, Mg are the input for the CNO charge group and Si, Fe are the representatives for the Fe charge group. One matrix element is defined as a two dimensional histogram which holds the number of occurrences of particles as function of their energy at the observer E_{obs} and the energy of the mother nucleus at the source E_{src} . As here four charge groups Z_i are considered there are $4 \times 4 = 16$ charge transitions each linked with one matrix element. As no charge is gained during the simulation matrix elements $Z \rightarrow Z'$ with $Z' > Z$ do not have entries. The corresponding upper triangular CRPropa propagation matrix is displayed in figure 3.9. Using reweighting techniques and clever summing of the matrix elements, one can predict the energy spectrum and mass distribution of UHECR on the top of the atmosphere as function of the parameters at the source [136].

Note, the cosmological expansion and the corresponding change in the source density as function of the redshift z was taken into account in these simulations. The effect on the number of detected particles as function of the redshift for the exemplary case of proton can be seen in figure 3.10. For the case of no interaction the number of protons should follow

$$\frac{dN}{dz} = \frac{dN}{dt} \frac{dt}{dz} = \frac{dN}{dt} \frac{1}{(1+z)H(z)}. \quad (3.25)$$

$H(z)$ is the Hubble constant

$$H(z)^2 = H_0^2 [\Omega_m(0)(1+z)^3 + \Omega_r(0)(1+z)^4 + \Omega_V(0) + \Omega_k(0)(1+z)^2] \quad (3.26)$$

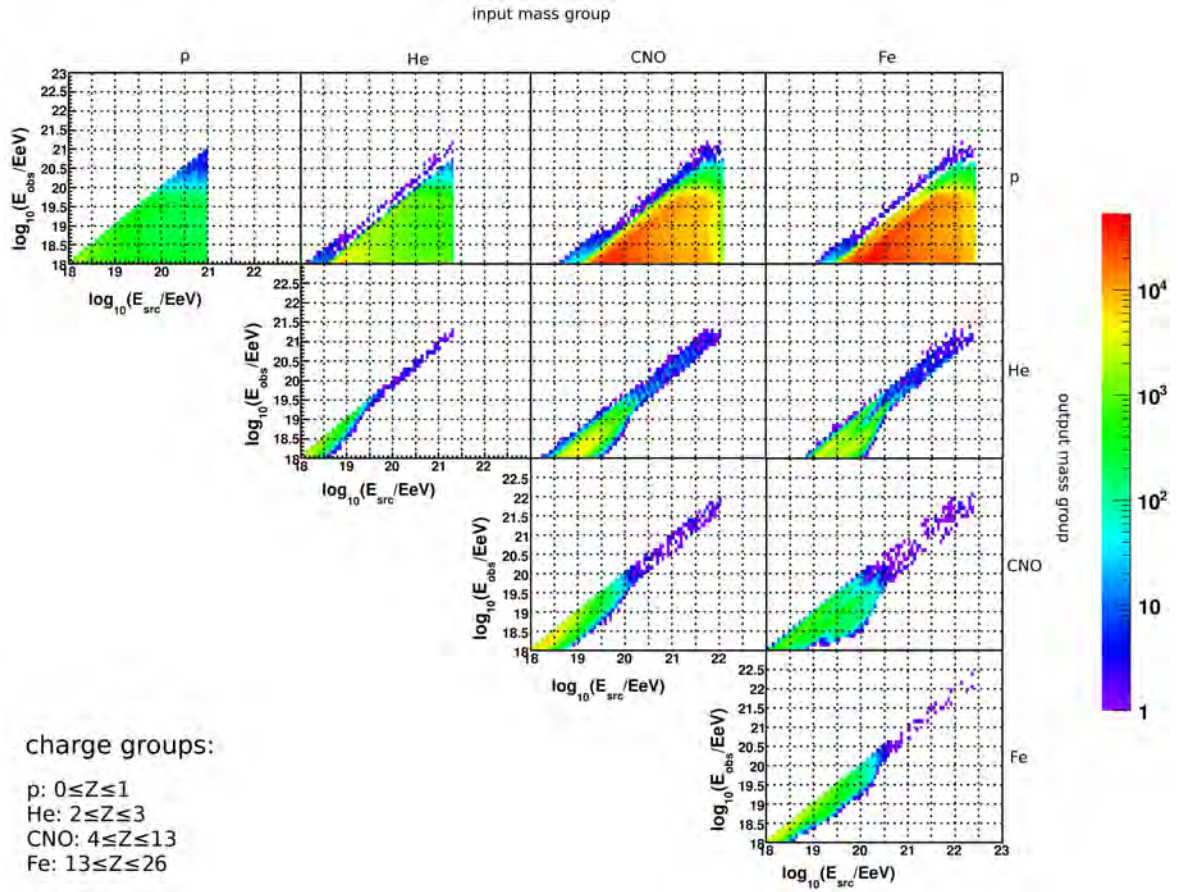


Figure 3.9.: The propagation matrix as calculated with CRPropa. Explanation see text.

which depends on the cosmological parameters: the density of matter Ω_r , radiation Ω_r , vacuum Ω_V and the curvature Ω_k . These are results from standard cosmology which are presented e.g. in [137]. Here, the cosmological density parameters were: $\Omega_m(0) = 0.3$, $\Omega_r = 0$, $\Omega_V = 0.7$ and $\Omega_k = 0$. Furthermore a cosmological constant of $H_0 = 65 \cdot \text{km} \cdot \text{s}^{-1} \cdot \text{Mpc}^{-1}$ is used in CRPropa. The factor dN/dt is often referred to as the *source evolution* as it describes the change of UHECR source number as function of time. In this simulations no source evolution was taken into account, that is $dN/dt = \text{const.}$

At last, it is noteworthy that the relative difference between the two available propagation matrices is smaller than 2% and that the predicted spectra are comparable [138].

Summary and Conclusion

A general scheme was outlined to extend the publicly available code CRPropa version 1.3 to allow for the propagation of nuclei. In this thesis the main focus was the implementation of the photo disintegration routines. Therefore, 78449 exclusive photo disintegration channels for 287 nuclei lighter than iron were collected and are the data basis of this implementation [129, 130, 131]. Somewhat problematic is the regime of light nuclei ($A \leq 12$) where model predictions with TALYS become unreliable. At higher nuclei masses the cross sections seems to be correct within a factor of ~ 2 [83]. At this end

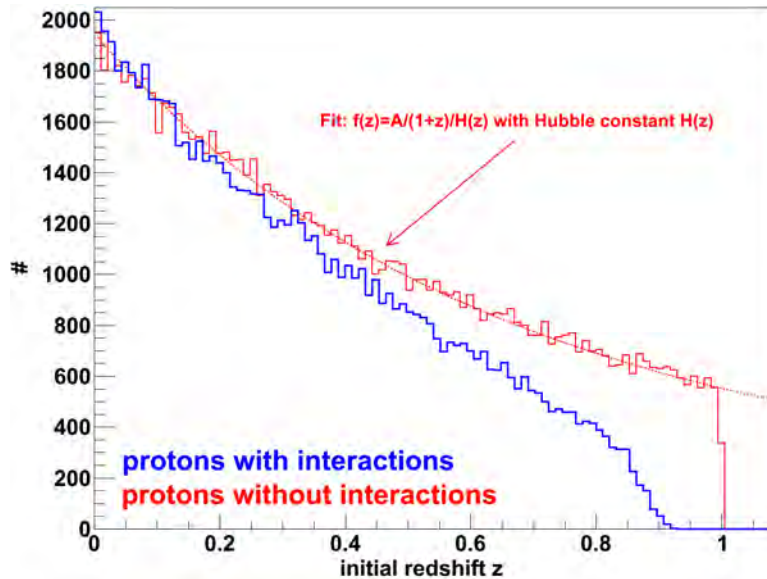


Figure 3.10.: Initial redshift distribution of protons without (red) and with (blue) interactions. If the interactions are switched off, the distribution follows equation 3.25 – as expected.

one faces the problem that TALYS provides a huge amount of reaction channels and not all of them are likely to be triggered. Hence, a channel thinning procedure was introduced. The cross sections were used to numerically calculate the mean free path λ . The convergence of this calculations has been checked and a reasonable accuracy has been confirmed. A preliminary version of CRPropa 2.0 has been released and is currently tested by some preselected users.

In a future work it would be interesting to study the effects of different settings of TALYS on the UHE-nuclei propagation. Especially, for light nuclei where only the total photo disintegration cross section is used more exclusive channels might be available and could be collected. In general, additional effort is needed to provide improved cross section predictions and measurements as an input for the presented code routines. Furthermore, it might be interesting to investigate if an averaging over the excitation levels of the nuclei is needed to model the UHE-nuclei propagation more accurately. Indeed, the de-excitation of UHE nuclei might be a source of secondary photons up to $\sim 10^{17} – 10^{18}$ eV. This process is not included in the current version of CRPropa which is focused on the case of ultra-high energies ($E > 10^{18}$ eV).

Especially, in the context of variable photon fields where the mean free path will be calculated on the fly in CRPropa, it might be useful to provide an alternative, faster integration routine of higher order.

Chapter 4

Towards a Radio and Infrared Catalog of Galaxies

A correlation study of the arrival directions of UHECR with respect to the position of radio AGN from the VC-V catalog has been presented in chapter 2. The VC-V catalog was chosen because of its correlation (99% confidence level) with UHECR as measured by the Auger collaboration [5]. It should be noted, however, that the VC-V catalog is statistically incomplete. This is reason enough to try providing an alternative catalog of extragalactic objects for correlation studies with UHECR data. Guided by the ideas which led to the correlation studies in chapter 2, here the focus is on the creation of a catalog which holds radio and infrared flux densities and redshift information of galaxies. The reader should keep in mind that the redshift is a distance estimator which is needed in many types of correlation studies. Thus, a method is needed to identify entries in a radio and in an infrared catalog which belong to the same galaxy in order to merge the available information. This can be done by identifying the galaxies in both catalogs by their celestial coordinates. But due to the high number of sources this is difficult and it is easy to end up with missidentifications. Even more challenging is the situation near the Galactic plane where Galactic objects cause a high background. Additionally, nearby radio AGN have a huge extension. Thus, lobes, jets or even finer structures might be resolved and listed separately in the catalogs. This fact makes it difficult to give the total radio flux density for an extended object, too, as an unknown number of catalog entries would need to be summed up.

Automated procedures have been tested to create a radio and infrared catalog during the preparation of this thesis: neuronal networks, multivariate analysis and matching using the sky positions. But none of these “automated” procedures led to a notably result. Hence, a simple approach is proposed: Use astrophysical constraints to reduce the number of sources to be considered for a position based identification. This can be done e.g. by demanding a minimum amount of radio luminosity, or by creating a *volume complete sample* of infrared galaxies inside a reasonable GZK-like volume. In a first step, these preselected source sets can then be used to create a *raw* version of the catalog. In a second and more tedious step this raw catalog has to be rarefied and cross checked by an experienced astronomer who can try to sort out multiple matches and combine entries that belong together. It is noteworthy that the statistical completeness of a catalog which is created in this way can probably not be quantified.

4.1. Input Catalogs

Three astronomical catalogs are a basis for what follows. The infrared information is taken from the XSCz survey. To obtain a full sky radio source list, two radio catalogs at somewhat different frequencies are available: NVSS in the northern-, SUMSS in the southern hemisphere. The main features of these catalogs are:

XSCz : 2MASS is the name of a full sky survey at $2\mu\text{m}$. The data is divided into an extended catalog (XSC) and a point source catalog (PSC). For 23171 extended sources with a magnitude larger than 11.25 in the K-band ($2.17\mu\text{m}$) the redshifts z have been measured and a sub release, the extended source catalog with redshift (XSCz), has been prepared which has not been made public yet. For this work a pre-released version of the XSCz was provided [139]. The angular resolution of the 2MASS measurements are $\sim 0.5''$. For more information on the official 2MASS data release, check the detailed online documentation at [140].

NVSS : A radio survey at 1400 MHz of the northern hemisphere ($\delta > -40^\circ$) is the NVSS catalog. The flux completeness limit is ~ 2.3 mJy and the spatial resolution is $\lesssim 1''$ for sources brighter than 15 mJy. Details can be taken from [141]

SUMSS : The complementary catalog to NVSS at the southern hemisphere ($\delta < -30^\circ$) is called SUMSS [142]. The underlying measurements are performed at a frequency of 843 MHz. In case of SUMSS the flux completeness limit is ~ 18 mJy. The measurement has a resolution of $\sim 1''\text{-}2''$ for sources with a peak brightness $A > 20\text{mJy/beam}$ but is always better than $10''$.

4.2. Calibration

The two radio catalogs SUMSS and NVSS have an *overlap region* for declination values $-40^\circ < \delta < -30^\circ$. This region can be used to calibrate the flux densities $F_{1400\text{MHz}}$ at 1400 MHz and $F_{843\text{MHz}}$ at 843 MHz: Let $N(F)$ be the number of sources in one of the radio catalogs with a flux density larger than F which are located in the overlap region. For a given radio flux density $F_{843\text{MHz}}$ there should be a corresponding value $F_{1400\text{MHz}}(F_{843\text{MHz}})$ which should roughly yield the same number of sources $N[F_{843\text{MHz}}] = N[F_{1400\text{MHz}}(F_{843\text{MHz}})]$ - if the radio flux densities are above the completeness limits of both catalogs. This fact can be exploited to yield the calibration relation; the calibration curve $F_{1400\text{MHz}}(F_{843\text{MHz}})$ is expected to be along the line where $\Delta N = |N[F_{843\text{MHz}}] - N[F_{1400\text{MHz}}(F_{843\text{MHz}})]|$ is minimal. This is visualized in figure 4.1 which shows ΔN as function of the radio threshold in both catalogs. A line fit to the minimum in ΔN gives an estimate for the calibration curve

$$\log_{10}\left(\frac{F_{1400\text{MHz}}}{[\text{mJy}]}\right) = -1.76 \cdot 10^{-1} + 1.01 \cdot \log_{10}\left(\frac{F_{843\text{MHz}}}{[\text{mJy}]}\right). \quad (4.1)$$

The fit starts at the completeness limit 18 mJy of the SUMSS catalog. It is difficult to assign an uncertainty to the minimum. Hence, the χ^2 value can not be used for a quantification of the agreement of the fit function with the data. Furthermore, one expects that resolved sources might cause $\Delta N \neq 0$ due to the different spatial resolutions at the different frequency. Note, objects inside the Galactic plane region ($|b| < 10^\circ$) have been excluded from this analysis.

The advantage of this approach is that it can be applied before an identification of the sources e.g. by using their sky positions. In general it is important to have a common flux density for SUMSS and

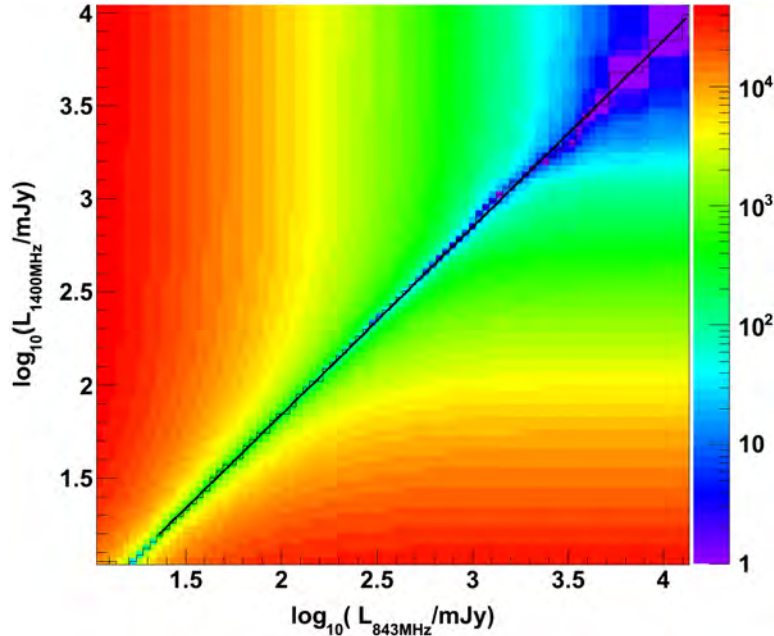


Figure 4.1.: The difference ΔN (color coded) in the number of sources above a flux threshold in the SUMSS and the NVSS catalog is shown. Only sources in the overlap region of SUMSS and NVSS ($-40^\circ < \delta < -30^\circ$) and outside the Galactic plane ($|b| > 10^\circ$) have been taken into account. A line is fitted to the minimum, see text for further explanation.

NVSS sources e.g. to perform a scan in the radio luminosity or the flux density as has been done in section 2.3.

The radio spectrum of galaxies is expected to roughly follow a power law spectrum with an index $\alpha = 0.5 - 2$ [12]. Thus, the two flux densities at different frequency can be related to each other via

$$\log_{10} \left(\frac{F_{1400\text{MHz}}}{[\text{mJy}]} \right) = -\alpha \log_{10} \left(\frac{1400\text{MHz}}{843\text{MHz}} \right) + \log_{10} \left(\frac{F_{843\text{MHz}}}{[\text{mJy}]} \right). \quad (4.2)$$

It follows that equation 4.1 corresponds to a power law with

$$\alpha \approx 0.8 \quad (4.3)$$

by comparing the first term of the fitted function with the one from equation 4.2.

4.3. Preselection

As already stated above, it is important to preselect sources in the radio and infrared catalogs in order to start the identification procedure with as few sources as possible. This reduces the possibility to find random missidentifications. Here, this is done by assuming a GZK horizon at a redshift of $z = 0.04$ which corresponds to a distance of approximately 167 Mpc. Furthermore, only objects at least as bright in radio as Centaurus A will be considered in the first step. The latter preselection criterion is somewhat arbitrarily and might be changed later on.

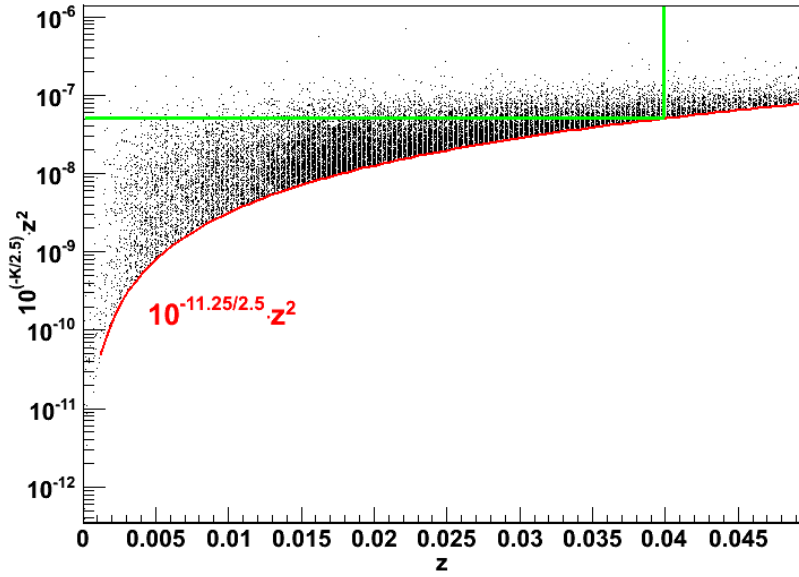


Figure 4.2.: The k magnitudes as given in the XSCz catalog are shown converted via $L_{\text{ir}} = 10^{-K/2.5} \cdot z^2$ which is proportional to the luminosity. Here, L_{ir} is shown as a function of the redshift z . Faint sources can only be seen if they are nearby. Hence, a volume complete sample of galaxies up to a redshift of $z = 0.04$ is within the green rectangle. Note, only sources which are brighter than 11.25 mag are in the XSCz catalog. This limit is indicated with the red line.

Using the redshift information and the infrared flux density F_{ir} in the K-band, one can create a volume complete sample of 2MASS galaxies. The procedure can be explained with figure 4.2 where the luminosity $L_{\text{ir}} \propto F_{\text{ir}} \cdot z^2$ is plotted versus the redshift. Strictly speaking this is only an auxiliary quantity which is proportional to the luminosity, see the corresponding remarks in chapter 2.4.2. Note in this context, that the redshift is a rough measure of the distance d and that the energy per area would fall off $\propto d^{-2}$. The red line marks the luminosity threshold for the XSCz catalog which, by construction, only holds galaxies brighter than 11.25 mag. A volume complete sample of galaxies up to a redshift of $z = 0.04$ can be created by selecting all sources inside the green rectangle.

Centaurus A has a radio flux density of $F'_{1400 \text{ MHz}} = 1330 \text{ Jy}$ [105]. Assuming an isotropic emission, this would correspond to a flux density of $F_{1400 \text{ MHz}} = F'_{1400 \text{ MHz}} \cdot (0.0009/0.04)^2 = 673 \text{ mJy}$ if Centaurus A would be located at a redshift of $z = 0.04$ instead of its true redshift $z = 0.0009$. This can be converted into the corresponding value of $L_{843 \text{ MHz}} = 942 \text{ mJy}$ at 843 MHz. Thus, in what follows NVSS sources which are brighter than $L_{1400 \text{ MHz}} > 673 \text{ mJy}$ and SUMSS sources with $L_{843 \text{ MHz}} > 942 \text{ mJy}$ are considered.

After this preselection one has to consider 3045 NVSS, 998 SUMSS and 3072 2MASS objects for the creation of the radio and infrared catalog.

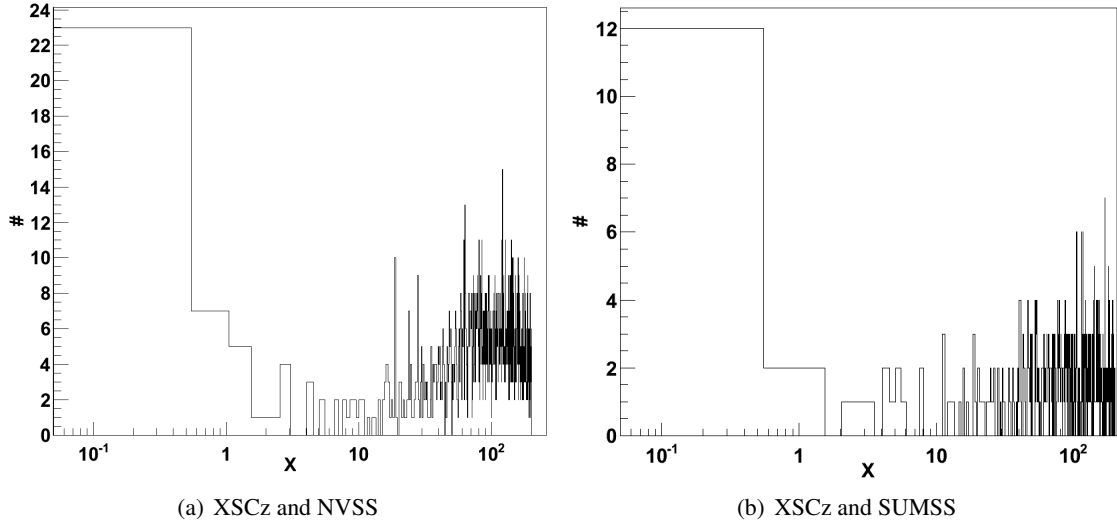


Figure 4.3.: Distribution of the angular distance parameter X (s. equation 4.4) for a cross correlation of XSCz and NVSS sources (a) and XSCz and SUMSS sources (b).

4.4. The Raw Catalog

Now one can try to identify the radio sources (NVSS+SUMSS) with their corresponding infrared source (XSCz) using their sky position and the radio extensions. To do so the quantity

$$X = \frac{\Omega}{\sqrt{\sigma_{ir}^2 + \sigma_r^2 + e_{ir}^2 + e_r^2}} \quad (4.4)$$

was used where Ω is the angular distance between the radio and the infrared position, σ_{ir} and σ_r are the resolutions of the infrared and radio measurements and e_{ir} , e_r are the major axes of the sources. Here, the major axes are identified with the source size. As the XSCz catalog does not provide extension values, the e_{ir} are neglected. The distribution of X values calculated for both radio catalogs with respect to the XSCz is shown in figure 4.3.

A *raw* version of the catalog has been created using $X < X_{cut} := 5$. Then one can start to compare if known radio and infrared galaxies are in the sample. If there are missing ones - or too much random identifications -, one can start to fine tune the X_{cut} value. A simple cross check has shown that all sources that are in the well known Kuehr catalog [143] have a counterpart in the *raw* catalog [144]. This suggest that the identification window $X_{cut} = 5$ is reasonably large. Note, that during the creation of the raw catalog, 19 XSCz sources had more than 1 match with the NVSS catalog. In the case of SUMSS the corresponding number was found to be 10.

Now the astronomical part of the work has to start. Each potential source from the *raw* catalog has to be looked at and double- as well as missidentifications have to be sorted out. Furthermore, a literature study has to be started to check whether all prominent and already known source are included. This extensive work will be done in cooperation with Sjoert van Velzen from the University of Nijmegen in the Netherlands. The final catalog will be published once this work will be finished.

An Aitoff projected skymap which shows all 56 radio and infrared sources which are in the radio and infrared *raw* catalog is given in figure 4.4. For this skymap the equatorial coordinates from the

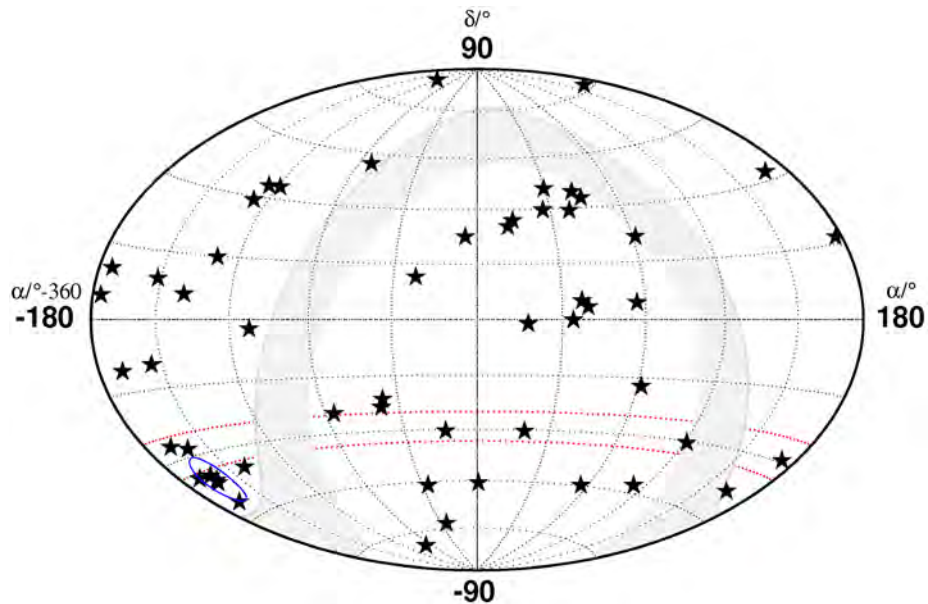


Figure 4.4.: Aitoff projected sky map of the created *raw* radio and infrared catalog. The infrared positions of the galaxies are marked with a star. The x -axis shows the right ascension α for $\alpha < 180^\circ$ and $\alpha - 360^\circ$ otherwise. The Galactic plane region is given in grey. No entries in this region, do exist because they were excluded from this analysis. The overlap region of the two radio catalogs SUMSS and NVSS is framed with red lines. In this region the identifications with the NVSS catalogs were chosen. The location of Centaurus A is encircled in blue.

infrared catalog XSCz are displayed. In case of multiple matches, the radio source with the closest distance to the infrared source was selected. In the overlap region the NVSS catalog was chosen.

A simple cross check of the reliability of the identification procedure can be done using the overlap region of NVSS and SUMSS. As the radio flux densities limits applied for the preselection are above the completeness limits of both catalogs, one expects to find the same identifications with the XSCz sources in the overlap region. The situation is displayed in figure 4.5 where the positions of the NVSS and SUMSS sources from the *raw* catalog are plotted on top of each other. One can see that there is one SUMSS source without a match in the NVSS. It is in the region of the extended Fornax A radio galaxy - a galaxy which is resolved in much detail on the radio pictures. As expected, this complicates the identification. This cross check suggest that technical aspects of the identification procedure works reliably but underlines the aforementioned difficulties caused by the huge extensions of nearby, resolved radio galaxies.

Summary and Conclusion

A first step towards the creation of a full sky radio and infrared catalog of galaxies for UHECR astronomy has been made. That is, a *raw* catalog has been created using the angular distance of the radio and infrared sources with respect to the radio extensions and the mean position uncertainties of the underlying measurements. This procedure was applied to a preselected, small set of sources. This preselection, which is motivated by astrophysical considerations, reduces the probability of random-

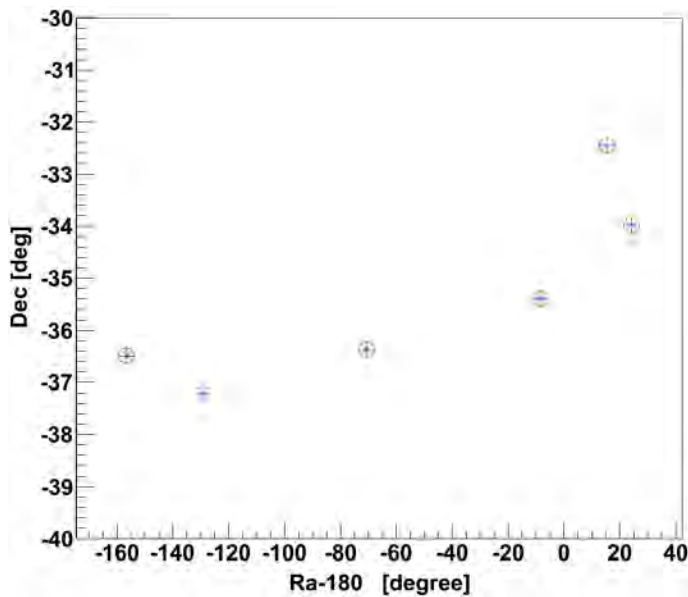


Figure 4.5.: The positions of the *raw* catalog entries for NVSS (blue stars) and SUMSS (red circles) plotted on top of each other. Only the overlap region $-40^\circ < \delta < -30^\circ$ of the two radio catalogs is considered. Herein, sources in the Galactic plane region have been excluded.

and missidentifications. In a second step, each entry in the *raw* catalog has to be manually cross checked based on all available astronomical information.

Overview of Scientific Results

Before finally closing this thesis, a short summary of the scientific results will be given which were presented in the chapters 2 to 4.

- A four dimensional scan technique is introduced which aims on finding anisotropies in the UHECR arrival directions with respect to VC-V AGN with a given radio flux densities F_{6cm} at 6cm wavelength. This analysis counts the number of correlations inside top hats around the AGN and uses binomial statistics to minimize the probability for the UHECR data to arise from an isotropic distribution. This minimization is performed as function of four scan parameters: the UHECR energy threshold E_{th} , the radius Ψ of the top hats as well as the maximum distance z_{max} and minimum logarithmic radio luminosity $\log_{10}(L) \propto \log_{10}(F_{\text{6cm}} \cdot z^2 / \text{Jy})$ of the AGN. Using the PAO surface detector data up to March, 2nd 2008, the observed minimum parameters are: $E_{\text{th}} = 51.92 \text{ EeV}$, $\psi = 5.9^\circ$, $z_{\text{max}} = 0.018$ and $\log(F_{\text{6cm}} \cdot z^2 / \text{Jy}) = -5.36$ (\Leftrightarrow luminosity $L = 9 \cdot 10^{21} \text{ W Hz}^{-1}$). Within these minimum parameters there are 17 correlations out of 31 events with the 56 AGN above the radio threshold while four correlations would have been expected in case of isotropy. The penalized or post trials probability for this to happen is $P_{\text{pen}} = 0.3\%$.

These energy and redshift minimum parameters are similar to what has been reported by the Pierre Auger collaboration using a similar analysis but only scanning in three dimensions (E_{th} , z_{max} , Ψ). Furthermore, this analysis was based on a larger set of AGN if compared to this thesis. That is because no measured radio flux densities were needed. Due to this comparison, the question arises if the radio AGN as preselected by the four dimensional scan results are possible UHECR sources, or if the correlation signal in question is just traced by a similar mass distribution they share with all VC-V AGN or the mass distribution in our nearby Universe in general. Thus, it is suggested to perform correlation studies but with randomly shuffled radio luminosities among the radio VC-V AGN. Doing so, an indication is found that the radio information of the AGN can be used to strengthen the correlation with the UHECR arrival directions. If true, this would imply that radio AGN are likely sources of - at least some - UHECR.

A hypothesis test (aiming for 99% confidence) was set up to test the anisotropy of UHECR arrival directions with respect to the radio VC-V AGN as prescribed by the previously mentioned minimum parameters. For this test, an independent, growing data set starting on March, 3rd 2008 up to July, 4th 2010 is available. Currently, this test has not reached a decision and more data has to be collected.

If one wants to set up an official prescription, a two folded approach is proposed: Firstly, use the aforementioned hypothesis test to reject isotropy. Secondly, test if an intrinsic property of the

AGN can be used to significantly improve the correlation with the UHECR data e.g. by applying the flux shuffling type of experiments. Indeed, the second step might make the difference between showing UHECR anisotropy and identifying their sources.

Some models of UHECR acceleration in radio loud AGN do predict a higher radio luminosity threshold than what has been found in the presented four dimensional scan. Indeed, active jets and huge radio structures (jets, lobes ~ 100 kpc) are often considered to be the origin of the UHECR. This special radio morphology can be found in huge radio galaxies e.g. of the FR I/II type. Many AGN which are selected by the four dimensional scan do not meet these requirements. If those AGN at least have jet activity on smaller scales or if the radio signal is linked with star burst activity, might be separated by using the radio to infrared ratio $R_{\text{FIR}}^{\text{6cm}}$. Here, an indication has been found that AGN with an enhanced radio to infrared ratio $1 < R_{\text{FIR}}^{\text{6cm}} < 2$ strengthen the correlation with the UHECR data. This approach could be extended into a five dimensional scan procedure.

- To predict the behavior of measurable quantities on Earth, it is essential in order to test models of UHECR acceleration. These predictions can then be compared with observations to statistically quantify the agreement of a model with UHECR data. The needed modeling should include the creation and propagation of UHECR as well as their detection. A tool to study the propagation of UHE-nucleons is the publicly available CRPropa framework. As the elongation rate data from the PAO indicate that some UHECR might be nuclei, an extension of version 1.3 of CRPropa to allow for the propagation of nuclei is in order. Herein, a major challenge is the modeling of the photodisintegration reactions which is linked with a large multitude of possible reaction channels. In this thesis, a compilation of 78449 photo nuclear reaction channels for nuclei up to iron is presented as well as the approach to include the photo disintegration in the existing CRPropa routines. A reasonable convergence of the needed numerical calculations for a broad energy range for all these reactions channels is shown. Furthermore, a method is introduced that selects only the most important out of the 78449 reaction channels to allow for a fast and efficient simulation.

A pre-release of version 2.0 of CRPropa has been published and is currently tested by external users.

- The radio and infrared fluxes of galaxies as well as their redshifts are important in various types of correlation studies of UHECR arrival directions. Here, a first step towards a full sky radio and infrared catalog of galaxies has been made. The needed information has been collected from the complementary radio catalogs NVSS (northern hemisphere) and SUMSS (southern hemisphere). The infrared fluxes as well as the redshift have been extracted from a pre-released version of the 2MASS XSCz galaxy sample. Those entries in the radio and infrared catalogs which belong to the same galaxy have been identified using the angular distance with respect to the resolution of the underlying experiments as well as the extensions of the radio sources. Beforehand, the sources had been preselected based on astrophysical considerations e.g. to be closer than 167 Mpc. The latter is motivated by expectation that the Universe should become opaque for UHECR at the highest energies due to propagation effects (for example GZK reactions). Furthermore, for a start, only sources which are at least as bright in radio wavelength as Centaurus A are considered. This preselection of the sources reduces the chance probability to find random matches while identifying the counterparts of one galaxy in the radio and infrared catalogs. A *raw* catalog was created which is currently revisited by an astronomer who is familiar especially with large, nearby radio loud galaxies.

What is the difference between music and physics?

Well, each song defines a small, elusive universe on its own - only partially accessible to logic and mainly ruled by unutterable inspiration. Physics, instead, is the haunted attempt to grasp the unnameable beauty and precision of the Universe we inhabit.

So, who knows? Maybe we are just a part of one of God's compositions woven by the voices of angels in the heavens?

Acknowledgments

First of all, I want to express my gratitude to Karl-Heinz Kampert who gave me the opportunity to compose this work. Surely, it will remain a mystery to me how he always has managed to find time for giving advice or having a physics discussion next to his enormous work load. And, no matter what, he always remained calm - which is indeed impressive considering that ambitious young minds occasionally come close to be hot-headed. From what I was allowed to observe around him, it is surely true that authority naturally comes along with calmness, circumspection and well-founded decisions. I am further grateful to him for the allocation of travel funding which allowed me to meet, visit and cooperate with colleagues from other towns and countries. Next to the scientific exploit, these experiences shaped my way of being and thinking.

Among many others, these are reasons why I am happy and proud to call Karl Heinz Kampert *meinen Doktorvater*¹ which suits his role better than the pale phrase supervisor.

I feel indebted to Markus Risse who taught me how much care and attention has to be summoned while trying to convert observational data into physics results. He influenced me to work even more accurate efficient and goal orientated. Markus Risse also had a strong impact on my attitude during discussions to become more calm and less emotional. Next to that, his way of presenting results in public is simply inspiring.

Indeed, he did not accomplish all these things by actively giving verbal advice. Sometimes already observing a well educated mind at work is worth a lesson.

With great pleasure I look back on a collaboration with my colleagues from the University of Hamburg. Especially, Guenter Sigl's experience guided us well towards the completion of the CRPRopa

¹German term, literally: my PhD father.

extensions. He surely is one of the main reasons for a growing tendency to theoretical physics in my work and personal interest. An outstanding big thank you goes to Jörg Konrad Kulbartz for a productive, close cooperation and discussions about the common goal: propagation of nuclei with CRPropa. Thank you “Hamburg”, you surely define my personal standard in teamwork so far.

I benefited a lot from a stay and several discussions about astronomy with scientist from the University of Nijmegen: Heino Falcke, Jörg Hörandel, Sarka Jiraskova and Sjoert van Velzen. Most importantly, Heino Falcke was an inspiration for many astronomical considerations which are embedded into this thesis.

It was a great personal experience to be a part of the Pierre Auger Collaboration. And I highly appreciate the possibility to have met so many great minds and people from different countries. Some of them have to be explicitly named to express my gratitude for discussions and scientific exchange: Segev BenZvi, Peter Schiffer, Michael Unger, Simone Riggi, Peter Biermann, Martin Erdmann, Fabian Schüssler, Diego Harari, Esteban Roulet, Dimitri Semikoz, Antoine Letessier-Selvon, Carla Bonifazi and Stefan Westerhoff.

Thank you to all the Auger Youngsters and my FD-shift partners - especially, Adrian Schmidt and Marco Haag for being such good “shift-mates” and a great company during my stays in Malargüe and Mendoza. These visits to Argentina were always a pleasure also due to the friendly and helpful people and the staff on the site, most notably Rosa Ines Pacheco and Julio Rodriguez Martino.

I gratefully acknowledge discussions about all facets of physics and object orientated programming with Timo Karg from the astroparticle physics department in Wuppertal. He really impressed me with his quick perception and an immanent easiness in grasping thoughts, ideas and the essence of the work of other people.

Thank you very much to my colleagues from the physics department of the University of Wuppertal for great support, enjoyable company as well as a warm and refreshing atmosphere. This in particular applies, to my office mates and Frau Schaarwächter who helped me to face one of my worst enemies: organizational paperwork ;-). Thanks to Julian Rautenberg, Karl-Heinz Becker and, again, Timo Karg who did a great job in maintaining the group’s computer cluster which was essential while preparing this thesis.

Out of friendship and for academic reasons above the scope of this thesis, an individual paragraph is in order for Julia Becker while crossing from professional to private statements of gratitude in my acknowledgments.

A sources of strength, support and affection are my family and close friends which comprise the central point of my being, thank you to my parents, my sisters and the rest of my family, Björn, Iris, Kai, Lars and Pietro. And especially Elmar Neugebauer, my oldest friend, who has designed the cover which enclose this thesis. A big hug to my friends and (former) roommates: Charly, Christian, Nicole and the other “ZooRoomies”.

*To emphasize their importance,
I want to end with a dedication to my beloved parents
who always encouraged me to explore my sometimes rapidly changing interests.*

Statutory Declaration

I declare that I have authored this thesis independently, that I have not used other than the declared sources / resources, and that I have explicitly marked all material which has been quoted either literally or by content from the used sources.

Wuppertal,

Place, Date

Signature

Eidesstattliche Erklärung

Ich erkläre an Eides statt, dass ich die vorliegende Arbeit selbstständig verfasst, andere als die angegebenen Quellen/Hilfsmittel nicht benutzt, und die den benutzten Quellen wörtlich und inhaltlich entnommene Stellen als solche kenntlich gemacht habe.

Wuppertal, am

Ort, Datum

Unterschrift

VC-V AGN List

A set of 355 VC-V AGN was selected which have a listed radio flux density at a wavelength of 6 cm and redshifts $z \leq 0.04$ [4]. They enter the analysis work described in chapter 2. An exception to this is the three dimensional scan of section 2.2 which is based on 694 VC-V AGN up to $z \leq 0.024$ but without requiring an available radio flux density $F_{6\text{cm}}$. In section 2.11 the infrared flux densities at a wavelength of 60 microns were needed, too. These values are not distributed with the VC-V catalog data. Thus, they have been collected using the NED database [115] in January, 2011. Further details can be found in section 2.4.1.

Table A.1.: List of VC-V AGN with a given radio flux at a wavelength of 6 cm and redshifts smaller than $z \leq 0.04$, cf. section 2.4.1. The first two columns hold the name and the classification of the galaxies. For an explanation of the used abbreviations see [4]. Column three to five hold the two equatorial coordinates and the galactic latitude. It follows a column with the redshift. At last, the flux densities at 6 cm and $60\mu\text{m}$ are listed. These values were collected using the Nasa Extragalactic Database. If no value was available, -1 is given.

Three separated tables for BL Lac objects, Quasars and AGN comprise to the full VC-V catalog. In this thesis, AGN collected from all of these tables are considered. Thus, the first nine entries belong to the BL Lac, the following ten entries to the Quasars table. The remaining 336 rows have been extracted from the AGN table of the VC-V catalog.

name	type	Ra/ $^{\circ}$	Dec/ $^{\circ}$	b/ $^{\circ}$	z	$F_{6\text{cm}}/\text{Jy/Hz}$	$F_{60\mu\text{m}}/\text{Jy/Hz}$
8C 0149+710	No	28.36	71.25	8.98	0.022	0.643	-1
V Zw 331	BL	48.49	41.26	-14.07	0.029	0.048	-1
RXS J05055+0416	BL	76.39	4.27	-21.20	0.027	0.112	-1
TEX 0554+534	BL	89.55	53.47	14.15	0.036	0.234	-1
1WGA J0816.0-0736	BL	124.02	-7.60	14.96	0.04	0.061	-1
MARK 421	HP	166.11	38.21	65.03	0.031	0.4	0.181
NGC 5128	?	201.37	-43.02	19.42	0.00083	579	162.2
MARK 501	HP	253.47	39.76	38.86	0.033	1.118	0.117
RXS J21231-1036	BL?	320.78	-10.61	-38.43	0.023	0.17	-1
M 31	S2	10.68	41.27	-21.57	0.00019	2.46	10.79
NGC 3031	S3b	148.89	69.07	40.90	0.000884	0.093	6.806
3C 278	S3	193.65	-12.56	50.30	0.016	2.54	-1
IRAS 13120-5453	S2	198.78	-55.16	7.56	0.031	0.154	41.49

continued on next page

Appendix A. VC-V AGN List

Table A.1 – continued from previous page

name	type	Ra/$^{\circ}$	Dec/$^{\circ}$	b/$^{\circ}$	z	$F_{6cm}/\text{Jy/Hz}$	$F_{60\mu\text{m}}/\text{Jy/Hz}$
MARK 266NE	S3	204.57	48.28	66.97	0.028	0.049	-1
Circinus	S1h	213.29	-65.34	-3.81	0.001	0.695	248.7
MARK 509	S1.5	311.04	-10.72	-29.86	0.035	0.005	1.364
1ES 2055+298	S1	314.51	30.05	-10.13	0.036	0.002	-1
IRAS 21497-0824	S2	328.11	-8.17	-43.67	0.034	0.065	3.124
3C 465.0	S1	354.62	27.03	-33.07	0.03	2.8	0.17
Zw 517.014	S2	0.49	36.65	-25.17	0.032	0.027	4.476
MARK 334	S1.8	0.79	21.96	-39.54	0.022	0.011	4.345
MARK 335	S1n	1.58	20.20	-41.42	0.026	0.003	0.3433
MARK 938	S2	2.78	-12.11	-72.25	0.019	0.026	16.62
IRAS 00160-0719	S2	4.65	-7.05	-68.46	0.018	0.001	1.641
ESO 350-IG38	H2	9.22	-33.56	-82.85	0.02	0.007	6.476
MARK 1143	H2	10.64	3.26	-59.54	0.037	0.016	0.4905
MARK 1144	H2	10.66	3.24	-59.56	0.037	0.013	-1
NGC 253	S	11.89	-25.29	-87.96	0.001	2.433	784.2
MARK 348	S1h	12.20	31.96	-30.91	0.014	0.462	1.29
NGC 266	S3b	12.45	32.28	-30.59	0.015	0.004	0.8141
UGC 524	S1.0	12.90	29.40	-33.47	0.036	0.003	0.9435
NGC 315	S3h	14.45	30.35	-32.50	0.016	0.914	0.2703
PKS 0056-572	S1	14.69	-56.99	-60.11	0.018	0.813	-1
NGC 424	S1h	17.87	-38.08	-78.27	0.011	0.015	1.796
MARK 1	S2	19.03	33.09	-29.50	0.016	0.032	2.531
MARK 567	H2	19.83	4.58	-57.59	0.033	0.017	3.027
NGC 526A	S1.9	20.98	-35.07	-79.46	0.019	0.004	-1
NGC 513	S1h	21.11	33.80	-28.57	0.019	0.022	1.935
MARK 991	No	21.19	32.17	-30.18	0.036	0.028	1.261
MARK 993	S1.5	21.38	32.14	-30.18	0.017	0.002	0.2958
PKS 0131-522	S1	23.27	-52.00	-63.92	0.02	0.693	-1
MARK 1157	S1h	23.38	35.67	-26.42	0.015	0.008	1.991
NGC 613	S?	23.58	-29.42	-80.29	0.005	0.081	22.01
NGC 660	S3	25.76	13.64	-47.35	0.003	0.156	65.54
MARK 573	S1h	25.99	2.35	-57.92	0.017	0.006	1.088
III Zw 35	S2	26.13	17.10	-43.93	0.027	0.025	12.55
IRAS 01475-0740	S1h	27.51	-7.43	-65.89	0.017	0.297	1.048
UGC 1395	S1.9	28.84	6.61	-52.88	0.017	0.01	0.4673
NGC 777	S2	30.06	31.43	-29.19	0.017	0.003	-1
NGC 788	S1h	30.28	-6.82	-63.80	0.013	0.001	0.5105
MARK 590	S1.0	33.64	-0.77	-56.94	0.027	0.004	0.4893
3C 66.0B	S1	35.80	42.99	-16.77	0.021	3.75	-1
AKN 81	S?	35.84	32.20	-26.77	0.035	0.022	6.475
Zw 523.037	S	36.36	37.17	-22.01	0.033	0.137	-1
MARK 1040	S1.0	37.06	31.31	-27.17	0.016	0.003	2.555
MARK 1179	S1.9	38.34	27.94	-29.75	0.038	0.006	-1
NGC 1052	S3h	40.27	-8.26	-57.93	0.005	0.88	0.9027
NGC 1068	S1h	40.67	-0.01	-51.93	0.003	1.9	176.2
MARK 596	S2	40.72	7.60	-46.03	0.039	0.042	0.7864
NGC 1097	S3b	41.58	-30.27	-64.68	0.004	0.15	44.54
NGC 1144	S2	43.80	-0.18	-49.89	0.029	0.049	5.302
MARK 1066	S2	44.99	36.82	-19.27	0.012	0.035	10.98
NGC 1167	S3	45.43	35.21	-20.49	0.016	0.912	0.12

continued on next page

Table A.1 – continued from previous page

name	type	Ra/$^{\circ}$	Dec/$^{\circ}$	b/$^{\circ}$	z	$F_{6cm}/\text{Jy/Hz}$	$F_{60\mu\text{m}}/\text{Jy/Hz}$
NGC 1218	S1	47.11	4.11	-44.51	0.029	3.554	-1
NGC 1241	S2	47.81	-8.92	-52.31	0.013	0.067	-1
MARK 1073	S2	48.76	42.04	-13.31	0.023	0.044	8.166
NGC 1275	S1.5	49.95	41.51	-13.26	0.017	18.72	7.146
MARK 607	S2	51.20	-3.04	-46.16	0.009	0.004	2.152
MARK 609	S1.8	51.36	-6.14	-47.85	0.032	0.005	2.578
PKS 0325+02	S3	51.98	2.56	-42.02	0.03	1.594	0.18
NGC 1365	S1.8	53.40	-36.14	-54.60	0.006	0.21	76.13
NGC 1386	S1i	54.19	-36.00	-53.97	0.002	0.013	5.396
ESO 548-G81	S1	55.52	-21.24	-50.83	0.015	0.001	0.6014
IRAS 03450+0055	S1.5	56.92	1.09	-39.11	0.031	0.012	0.4707
3C 98.0	S2	59.73	10.43	-31.05	0.031	4.97	-1
MS 04124-0802	S1.5	63.72	-7.93	-38.26	0.037	0.002	0.6335
NGC 1566	S1.5	65.00	-54.94	-43.39	0.004	0.076	14.71
ESO 202-G23	S3	67.00	-47.91	-43.46	0.016	0.055	1.869
NPM1G-04.0195	S3	67.11	-4.56	-33.68	0.016	0.002	4.129
3C 120	S1.5	68.30	5.35	-27.40	0.033	5.09	1.283
NGC 1614	H2	68.50	-8.58	-34.38	0.015	0.063	32.31
MARK 618	S1.0	69.09	-10.38	-34.66	0.035	0.004	2.706
NPM1G-08.0177	S1h	70.23	-8.37	-32.76	0.015	0.012	2.774
NGC 1672	S	71.43	-59.25	-38.99	0.004	0.1	32.96
NGC 1667	S2	72.16	-6.32	-30.12	0.015	0.045	5.952
UGC 3179	H2	72.44	3.33	-25.05	0.028	0.014	-1
NGC 1685	S1.9	73.14	-2.95	-27.65	0.014	0.005	0.9757
IRAS 04502-0317	S2	73.18	-3.22	-27.74	0.016	0.001	0.8341
NGC 1692	S3	73.85	-20.57	-34.36	0.035	1.78	0.681
MS 04595+0327	S1	75.54	3.53	-22.31	0.016	0.005	-1
NGC 1808	H2	76.93	-37.51	-35.90	0.003	0.213	87.81
AKN 120	S1.0	79.05	-0.15	-21.13	0.033	0.003	0.643
PKS 0518-45	S3b	79.96	-45.78	-34.63	0.034	15	0.163
NGC 1961	S3	85.52	69.38	19.47	0.012	0.06	6.382
UGC 3351	S2	86.45	58.70	15.01	0.015	0.047	14.45
NGC 2110	S1i	88.05	-7.46	-16.55	0.007	0.175	4.129
H 0557-385	S1.2	89.51	-38.33	-26.36	0.034	0.02	0.322
MARK 3	S1h	93.90	71.04	22.72	0.014	0.353	3.77
Zw 308.017	S	94.18	66.51	21.38	0.014	0.174	-1
MARK 620	S1h	102.54	60.85	23.31	0.006	0.008	6.021
MARK 6	S1.5	103.05	74.43	26.11	0.019	0.115	1.183
ESO 428-G14	S2	109.13	-29.32	-7.97	0.005	0.07	4.401
MARK 9	S1.5	114.24	58.77	28.75	0.039	0.001	0.7676
MARK 79	S1.2	115.64	49.81	28.38	0.022	0.004	1.503
MARK 78	S2	115.67	65.18	29.78	0.038	0.009	1.11
MARK 1210	S1h	121.02	5.11	18.48	0.013	0.056	1.892
MARK 1218	S1.8	129.55	24.90	33.68	0.028	0.015	0.4283
NGC 2639	S3	130.91	50.21	38.19	0.011	0.04	1.988
NGC 2655	S3	133.91	78.22	32.69	0.005	0.043	1.673
MARK 703	H2	134.71	6.29	31.12	0.013	0.015	3.669
NGC 2768	S	137.91	60.04	40.56	0.005	0.01	0.3694
NGC 2782	S2	138.52	40.11	43.68	0.008	0.049	8.668
NGC 2787	S3b	139.83	69.20	38.05	0.003	0.009	0.6437

continued on next page

Appendix A. VC-V AGN List

Table A.1 – continued from previous page

name	type	Ra/$^{\circ}$	Dec/$^{\circ}$	b/$^{\circ}$	z	$F_{6cm}/\text{Jy/Hz}$	$F_{60\mu\text{m}}/\text{Jy/Hz}$
NGC 2841	S3	140.51	50.98	44.15	0.002	0.03	3.034
MARK 110	S1n	141.30	52.29	44.36	0.035	0.002	-1
MARK 705	S1.2	141.51	12.73	40.00	0.028	0.01	0.5901
NGC 2911	S3	143.44	10.15	40.56	0.01	0.19	0.2192
UGC 5101	S1	143.97	61.35	42.90	0.04	0.079	11.54
MARK 1419	S3	145.15	3.58	38.77	0.015	0.011	0.708
MARK 403	S2	145.19	21.23	46.36	0.024	0.014	-1
NGC 2965	S?	145.83	36.25	49.36	0.022	0.081	-1
NGC 2992	S1i	146.43	-14.33	28.78	0.008	0.077	7.51
ESO 434-G40	S1i	146.92	-30.95	17.23	0.008	0.006	-1
NGC 2985	S1.9	147.59	72.28	38.68	0.004	0.02	5.004
NGC 3032	H2	148.03	29.24	50.67	0.005	0.004	1.782
MARK 1239	S1n	148.08	-1.61	38.22	0.019	0.019	1.335
NGC 3081	S1h	149.87	-22.83	25.03	0.007	0.001	-1
NGC 3079	S2	150.49	55.68	48.36	0.004	0.327	44.5
IRAS 10057-3343	S	152.00	-33.97	17.66	0.034	0.007	2.615
NGC 3169	S	153.56	3.47	45.65	0.003	0.023	6.508
NGC 3147	S2	154.22	73.40	39.46	0.01	0.047	7.261
NGC 3185	S2	154.41	21.69	54.70	0.004	0.002	1.427
IRAS 10201-3601	H2	155.60	-36.28	17.53	0.034	0.004	1.406
NGC 3226	S3b	155.86	19.90	55.44	0.004	0.004	-1
NGC 3227	S1.5	155.88	19.87	55.45	0.003	0.046	7.825
ESO 500-G34	S2	156.13	-23.55	28.14	0.013	0.023	11.25
ESO 436-G26	H2	157.18	-31.04	22.60	0.014	0.005	2.299
NGC 3281	S2	157.97	-34.85	19.78	0.011	0.027	6.861
NGC 3310	H2	159.69	53.50	54.06	0.003	0.152	30.53
MARK 1261	H2	160.97	-1.29	48.17	0.026	0.004	-1
NGC 3362	S2	161.22	6.60	53.61	0.028	0.004	-1
NGC 3367	S	161.65	13.75	57.96	0.01	0.036	6.005
NGC 3393	S2	162.10	-25.16	29.89	0.012	0.052	2.251
MS 10473+3518	S1.9	162.54	35.03	62.98	0.04	0.003	0.7135
MARK 728	S1.9	165.26	11.05	59.48	0.036	0.036	-1
MS 10588+1003	S1.9	165.36	9.79	58.81	0.028	0.006	-1
UGC 6100	S2	165.39	45.65	61.41	0.029	0.004	0.5743
NGC 3504	H2	165.80	27.97	66.04	0.005	0.117	21.2
NGC 3516	S1.5	166.70	72.57	42.40	0.009	0.015	1.758
ESO 438-G09	S1	167.70	-28.50	29.36	0.024	0.007	3.144
NGC 3561B	S3	167.80	28.70	67.84	0.028	0.062	4.18
MS 11103+2210	S1	168.25	21.91	67.05	0.03	0.001	-1
MARK 732	S1.5	168.46	9.59	61.06	0.03	0.019	1.75
ESO 319-G12	S2	169.76	-40.01	19.50	0.036	0.004	2.006
NGC 3627	S3	170.06	12.99	64.42	0.002	0.141	41.67
NGC 3660	S1.8	170.88	-8.66	48.35	0.011	0.011	1.872
IRAS 11215-2806	S2	171.01	-28.39	30.66	0.014	0.02	0.566
MARK 423	S1.8	171.70	35.25	70.22	0.032	0.01	1.423
ESO 439-G09	S2	171.85	-29.26	30.13	0.023	0.022	0.6471
MARK 171	H2	172.13	58.56	55.41	0.01	0.407	103.7
MARK 176	S1i	173.17	52.95	60.32	0.027	0.01	0.6937
NGC 3738	H2	173.95	54.53	59.31	0.001	0.037	2.003
NGC 3735	S2	173.99	70.54	45.28	0.009	0.028	6.697

continued on next page

Table A.1 – continued from previous page

name	type	Ra/$^{\circ}$	Dec/$^{\circ}$	b/$^{\circ}$	z	$F_{6cm}/\text{Jy/Hz}$	$F_{60\mu\text{m}}/\text{Jy/Hz}$
MARK 739E	S1n	174.12	21.60	72.08	0.03	0.001	-1
NGC 3783	S1.5	174.76	-37.74	22.95	0.009	0.016	3.257
MARK 744	S1.8	174.93	31.91	73.70	0.01	0.003	-1
ESO 504-G13	S	175.84	-27.60	32.88	0.033	0.01	2.66
NGC 3862	No	176.27	19.61	73.04	0.021	2	0.21
NGC 3894	S	177.21	59.42	55.95	0.011	0.566	0.14
IRAS 11463-3304	S	177.23	-33.34	27.73	0.028	0.004	-1
MARK 1308	H2	178.55	0.14	59.71	0.004	0.001	1.04
NGC 3982	S1.9	179.12	55.13	60.27	0.003	0.002	6.567
NGC 3994	S3	179.40	32.28	77.24	0.01	0.035	4.98
NGC 3998	S3b	179.48	55.45	60.06	0.004	0.085	0.4385
MARK 1310	S1.0	180.31	-3.68	56.90	0.019	0.001	-1
NGC 4036	S3b	180.36	61.90	54.25	0.005	0.003	0.5007
NGC 4051	S1n	180.79	44.53	70.09	0.002	0.031	7.131
IRAS 12031-3216	S2	181.43	-32.55	29.34	0.039	0.009	2.892
NGC 4102	S3	181.60	52.71	63.07	0.003	0.07	46.93
NGC 4151	S1.5	182.64	39.41	75.06	0.003	0.152	6.46
MARK 759	H2	182.66	16.03	75.42	0.007	0.073	4.116
NGC 4168	S1.9	183.07	13.21	73.34	0.008	0.005	-1
NGC 4192	S3	183.45	14.90	74.96	0.004	0.039	5.924
MARK 201	H2	183.54	54.53	61.76	0.008	0.039	21.38
NGC 4203	S3b	183.77	33.20	80.08	0.004	0.009	0.5998
ESO 505-IG30	S2	184.24	-26.21	36.02	0.04	0.003	-1
NGC 4235	S1.2	184.29	7.19	68.47	0.007	0.005	0.3164
MARK 766	S1n	184.61	29.81	82.27	0.013	0.006	4.026
NGC 4258	S2	184.74	47.30	68.84	0.002	0.17	21.6
NGC 4261	S3h	184.85	5.82	67.37	0.007	4	0.08
NGC 4278	S3b	185.03	29.28	82.77	0.002	0.48	0.5568
NGC 4303	S2	185.48	4.47	66.28	0.005	0.157	23.64
NGC 4374	S2	186.27	12.89	74.48	0.003	3.168	0.5023
NGC 4383	H2	186.36	16.47	77.76	0.005	0.016	7.945
MARK 52	H2	186.43	0.57	62.74	0.007	0.004	4.726
NGC 4388	S1h	186.44	12.66	74.33	0.008	0.093	10.24
NGC 4395	S1.8	186.45	33.55	81.53	0.001	0.001	2.375
MARK 1325	S3	186.62	9.02	70.96	0.025	0.13	0.322
NGC 4438	S3b	186.94	13.01	74.83	0.004	0.065	3.761
NGC 4450	S3b	187.12	17.08	78.64	0.006	0.007	1.343
Zw 244.025	S?	187.55	47.01	69.69	0.039	0.073	-1
NGC 4486	S3	187.71	12.39	74.49	0.004	71.9	0.3939
NGC 4501	S2	188.00	14.42	76.51	0.007	0.089	13.71
NGC 4507	S1h	188.90	-39.91	22.86	0.012	0.022	4.31
NGC 4552	S2	188.92	12.56	74.97	0.001	0.064	-1
NGC 4565	S1.9	189.09	25.99	86.44	0.004	0.003	6.65
NGC 4569	S	189.21	13.16	75.62	0.004	0.031	7.562
NGC 4579	S3b	189.43	11.82	74.36	0.005	0.056	4.742
NGC 4593	S1.0	189.91	-5.34	57.40	0.009	0.002	3.052
NGC 4594	S1.9	190.00	-11.62	51.15	0.002	0.136	3.113
IC 3639	S1h	190.22	-36.76	26.07	0.011	0.033	7.515
NGC 4636	S3b	190.71	2.69	65.47	0.003	0.07	0.14
NGC 4639	S1.0	190.72	13.26	75.98	0.001	0.001	1.41

continued on next page

Appendix A. VC-V AGN List

Table A.1 – continued from previous page

name	type	Ra/$^{\circ}$	Dec/$^{\circ}$	b/$^{\circ}$	z	$F_{6cm}/\text{Jy/Hz}$	$F_{60\mu\text{m}}/\text{Jy/Hz}$
NGC 4696	S3	192.21	-41.31	21.56	0.01	1.33	0.1
NGC 4736	S	192.72	41.12	76.01	0.001	0.106	71.54
NGC 4826	S	194.18	21.68	84.42	0.001	0.056	34.38
ESO 443-G17	H2	194.44	-29.77	33.09	0.01	0.015	5.96
ESO 507-G70	S	195.72	-23.92	38.88	0.022	0.037	13.66
NGC 4941	S2	196.05	-5.55	57.17	0.003	0.004	1.378
NGC 4939	S2	196.06	-10.34	52.40	0.01	0.001	2.015
NGC 4945	S	196.37	-49.47	13.34	0.002	2.82	359.3
NGC 4968	S2	196.77	-23.68	39.05	0.009	0.015	2.375
PKS 1306-241	S2	197.17	-24.38	38.32	0.014	0.22	1.44
NGC 4990	H2	197.32	-5.27	57.31	0.01	0.019	2.817
NGC 5005	S3b	197.73	37.06	79.25	0.003	0.062	19.65
NGC 5033	S1.8	198.36	36.59	79.45	0.003	0.07	13.8
NGC 5077	S3b	199.88	-12.66	49.64	0.008	0.167	-1
MCG -03.34.049	S1	200.03	-17.12	45.21	0.022	0.065	-1
MCG -03.34.064	S1h	200.60	-16.73	45.50	0.017	0.101	5.895
NGC 5135	S2	201.43	-29.83	32.45	0.013	0.059	16.91
TOL 1326-379	S3	202.32	-38.23	24.05	0.029	0.07	0.3761
NGC 5194	S2	202.47	47.19	68.56	0.001	0.525	32.68
MARK 789	H2	203.10	11.11	71.31	0.032	0.013	3.352
MCG -06.30.015	S1.5	203.97	-34.30	27.68	0.008	0.001	1.087
IC 4296	S3	204.16	-33.97	27.97	0.013	1.78	0.14
UGC 8621	S1.8	204.42	39.15	74.59	0.02	0.001	0.9654
NGC 5252	S2	204.57	4.54	64.80	0.022	0.018	-1
MARK 266SW	S2	204.57	48.28	66.97	0.028	0.044	-1
NGC 5253	H2	204.98	-31.64	30.11	0.001	0.075	30.51
MARK 270	S2	205.27	67.67	48.76	0.009	0.006	0.132
NGC 5273	S1.9	205.53	35.65	76.25	0.003	0.001	0.9
MARK 273	S2	206.18	55.89	59.68	0.037	0.103	21.74
MARK 1361	S	206.77	11.11	69.32	0.023	0.021	3.28
MARK 461	S2	206.82	34.15	76.10	0.016	0.002	0.3749
ESO 325-IG22	S2	207.06	-42.17	19.47	0.038	0.01	1.84
NGC 5322	S	207.31	60.19	55.49	0.006	0.043	0.4064
IC 4329A	S1.2	207.33	-30.31	30.92	0.016	0.024	2.03
UM 614	S1.8	207.47	2.08	61.30	0.033	0.01	-1
NGC 5318	S?	207.65	33.70	75.67	0.014	0.079	0.17
MARK 279	S1.0	208.26	69.31	46.86	0.031	0.008	1.255
NGC 5347	S2	208.32	33.49	75.23	0.008	0.002	1.424
NGC 5353	S?	208.36	40.28	71.63	0.008	0.035	0.2985
NGC 5371	S?	208.92	40.46	71.20	0.007	0.025	3.311
NGC 5427	S2	210.86	-6.03	52.55	0.009	0.002	4.861
NPM1G+13.0367	S3	212.67	13.56	67.05	0.017	0.004	3.696
NGC 5506	S1i	213.31	-3.21	53.81	0.007	0.132	8.409
NGC 5514	S3	213.41	7.66	62.46	0.024	0.061	1.308
MARK 673	S2	214.34	26.86	70.88	0.036	0.006	2.603
NGC 5548	S1.5	214.50	25.14	70.50	0.017	0.015	1.073
MARK 1490	H2	214.93	49.24	62.12	0.026	0.01	5.623
NGC 5597	H2	216.11	-16.76	40.65	0.008	0.013	8.7
NGC 5635	S3	217.13	27.41	68.46	0.014	0.151	0.2882
NGC 5675	S3	218.17	36.30	66.69	0.014	0.135	0.4724

continued on next page

Table A.1 – continued from previous page

name	type	Ra/$^{\circ}$	Dec/$^{\circ}$	b/$^{\circ}$	z	$F_{6cm}/\text{Jy/Hz}$	$F_{60\mu\text{m}}/\text{Jy/Hz}$
NGC 5643	S2	218.17	-44.17	15.03	0.003	0.064	19.49
NGC 5674	S1.9	218.47	5.46	57.38	0.025	0.01	1.444
MARK 817	S1.5	219.09	58.79	53.48	0.033	0.005	2.118
MARK 686	S2	219.34	36.57	65.71	0.014	0.003	0.5655
MARK 477	S1h	220.16	53.50	56.82	0.038	0.01	-1
NGC 5728	S1.9	220.60	-17.25	38.10	0.009	0.029	8.163
MARK 1388	S1.9	222.66	22.73	62.69	0.021	0.003	0.1744
MARK 841	S1.5	226.01	10.44	54.63	0.036	0.001	0.4593
NGC 5866	S	226.62	55.76	52.49	0.002	0.008	4.878
3C 317.0	S2	229.19	7.02	50.12	0.035	0.87	-1
MARK 848B	S3	229.53	42.75	56.49	0.04	0.042	-1
PKS 1521-30	S1	231.14	-30.21	21.99	0.02	0.39	-1
NGC 5929	S3	231.53	41.67	55.31	0.008	0.033	-1
NGC 5940	S1.0	232.83	7.46	47.35	0.034	0.004	0.7432
NGC 5953	S2	233.63	15.19	50.35	0.007	0.036	10.04
IC 4553	S	233.74	23.50	53.03	0.018	0.207	103.8
MARK 290	S1.5	233.97	57.90	47.95	0.03	0.002	0.1708
NGC 5972	S2	234.73	17.03	50.11	0.03	0.216	0.2473
MARK 860	S?	234.86	24.95	52.37	0.023	0.013	2.365
Zw 338.014	S?	235.73	70.83	40.16	0.025	0.047	-1
MARK 1102	S2	239.29	41.54	49.59	0.035	0.06	-1
MARK 493	S1n	239.79	35.03	49.41	0.032	0.001	0.6937
NGC 6104	S1.5	244.13	35.71	45.91	0.028	0.003	0.4997
MARK 699	S1.5	245.94	41.08	44.64	0.034	0.006	0.2453
MARK 883	S1.9	247.47	24.44	41.14	0.038	0.018	1.019
NGC 6251	S2	248.13	82.54	31.20	0.024	0.978	0.188
NGC 6217	H2	248.16	78.20	33.36	0.005	0.015	10.83
NGC 6211	S2	250.37	57.78	39.84	0.02	0.023	-1
NGC 6212	S1	250.85	39.81	40.87	0.03	0.064	-1
NGC 6221	S2	253.19	-59.22	-9.57	0.004	0.11	49.07
NGC 6240	S3	253.25	2.40	27.29	0.024	0.179	22.68
NGC 6300	S2	259.25	-62.82	-14.05	0.003	0.042	14.65
Arp 102B	S3b	259.81	48.98	34.94	0.025	0.156	-1
PKS 1718-649	S3	260.92	-65.01	-15.83	0.014	3.7	-1
GRS 1734-292	S1	264.37	-29.13	1.41	0.021	0.024	-1
NGC 6454	S?	266.24	55.70	31.34	0.031	0.562	-1
NGC 6521	S1.9	268.95	62.61	30.22	0.027	0.203	-1
NGC 6500	S3	269.00	18.34	20.23	0.01	0.176	0.6424
NGC 6552	S1h	270.03	66.62	29.80	0.027	0.033	2.453
F 49	S1h	279.24	-59.40	-21.34	0.019	0.066	3.227
NGC 6764	H2	287.07	50.93	18.23	0.008	0.036	6.328
1ES 1927+654	S2	291.82	65.57	20.97	0.017	0.016	-1
IRAS 19370-0131	H2	294.91	-1.41	-11.36	0.019	0.005	2.46
NGC 6814	S1.5	295.67	-10.32	-16.01	0.006	0.002	5.517
ESO 339-G11	S2	299.41	-37.93	-28.70	0.019	0.09	6.05
NGC 6890	S1.9	304.58	-44.81	-33.71	0.008	0.004	3.855
IC 4995	S2	305.00	-52.62	-34.47	0.016	0.005	0.8276
NGC 6951	S2	309.31	66.11	14.85	0.006	0.032	13.21
MARK 896	S1n	311.59	-2.81	-26.72	0.027	0.038	0.5134
PKS 2048-57	S1h	313.01	-57.07	-38.74	0.011	0.42	5.337

continued on next page

Appendix A. VC-V AGN List

Table A.1 – continued from previous page

name	type	Ra/$^{\circ}$	Dec/$^{\circ}$	b/$^{\circ}$	z	$F_{6cm}/\text{Jy/Hz}$	$F_{60\mu\text{m}}/\text{Jy/Hz}$
NGC 7018	S3	316.85	-25.43	-40.18	0.038	3.97	-1
II Zw 102	S2	316.94	3.88	-27.82	0.026	0.011	-1
NPM1G+24.0470	S1	324.92	24.41	-20.77	0.037	0.001	-1
IC 5135	S1.9	327.08	-34.95	-50.35	0.016	0.07	16.48
NGC 7135	No	327.44	-34.88	-50.65	0.007	0.004	0.218
PKS 2153-69	S1	329.27	-69.69	-40.65	0.028	13.4	0.1846
MARK 520	S1.9	330.17	10.55	-34.03	0.028	0.009	4.154
PKS 2158-380	S2	330.32	-37.77	-52.91	0.033	0.59	0.3494
NGC 7172	S2	330.51	-31.87	-53.07	0.008	0.02	5.712
PKS 2201+04	S1	331.07	4.67	-38.63	0.028	0.59	-1
NGC 7212	S1h	331.76	10.23	-35.38	0.026	0.046	2.885
NGC 7213	S3b	332.32	-47.17	-52.58	0.006	0.228	2.666
NPM1G-18.0578	S3	337.30	-18.18	-56.12	0.025	0.032	0.3094
ESO 602-G25	S	337.86	-19.03	-56.92	0.025	0.014	5.965
NGC 7314	S1h	338.94	-26.05	-59.74	0.005	0.002	3.736
MARK 915	S1.8	339.19	-12.55	-55.29	0.025	0.027	0.4578
UGC 12138	S1.8	340.07	8.05	-42.60	0.025	0.004	0.8259
MARK 917	S2	340.28	32.17	-23.08	0.025	0.014	3.714
AKN 564	S3	340.66	29.73	-25.34	0.025	0.009	0.8268
UGC 12243	S1	343.68	11.71	-41.94	0.028	0.002	0.469
IC 1459	S3	344.29	-36.46	-64.11	0.005	0.72	0.4666
MS 22549-3712	S1n	344.41	-36.94	-64.09	0.039	0.001	0.4759
MARK 1126	S1.5	345.20	-12.92	-60.49	0.01	0.004	-1
MARK 313	S3	345.50	15.96	-39.39	0.006	0.004	3.799
NGC 7469	S1.5	345.82	8.87	-45.47	0.017	0.061	25.87
MARK 315	S1.5	346.01	22.62	-33.89	0.04	0.007	1.464
NGC 7479	S1.9	346.24	12.32	-42.84	0.007	0.041	12.84
NGC 7552	H2	349.05	-42.58	-65.24	0.005	0.14	72.03
NGC 7591	S	349.57	6.59	-49.44	0.017	0.029	7.221
NGC 7592W	S2	349.59	-4.42	-58.24	0.024	0.01	-1
NGC 7582	S1i	349.60	-42.37	-65.70	0.005	0.11	49.1
NGC 7603	S1.5	349.74	0.24	-54.74	0.029	0.01	0.8525
NGC 7672	S2	351.88	12.39	-45.55	0.013	0.001	0.4563
NGC 7674	S1h	351.99	8.78	-48.79	0.029	0.067	5.588
NGC 7679	S2	352.19	3.51	-53.44	0.016	0.029	7.412
NGC 7682	S1h	352.27	3.53	-53.46	0.017	0.014	-1
MARK 930	H2	352.99	28.95	-30.78	0.019	0.01	1.245
NGC 7714	H2	354.06	2.16	-55.56	0.009	0.027	10.36
MARK 539	S?	355.99	2.75	-55.98	0.038	0.022	-1
NGC 7743	S2	356.09	9.93	-49.53	0.007	0.003	0.7911
MCG +02.60.017	S2	356.79	15.60	-44.52	0.026	0.005	4.263
Zw 098.038	S2	358.93	30.21	-31.13	0.031	0.081	-1

List of Correlated AGN

In section 2.4.2 a correlation study was introduced that used an exploratory UHECR data set up to March, 2nd 2008. The scan identified a list of 56 VC-V AGN, cf. first row of table 2.5. Some properties of those VC-V AGN which are correlated with the arrival direction of a UHECR as well as the number of correlations are listed in tables B.1.

Name	Type	k	z	$\log_{10}(F_{6\text{cm}} \cdot z^2 / \text{Jy})$	$L / (\text{W Hz}^{-1})$	V	$B - V$	$U - B$
PKS 1718-649	S3	2	0.014	-3.14	$1.52 \cdot 10^{24}$	15.5	?	?
NGC 5128	?	2	0.00083	-3.40	$8.38 \cdot 10^{23}$	12.76	1.72	0.83
IC 4296	S3	1	0.013	-3.52	$6.32 \cdot 10^{23}$	12.99	1.06	0.66
PKS 2048-57	S1h	1	0.011	-4.29	$1.07 \cdot 10^{23}$	13.6	1.09	0.38
PKS 1306-241	S2	1	0.014	-4.35	$9.06 \cdot 10^{22}$	13.9	?	?
IC 5135	S1.9	2	0.016	-4.75	$3.76 \cdot 10^{22}$	13.87	0.62	0.02
NGC 7469	S1.5	2	0.017	-4.75	$3.70 \cdot 10^{22}$	13.04	0.38	-0.72
NGC 1241	S2	3	0.013	-4.95	$2.38 \cdot 10^{22}$	12.7	?	?
NGC 4945	S	1	0.002	-4.95	$2.37 \cdot 10^{22}$	14.4	1.38	0.78
NGC 5135	S2	1	0.013	-5.00	$2.09 \cdot 10^{22}$	13.35	0.64	-0.08
NGC 7591	S	1	0.017	-5.08	$1.76 \cdot 10^{22}$	13.47	?	?
NGC 5506	S1i	1	0.007	-5.19	$1.36 \cdot 10^{22}$	14.38	0.87	0.14
NGC 2992	S1i	2	0.008	-5.31	$1.04 \cdot 10^{22}$	13.78	1.06	0.4

Table B.1.: Some properties of the correlated AGN taken from the VC-V catalog. Unavailable information is marked with a '?'. Column 1 yields the name of the AGN. Column 2 gives the astronomical classification and column 3 the number of correlations with the events within the scan minimum parameters, see first row of table 2.5 for details. Columns 4 to 6 hold redshift z , $\log_{10}(F_{6\text{cm}} \cdot z^2 / \text{Jy})$ as well as the corresponding luminosity in proper units of W Hz^{-1} , cf. equation 2.8. The last three columns hold V, B-V and U-B Filter (in units of [mag]) as defined in [4].

SPRT: Examples with Different p_1 Values

In chapter 2.9.1, a sequential probability ratio test (SPRT) was introduced to test the hypothesis of UHECR anisotropy. It was applied to an independent data set up to July, 4th 2010 in section 2.10. In order to create the SPRT test, a guess for the binomial signal probability $p_1 = 0.44$ had to be made in section 2.9.1. The development of the SPRT for different values of $p_1 = 0.3, 0.4, 0.5, 0.6$ is shown in figure C.1. It is noteworthy that only a guess of $p_1 = 0.6$ would have been ruled out with the presented independent data set. Of course, it is not allowed to alter the running SPRT or to draw conclusions from an a posteriori modified version of it. The intention of the graph is mainly to illustrate the response of the SPRT to different signal strength values.

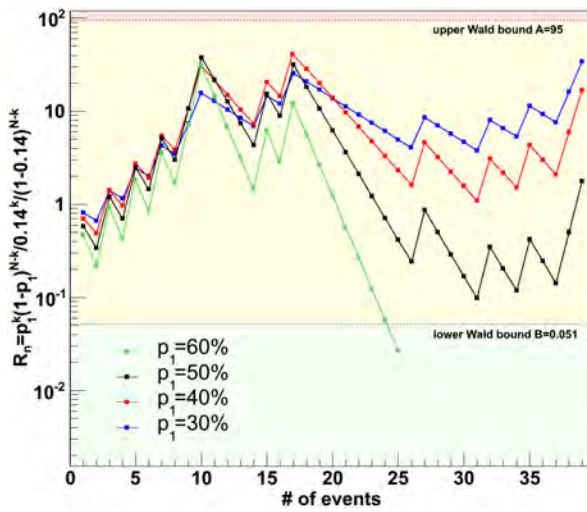


Figure C.1.: Likelihood ratio R_N as function of the number of events N (independent data until July, 4th 2010). Wald's bounds A, B (horizontal black lines) are used to divide the y-axis in three parts, cf. equation 2.11. The likelihood ratio has been calculated for different signal strength values of $p_1=0.3, 0.4, 0.5, 0.6$. The original SPRT with $p_1=0.44$ is presented in figure 2.14.

Appendix **D**

CMB Photon Number Density

This appendix derives the CMB photon number density $n(\varepsilon)$ as already given in equation 3.6. For further details see e.g. [12].

The Planck function $B_\lambda(T)$ describes the spectrum of a black body of temperature T as function of the photon wavelength λ

$$B_\lambda(T) = \frac{2hc^2}{\lambda^5(\exp(hc/\lambda/k/T) - 1)} \quad (\text{D.1})$$

where h , k are Planck's and Boltzman's constants. The units are [GeV/s/cm²/cm/sr]. Here, the separated 1/cm factor pronounces that one deals with an energy per time, area and steradians per unit wavelength interval - not energy per volume [1/cm³], steradians and time. If one wants to rewrite this equation in terms of the photon energy ε , the unit factor 1/cm needs to be changed to 1/GeV. This can be done by multiplying with $\lambda/h\nu = c/h\nu^2$ and replacing $\lambda = hc/\varepsilon$. One finds

$$B_\varepsilon(T) = \frac{1}{4\pi^3 h^3 c^2} \frac{\varepsilon^3}{(\exp(\varepsilon/k/T) - 1)}. \quad (\text{D.2})$$

Now, the units are [1/s/m²/sr]. Again, it is easier to understand what that means by writing [GeV/s/m²/sr/GeV]: energy of the radiation per area, second and steradians per photon energy interval $d\varepsilon$.

But what would be the amount of energy, $u_\varepsilon d\varepsilon$, per volume per photon energy interval e.g. in an infinitesimal cylinder of height dL with an area dA ? Assuming that the light can only enter the cylindrical volume through the round area dA and can be reflected on the curved walls of the length dL , the radiation would be trapped inside the volume $dV = dAdL$ for a time $dt = dL/\cos(\theta)$. Thus the trapped amount of energy would be

$$d(E_\varepsilon d\varepsilon) = B_\varepsilon d\varepsilon dt dA \cos(\theta) d\Omega = B_\varepsilon d\varepsilon d\Omega \frac{dV}{c}. \quad (\text{D.3})$$

This energy is trapped in the volume dV and one finds

$$d(u_\varepsilon d\varepsilon) = \frac{E_\varepsilon d\varepsilon}{dV} = \frac{1}{c} B_\varepsilon d\varepsilon d\Omega \quad (\text{D.4})$$

Integration gives

$$u_\varepsilon d\varepsilon = \frac{1}{c} B_\varepsilon d\varepsilon \int d\Omega = \frac{4\pi}{c} B_\varepsilon d\varepsilon \quad (\text{D.5})$$

Appendix D. CMB Photon Number Density

The number of photons within the energy interval $(\varepsilon, \varepsilon + \Delta\varepsilon)$ can be found by dividing the available energy by the single photon energy ε

$$N_\varepsilon(T) = \frac{u_\varepsilon(T)}{\varepsilon} d\varepsilon = n(\varepsilon) d\varepsilon = \frac{\varepsilon^2}{\pi^2 \hbar^3 c^3 (\exp(\frac{\varepsilon}{kT}) - 1)}. \quad (\text{D.6})$$

From that one can yield the photon number density as used in 3.6

$$n(\varepsilon) = \frac{\varepsilon^2}{\pi^2 \hbar^3 c^3 (\exp(\frac{\varepsilon}{kT}) - 1)}. \quad (\text{D.7})$$

Appendix **E**

Photonuclear Cross Sections For Light Nuclei

In chapter 3, a compilation of photonuclear cross sections was presented which is needed to calculate the mean free path λ for photodisintegration reactions of nuclei in low energy ambient photon fields using equation 3.13. For the majority of nuclei up to iron this cross sections have been calculated with TALYS [129]. But TALYS should not be used for light nuclei ($A < 12$). That is why for stable, light nuclei another source for the cross section is needed. A list of light nuclei which are included in the cross section collections of this work is given in 3.2. Here the corresponding graphs figure E.1-E.3 are presented.

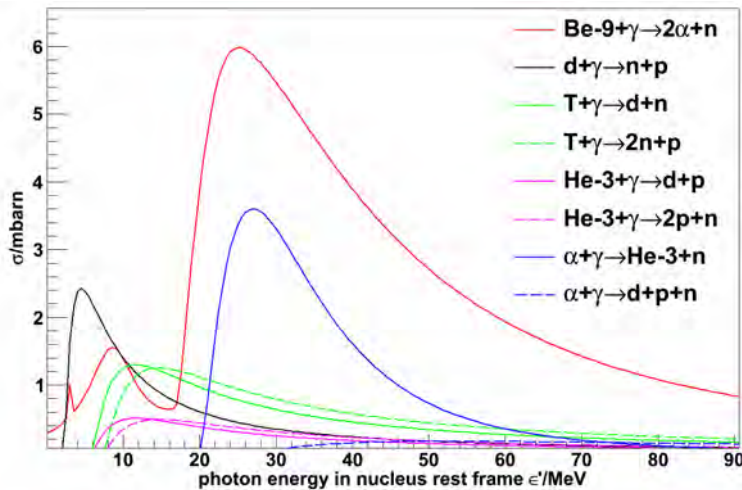


Figure E.1.: Photonuclear cross section data from [130] but modified: Fit of equation 3.20 (red) to ^9Be cross section data from [132] - this was already shown in figure 3.2. Tritium, Deuterium rescaled by factor 1.7, 0.66 respectively to match the maximum peak height of the measured data extracted from [124].

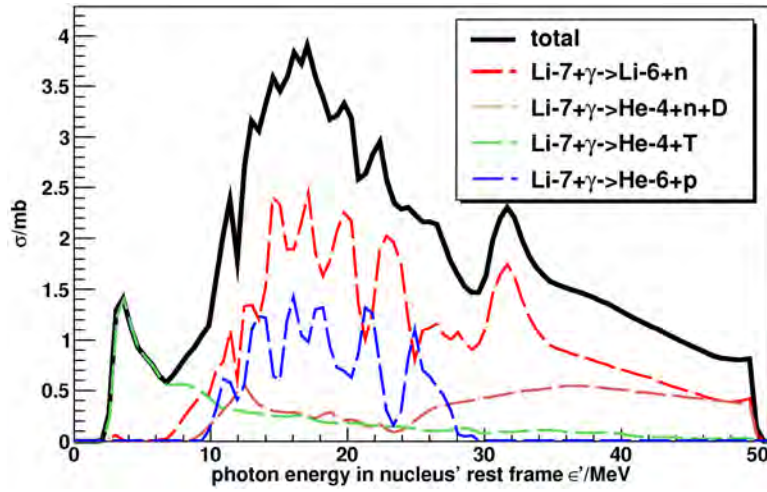


Figure E.2.: The total and the exclusive photonuclear cross section channels for ${}^7\text{Li}$: (G,abs), (G,n+D), (G,T) [133]; (G,p) [134]. The total cross section (G,abs) minus the sum of the cross section channels (G,p)+(G,n+D)+(G,T) is assigned to the neutron channel (G,n).

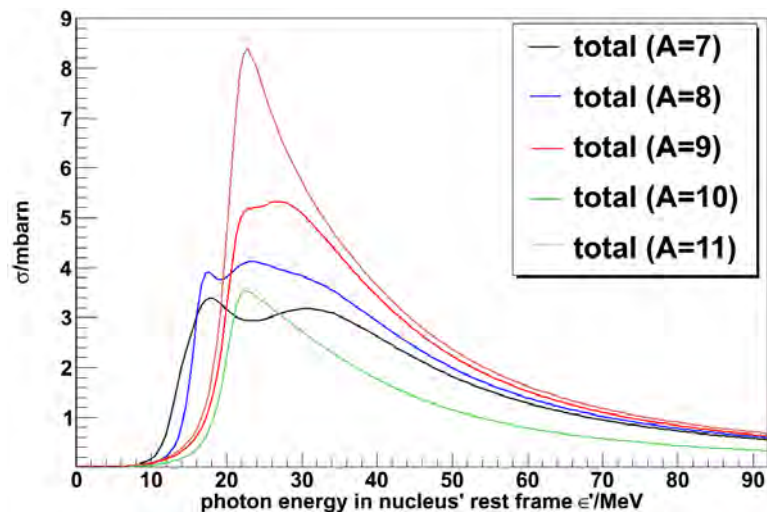


Figure E.3.: For light nuclei ($A < 12$) without available measured photo nuclear cross sections but short half life times, a parametrization of the total photo nuclear cross section as function of the mass number A is used [131]. Note, exceptions are ${}^9\text{Be}$, ${}^4\text{He}$, ${}^3\text{He}$, T, D and ${}^7\text{Li}$. See table 3.2 for futher information.

Bibliography

- [1] Pierre Auger Collaboration, “Correlation of the Highest-Energy Cosmic-Rays with Nearby Extragalactic Objects,” *Science* **318** (2007).
(Cited on page 3.)
- [2] Pierre Auger Collaboration, “Observation of the Suppression of the Flux of Cosmic Rays above 4×10^{19} eV,” *Physical Review Letters* **101** (Aug., 2008) 061101, 0806.4302.
(Cited on page 3.)
- [3] M. Unger, “Study of the Cosmic Ray Composition above 0.4 EeV using the Longitudinal Profiles of Showers observed at the Pierre Auger Observatory,” in *Proceedings of the ICRC 2007, Merida (Mexico)*, 2007.
(Cited on pages 3 and 77.)
- [4] Véron-Cetty and Véron, “A catalogue of quasars and active nuclei: 12th edition,” *Astron. & Astrophys.* **455** (Mar., 2006) 773.
(Cited on pages 3, 4, 45, 46, 111, and 119.)
- [5] The Pierre AUGER Collaboration, “Correlation of the highest-energy cosmic rays with the positions of nearby active galactic nuclei,” *Astroparticle Physics* **29** (Apr., 2008) 188–204, 0712.2843.
(Cited on pages 3, 31, 39, 42, 45, 46, 61, and 97.)
- [6] J. Blümner, R. Engel, and J. R. Hörandel, “Cosmic rays from the knee to the highest energies,” *Progress in Particle and Nuclear Physics* **63** (Oct., 2009) 293–338, 0904.0725.
(Cited on pages 9, 10, and 24.)
- [7] T. Stanev, *High Energy Cosmic Rays*. Springer Verlag, 2003.
(Cited on pages 9, 11, 24, and 34.)
- [8] M. Unger, “Cosmic Rays above the Knee,” *ArXiv e-prints* (Dec., 2008) 0812.2763.
(Cited on pages 9 and 15.)
- [9] K.-H. Kampert, “Ultra-High Energy Cosmic Ray and Neutrino Observations,” *ArXiv e-prints* (Nov., 2009) 0911.1089.
(Cited on pages 9, 13, and 29.)
- [10] P. Sommers, “Recent Results from the Pierre Auger Observatory,” in *Proceedings of the ICRC 2009, Lodz (Poland)*, 2009.
(Cited on page 9.)
- [11] M. Fukushima, “Measurement of High Energy Cosmic Rays above 10^{16} eV,” in *Proceedings of the ICRC 2009, Lodz (Poland)*, 2009.

Bibliography

- (Cited on pages 9, 13, 14, and 32.)
- [12] B. W. Carroll and D. A. Ostlie, *AN INTRODUCTION TO Modern Astrophysics*. Addison-Wesley Publishing Company, inc., 1996.
(Cited on pages 9, 12, 15, 99, and 123.)
- [13] V. F. Hess, “Über Beobachtungen der durchdringenden Strahlung bei sieben Freiballonfahrten,” *Phys. Z.* **13** (1912) 1084.
(Cited on page 9.)
- [14] P. Auger *et. al.*, “Extensive Cosmic-Ray Showers,” *Rev. of Mod. Phys.* **11** (July, 1939) 288.
(Cited on page 9.)
- [15] Kohlster.
Naturw. **26**, 1938, 576.
(Cited on page 9.)
- [16] Pierre AUGER Collaboration, “Measurement of the energy spectrum of cosmic rays above 10^{18} eV using the Pierre Auger Observatory,” *Physics Letters B* **685** (Mar., 2010) 239–246, 1002.1975.
(Cited on pages 10 and 14.)
- [17] T. Antoni *et. al.*, “KASCADE measurements of energy spectra for elemental groups of cosmic rays: Results and open problems,” *Astropart. Phys.* **24** (Sept., 2005) 1.
(Cited on page 11.)
- [18] W. Baade and F. Zwicky, “Remarks on super-novae and cosmic rays,” *Phys. Rev.* **46** (Jul, 1934) 76–77.
(Cited on page 11.)
- [19] E. Fermi, “On the origin of the Cosmic Rays,” *Phys. Rev.* **75** (1949), no. 8 1169.
(Cited on page 11.)
- [20] H. Kolanoski, “Einführung in die Astroteilchenphysik (in German).” available at <http://www-zeuthen.desy.de/kolanosk/astro0910/skript.html>.
(Cited on pages 11 and 20.)
- [21] T. K. Gaisser, *Cosmic Rays and Particle Physics*. Cambridge University press, 1990.
(Cited on page 11.)
- [22] A. R. Bell and S. G. Lucek, “Cosmic ray acceleration to very high energy through the non-linear amplification by cosmic rays of the seed magnetic field,” *MON. NOT. OF THE ROYAL ASTRON. SOC.* **321** (Mar., 2001) 433–438.
(Cited on page 11.)
- [23] M. Wiedenbeck *et. al.* in *Proceedings of the ICRC 2003, Tsukuba*, 2003.
(Cited on page 11.)
- [24] L. Anchordoqui, T. Paul, S. Reucroft, and J. Swain, “Ultrahigh Energy Cosmic Rays,” *International Journal of Modern Physics A* **18** (2003) 2229–2366, arXiv:hep-ph/0206072.
(Cited on page 12.)
- [25] A. M. Hillas, “The Origin of Ultra-High-Energy Cosmic Rays,” *Ann. Rev. Astron. Astrophys.* **22** (1984) 425.
(Cited on page 12.)
- [26] M. J. Hardcastle, “Which radio galaxies can make the highest energy cosmic rays?,” *Mon. Not. of the Royal Astron. Soc.* **405** (July, 2010) 2810–2816, 1003.2500.
(Cited on page 13.)
- [27] S. Massaglia, “Active Galactic Nuclei, Radio Jets and Acceleration of UHECRs,” *Nuclear*

- Physics B Proceedings Supplements* **190** (May, 2009) 79–84, 0812.4945.
 (Cited on pages 13, 15, and 18.)
- [28] G. E. Romero, J. A. Combi, S. E. Perez Bergliaffa, and L. A. Anchordoqui, “Centaurus A as a source of extragalactic cosmic rays with arrival energies well beyond the GZK cutoff,” *Astroparticle Physics* **5** (Oct., 1996) 279–283, arXiv:gr-qc/9511031.
 (Cited on page 13.)
- [29] M. J. Hardcastle, C. C. Cheung, I. J. Feain, and Ł. Stawarz, “High-energy particle acceleration and production of ultra-high-energy cosmic rays in the giant lobes of Centaurus A,” *Mon. Not. of the Royal Astron. Soc.* **393** (Mar., 2009) 1041–1053, 0808.1593.
 (Cited on page 13.)
- [30] S. O’Sullivan, B. Reville, and A. M. Taylor, “Stochastic particle acceleration in the lobes of giant radio galaxies,” *Mon. Not. of the Royal Astron. Soc.* **400** (Nov., 2009) 248–257, 0903.1259.
 (Cited on page 13.)
- [31] M. Lemoine and E. Waxman, “Anisotropy vs chemical composition at ultra-high energies,” *Journ. of Cosm. and Astr. Phys.* **11** (Nov., 2009) 9, 0907.1354.
 (Cited on page 13.)
- [32] D. Gorbunov, P. Tinyakov, I. Tkachev, and S. Troitsky, “On the correlation of the highest-energy cosmic rays with nearby extragalactic objects reported by the Pierre Auger Collaboration,” *Soviet Journal of Experimental and Theoretical Physics Letters* **87** (July, 2008) 461–463, 0711.4060.
 (Cited on page 13.)
- [33] P. L. Biermann and P. A. Strittmatter, “Synchrotron emission from shock waves in active galactic nuclei,” *Astroph. Journal* **322** (Nov., 1987) 643–649.
 (Cited on page 13.)
- [34] R. J. Protheroe and A. P. Szabo, “High energy cosmic rays from active galactic nuclei,” *Phys. Rev. Lett.* **69** (Nov, 1992) 2885–2888.
 (Cited on page 13.)
- [35] K. Greisen, “End to the Cosmic-Ray Spectrum?,” *Phys. Rev. Let.* **16** (1966).
 (Cited on page 13.)
- [36] G. T. Zatsepin and V. A. Kuz’min *Sov. Phys. JETP Lett.* **4** (1966) 78. engl. Translation.
 (Cited on page 13.)
- [37] J. L. Puget, F. W. Stecker, and J. H. Bredekamp, “Photonuclear interactions of ultrahigh energy cosmic rays and their astrophysical consequences,” *ASTROPH. JOURNAL* **205** (Apr, 1976) 638–654.
 (Cited on pages 13, 77, and 79.)
- [38] A. P. Szabo and R. J. Protheroe, “Implications of particle acceleration in active galactic nuclei for cosmic rays and high energy neutrino astronomy,” *Astroparticle Physics* **2** (Oct., 1994) 375–392, arXiv:astro-ph/9405020.
 (Cited on page 14.)
- [39] The High Resolution Fly’S Eye Collaboration, “Measurement of the flux of ultra high energy cosmic rays by the stereo technique,” *Astroparticle Physics* **32** (Aug., 2009) 53–60, 0904.4500.
 (Cited on page 14.)
- [40] P. Bhattacharjee, “Origin and propagation of extremely high energy cosmic rays,” *Physics Reports* **327** (Mar., 2000) 109–247, arXiv:astro-ph/9811011.
 (Cited on page 14.)

Bibliography

- [41] J. R. Hörandel, “On the knee in the energy spectrum of cosmic rays,” *Astroparticle Physics* **19** (May, 2003) 193–220, arXiv:astro-ph/0210453.
(Cited on page 15.)
- [42] I. V. Moskalenko, L. Stawarz, T. A. Porter, and C. C. Cheung, “On the Possible Association of Ultra High Energy Cosmic Rays With Nearby Active Galaxies,” *Astroph. Journal* **693** (Mar., 2009) 1261–1274, 0805.1260.
(Cited on pages 15, 32, and 72.)
- [43] R. J. Buta, “Galaxy Morphology,” *ArXiv e-prints* (Feb., 2011) 1102.0550.
(Cited on page 15.)
- [44] “CSIRO webpage.”
See <http://www.narrabri.atnf.csiro.au/public/images/b1545-321/>.
(Cited on page 17.)
- [45] B. L. Fanaroff and J. M. Riley, “The morphology of extragalactic radio sources of high and low luminosity,” *Mon. Not. of the Royal Astron. Soc.* **167** (May, 1974) 31P–36P.
(Cited on page 17.)
- [46] “Robert Wagner’s list of VHE gamma sources.”
See <http://www.mppmu.mpg.de/rwagner/sources/>.
(Cited on page 19.)
- [47] J. Hinton, “Ground-based gamma-ray astronomy with Cherenkov telescopes,” *New Journal of Physics* **11** (May, 2009) 055005, 0803.1609.
(Cited on page 18.)
- [48] Albert *et. al.* *Science* **320** (2008).
(Cited on page 19.)
- [49] M. Böttcher, A. Reimer, and A. P. Marscher, “Implications of the very High Energy Gamma-Ray Detection of the Quasar 3C279,” *Astroph. Journal* **703** (Sept., 2009) 1168–1175.
(Cited on page 19.)
- [50] A. E. Wehrle, B. G. Piner, S. C. Unwin, A. C. Zook, W. Xu, A. P. Marscher, H. Teräsranta, and E. Valtaoja, “Kinematics of the Parsec-Scale Relativistic Jet in Quasar 3C 279: 1991-1997,” *Astroph. Journal Suppl. Series* **133** (Apr., 2001) 297–320, arXiv:astro-ph/0008458.
(Cited on page 19.)
- [51] W. Essey, O. Kalashev, A. Kusenko, and J. F. Beacom, “Role of line-of-sight cosmic ray interactions in forming the spectra of distant blazars in TeV gamma rays and high-energy neutrinos,” *ArXiv e-prints* (Nov., 2010) 1011.6340.
(Cited on page 19.)
- [52] J. M. Shuder, “Emission-line-continuum correlations in active galactic nuclei,” *Astroph. Journal* **244** (Feb., 1981) 12–18.
(Cited on page 20.)
- [53] R. R. J. Antonucci and J. S. Miller, “Spectropolarimetry and the nature of NGC 1068,” *Astroph. Journal* **297** (Oct., 1985) 621–632.
(Cited on page 20.)
- [54] J. K. Becker, “High-energy neutrinos in the context of multimessenger astrophysics,” *Physics Reports* **458** (Mar., 2008) 173–246, 0710.1557.
(Cited on pages 21 and 27.)
- [55] University of Adelaide, “High Energy Astrophysics.”
<http://www.physics.adelaide.edu.au/astrophysics/hires/uhecr.html>.

- (Cited on page 23.)
- [56] T. Huege and H. Falcke, “Radio Emission from EAS Coherent Geosynchrotron Radiation,” in *International Cosmic Ray Conference*, vol. 1, p. 291, July, 2003.
arXiv:astro-ph/0305332.
(Cited on page 23.)
- [57] B. Rossi and K. Greisen *Res. Mod. Phys.* **13** (1941).
(Cited on page 24.)
- [58] B. Rossi, ““high energy particles”,” *Prentice Hall, New York* (1952).
(Cited on page 24.)
- [59] K. Greisen *Prog. Cosmic Ray Physics* **3** (1956).
(Cited on page 24.)
- [60] K. Kamata and J. Nishimura *Prog. Theor. Phys.* **6** (1958).
(Cited on page 24.)
- [61] J. Alvarez-Muñiz, R. Engel, T. K. Gaisser, J. A. Ortiz, and T. Stanev, “Hybrid simulations of extensive air showers,” *Phys. Rev. D* **66** (Aug., 2002) 033011, arXiv:astro-ph/0205302.
(Cited on page 25.)
- [62] Pierog *et. al.* in *Proceedings of the ICRC 2005, Pune 7* (2005) 103, 2005.
(Cited on page 25.)
- [63] Pierre AUGER Collaboration, “Upper limit on the cosmic-ray photon flux above 10^{19} eV using the surface detector of the Pierre Auger Observatory,” *Astroparticle Physics* **29** (May, 2008) 243–256, 0712.1147.
(Cited on page 26.)
- [64] J. Abraham *et. al.*, “An upper limit to the photon fraction in cosmic rays above 10^{19} eV from the Pierre Auger Observatory,” *Astropart. Phys.* **27** (Mar., 2007) 155,
arXiv:astro-ph/0606619.
(Cited on page 26.)
- [65] J. Abraham *et. al.*, “Measurement of the Depth of Maximum of Extensive Air Showers above 10^{18} eV,” *Physical Review Letters* **104** (Mar., 2010) 091101, 1002.0699.
(Cited on pages 26 and 27.)
- [66] R. U. Abbasi *et. al.*, “Indications of Proton-Dominated Cosmic-Ray Composition above 1.6 EeV,” *Physical Review Letters* **104** (Apr., 2010) 161101, 0910.4184.
(Cited on page 26.)
- [67] P. Homola, “Ultra-high energy photon studies with the Pierre Auger Observatory,” in *Proceedings of the ICRC 2009, Lodz (Poland)*, 2009.
(Cited on page 28.)
- [68] L. D. Landau and I. Y. Pomeranchuk *Dokl. Akad. Nauk SSSR* **92** (1953) 535 & 735.
(Cited on page 28.)
- [69] A. B. Migdal, “Bremsstrahlung and Pair Production in Condensed Media at High Energies,” *Phys. Rev.* **103** (1956) 1811.
(Cited on page 28.)
- [70] The IceCube Collaboration, “Constraints on the Extremely-high Energy Cosmic Neutrino Flux with the IceCube 2008-2009 Data,” *ArXiv e-prints* (Mar., 2011) 1103.4250.
(Cited on page 29.)
- [71] R. Abbasi and et al., “Measurement of the atmospheric neutrino energy spectrum from 100 GeV to 400 TeV with IceCube,” *Phys. Rev. D* **83** (Jan., 2011) 012001–+, 1010.3980.
(Cited on page 29.)
- [72] K.-H. Kampert, “in private communication.”.

Bibliography

- (Cited on page 29.)
- [73] G. Sigl, F. Miniati, and T. A. Enßlin, “Cosmic Magnetic Fields and Their Influence on Ultra-High Energy Cosmic Ray Propagation,” *Nuclear Physics B Proceedings Supplements* **136** (Nov., 2004) 224–233, arXiv:astro-ph/0409098.
- (Cited on page 30.)
- [74] P. P. Kronberg, “Cosmic magnetic fields and implications for HE particle anisotropies,” *ArXiv e-prints* (Nov., 2010) 1011.4467.
- (Cited on page 29.)
- [75] G. Sigl, “Propagation of ultra-high-energy radiation,” *Physics and Astrophysics of Ultra-High-Energy Cosmics Rays* (2001) 198.
- (Cited on page 30.)
- [76] The AGASA collaboration, “Possible Clustering of the Most Energetic Cosmic Rays within a Limited Space Angle Observed by the Akeno Giant Air Shower Array,” *Physical Review Letters* **77** (1996) 1000–1003.
- (Cited on page 30.)
- [77] R. U. Abbasi and others (HiRes Collaboration) *Astropart. Phys.* **22** (2004) 139–149.
- (Cited on page 30.)
- [78] D. Harari, “Search for correlation of UHECRs and BL Lacs in Pierre Auger Observatory data,” in *International Cosmic Ray Conference*, vol. 4, pp. 283–286, 2008. 0706.1715.
- (Cited on page 31.)
- [79] R. U. Abbasi *et. al.* *Astropart. Phys.* **30** (2008) 175–179.
- (Cited on page 31.)
- [80] The Pierre AUGER Collaboration, “Update on the correlation of the highest energy cosmic rays with nearby extragalactic matter,” *Astroparticle Physics* **34** (Dec., 2010) 314–326, 1009.1855.
- (Cited on pages 31 and 58.)
- [81] N. M. Nagar and J. Matulich, “Ultra-high energy cosmic rays detected by the Pierre Auger observatory. First direct evidence, and its implications, that a subset originate in nearby radiogalaxies,” *Astron. & Astrophys.* **488** (Sept., 2008) 879–885, 0806.3220.
- (Cited on page 32.)
- [82] The Pierre Auger Collaboration, “Astrophysical Sources of Cosmic Rays and Related Measurements with the Pierre Auger Observatory,” *ArXiv e-prints* (June, 2009) 0906.2347.
- (Cited on page 32.)
- [83] J. P. Rachen, “Ultra-high energy cosmic rays from radio galaxies revisited,” *ArXiv e-prints* (Aug., 2008) 0808.0349.
- (Cited on pages 32 and 95.)
- [84] M. Raue *et. al.*, “Discovery of VHE γ -rays from Centaurus A,” in *Accretion and Ejection in AGN: a Global View* (L. Maraschi, G. Ghisellini, R. Della Ceca, & F. Tavecchio, ed.), vol. 427 of *Astronomical Society of the Pacific Conference Series*, p. 302, Oct., 2010. 0904.2654.
- (Cited on page 33.)
- [85] N. Busca, *The Ultra High Energy Cosmic Ray Flux from the Southern Pierre Auger Observatory Data*. PhD thesis, University of Chicago, 2006.
- (Cited on page 36.)

- [86] T. K. Gaisser *et. al.* in *Proceedings of the ICRC 1977, Plovdiv (1977)*, p. 358, 1977.
(Cited on page 34.)
- [87] The Pierre Auger Collaboration, “The angular resolution of the Pierre Auger Observatory,” *Nuclear Physics B Proceedings Supplements* **190** (May, 2009) 20–25, 0901.3138.
(Cited on pages 34 and 36.)
- [88] The Pierre Auger Collaboration, “The Cosmic Ray Energy Spectrum and Related Measurements with the Pierre Auger Observatory,” *ArXiv e-prints* (June, 2009) 0906.2189.
(Cited on pages 36 and 37.)
- [89] A. M. Hillas *Acta Physica Academiae Scientiarum Hungaricae Suppl.* **3** **29** (1970) 355.
(Cited on page 36.)
- [90] The Pierre Auger Collaboration, “Operations of and Future Plans for the Pierre Auger Observatory,” *ArXiv e-prints* (June, 2009) 0906.2354.
(Cited on page 37.)
- [91] T. Ebisuzaki and for the JEM-EUSO Collaboration, “The JEM-EUSO Mission,” *ArXiv e-prints* (Jan., 2011) 1101.1909.
(Cited on page 37.)
- [92] A. Wald *Ann. Math. Stat.* **16** (Mar., 1945) 117.
(Cited on pages 39, 58, and 60.)
- [93] D. Harari, S. Mollerach, and E. Roulet,, “Correlation of cosmic rays with astronomical objects in the Pierre Auger Observatory data.” GAP-note 2006-046 (not public).
(Cited on pages 39, 40, and 41.)
- [94] P. Sommers, “Cosmic ray anisotropy analysis with a full-sky observatory,” *Astroparticle Physics* **14** (Jan., 2001) 271–286, arXiv:astro-ph/0004016.
(Cited on page 40.)
- [95] G. Cowan, *Statistical Data Analysis*, vol. 1989.
Clarendon Press, 1998.
(Cited on page 41.)
- [96] “AGN correlation studies web page.”
See <http://cabtep5.cnea.gov.ar/experiments/auger/private/AGN/>.
(Cited on page 41.)
- [97] J. D. Hague, “Correlation of the Highest Energy Cosmic Rays with Nearby Extragalactic Objects in Pierre Auger Observatory Data,” in *Proceedings of the ICRC 2009, Lodz (Poland)*, 2009.
(Cited on pages 42 and 62.)
- [98] The Pierre Auger Collaboration, “The CDAS Herald webpage.” See
<http://www.auger.org.ar/CDAS/Herald/>.
(Cited on pages 42 and 45.)
- [99] D. Allard, “The trigger system of the Pierre Auger Surface Detector: operation, efficiency and stability,” in *Proceedings of the ICRC 2005, Pune (India)*, 2005.
ICRC 2001.
(Cited on page 45.)
- [100] O. Blanch *et. al.*, “Are the Precise Values of the Scan Minimum Meaningful?” Internal Auger GAP-note (not public).
(Cited on pages 45 and 54.)
- [101] The Pierre Auger Collaboration, “Exculator.”
<http://ipnweb.in2p3.fr/auger/AugerProtected/formulaire1.html>.

Bibliography

- (Cited on page 45.)
- [102] The Pierre Auger Collaboration, “Acceptance main web page.” See <http://ipnweb.in2p3.fr/auger/AugerProtected/AcceptWork.html>.
(Cited on page 45.)
- [103] I. D. Karachentsev *et. al.*, “A Catalog of Neighboring Galaxies,” *The Astronomical Journal* **127** (2004).
(Cited on page 46.)
- [104] M. E. Filho, P. D. Barthel, and L. C. Ho, “A radio census of nuclear activity in nearby galaxies,” *Astronomy and Astrophysics* **451** (may, 2006) 71–83.
(Cited on page 46.)
- [105] B. Jones P.A., McAdam *Astroph. Journal Suppl. Series* **80** (Mar., 1992) 137.
(Cited on pages 46 and 100.)
- [106] D. N. Spergel *et. al.*, “Wilkinson microwave anisotropy probe (wmap) three year results: Implications for cosmology,” *ASTROPH. JOURNAL SUPPL. SERIES* **170** (2007) 377.
(Cited on page 46.)
- [107] J. J. Condon *et. al.*, “THE NRAO VLA SKY SURVEY,” *ASTRON. JOURN.* **115** (1998) 1693.
(Cited on page 46.)
- [108] G. P. Rybicki and A. P. Lightman, *Radiative processes in astrophysics*, vol. 1989. Wiley, 1979.
(Cited on page 47.)
- [109] D. Kruppke *et. al.*, “A short note on the redshift and angle parameter in the AGN correlation analysis.” Internal Auger GAP-note (not public).
(Cited on page 51.)
- [110] N. Nierstenhoefer *et. al.*, “UHECR-Source Identification using Radio Fluxes in a Four Dimensional Scan.” Internal Auger GAP-note (not public), 11, 2008.
(Cited on page 51.)
- [111] S. Y. BenZvi *et. al.*, “Sequential Analysis Techniques for Correlation Studies in Particle Astronomy,” *Astroph. Journal* **687** (Nov., 2008) 1035–1042, 0711.3937.
(Cited on page 58.)
- [112] AAARG group, “A Prescription for A Search for Correlation between AGN and Ultra-High Energy Cosmic Rays with the Pierre Auger Observatory.” GAP-note 2006-096 (not public).
(Cited on page 61.)
- [113] M. J. Ledlow and F. N. Owen, “20 CM VLA Survey of Abell Clusters of Galaxies. VI. Radio/Optical Luminosity Functions,” *Astron. Journ.* **112** (July, 1996) 9, arXiv:astro-ph/9607014.
(Cited on page 72.)
- [114] J. K. Becker, P. L. Biermann, J. Dreyer, and T. M. Kneiske, “Cosmic Rays VI - Starburst galaxies at multiwavelengths,” *ArXiv e-prints* (Jan., 2009) 0901.1775.
(Cited on pages 72 and 73.)
- [115] NASA Extragalactic Database, “NED.” See <http://nedwww.ipac.caltech.edu/>.
(Cited on pages 72 and 111.)
- [116] M. Erdmann, “UHECR Experimental Procedures: Anisotropy and Magnetic Fields.” Conference contribution without proceedings. International Workshop on Ultra high Energy Cosmic Rays and Magnetic Fields in the Universe, Ringberg Castle, Tegernsee, Germany, 2009.
(Cited on page 77.)

- [117] “Offline Wiki-pages.”
See <https://www.auger.unam.mx/AugerWiki/OfflineSoftware>.
(Cited on page 77.)
- [118] D. Heck *et. al.*, “CORSIKA web page.” See <http://www-ik.fzk.de/corsika/Welcome.html>.
(Cited on page 77.)
- [119] E. Armengaud, G. Sigl, T. Beau, and F. Miniati, “CRPropa: A numerical tool for the propagation of UHE cosmic rays, γ -rays and neutrinos,” *Astroparticle Physics* **28** (Dec., 2007) 463–471, arXiv:astro-ph/0603675.
(Cited on pages 77, 78, and 82.)
- [120] E. Khan *et. al.*, “Photodisintegration of ultra-high-energy cosmic rays revisited,” *Astroparticle Physics* **23** (Mar., 2005) 191–201, arXiv:astro-ph/0412109.
(Cited on pages 77, 78, 83, 91, and 93.)
- [121] K.-H. Kampert *et. al.*, “Propagation of Ultra-High Energy Nuclei with CRPropa,” in *Proceedings of the ICRC 2009, Lodz (Poland)* (B. Dawson and P. Sommers, eds.), 2009. ICRC 2009.
(Cited on page 78.)
- [122] A. Mücke, R. Engel, J. P. Rachen, R. J. Protheroe, and T. Stanev, “Monte Carlo simulations of photohadronic processes in astrophysics,” *Computer Physics Communications* **124** (Feb., 2000) 290–314, arXiv:astro-ph/9903478.
(Cited on page 79.)
- [123] G. R. Blumenthal, “Energy loss of high-energy cosmic rays in pair-producing collisions with ambient photons,” *Phys. Rev. D* **1** (Mar, 1970) 1596–1602.
(Cited on page 79.)
- [124] National Nuclear Data Center, “NuDat 2 database.” See <http://www.nndc.bnl.gov/nudat2/>.
(Cited on pages 80, 83, 85, 91, and 125.)
- [125] F. W. Stecker, “Effect of photomeson production by the universal radiation field on high-energy cosmic rays,” *Phys. Rev. Lett.* **21** (Sep, 1968) 1016–1018.
(Cited on page 80.)
- [126] J. W. Elbert and P. Sommers, “In search of a source for the 320 EeV Fly’s Eye cosmic ray,” *Astroph. Journal* **441** (Mar., 1995) 151–161, arXiv:astro-ph/9410069.
(Cited on page 80.)
- [127] J. R. Primack, J. S. Bullock, and R. S. Somerville, “Observational Gamma-ray Cosmology,” in *High Energy Gamma-Ray Astronomy* (F. A. Aharonian, H. J. Völk, & D. Horns, ed.), vol. 745, pp. 23–33, Feb., 2005.
arXiv:astro-ph/0502177.
(Cited on page 80.)
- [128] T. Kneiske, “in private communication.”
University of Hamburg.
(Cited on page 80.)
- [129] A. Koning *et. al.*, “TALYS-1.0,” in *Proceedings of the International Conference on Nuclear Data for Science and Technology*, pp. 211–214, EDP Sciences, 2008.
(Cited on pages 83, 91, 95, and 125.)
- [130] J. Rachen, *Interaction Processes and Statistical Properties of the Propagation of Cosmic Rays in Photon Backgrounds*.
PhD thesis, Universität zu Bonn, 1996.
(Cited on pages 83, 84, 85, 91, 95, and 125.)
- [131] M. V. Kossov, “Approximation of photonuclear interaction cross-sections,” *European*

Bibliography

- Physical Journal A* **14** (2002) 377–392.
(Cited on pages 83, 84, 85, 95, and 126.)
- [132] J. Ahrens, “The total absorption of photons by nuclei.,” *Nuclear Physics, Section A* **446** (1985) 229(C).
(Cited on pages 83, 84, and 125.)
- [133] V. V. Varlamov *et. al.*, *PHOTONUCLEAR DATA. PHOTODISINTEGRATION OF LITHIUM. EVALUATED CROSS SECTIONS OF CHANNELS AND REACTIONS*. Fotojad.Danny - Photodisint.of Li,Suppl.,Moscow 1986, 1986.
(Cited on pages 84, 85, and 126.)
- [134] L. A. Kulchitskii, Y. M. Volkov, V. P. Denisov, and V. I. Ogurtsov, “Energy levels of li⁷ observed in its photoemission,” *Izv. Rossiiskoi Akademii Nauk, Ser.Fiz.* **27** (1963), no. 11 1412.
(Cited on pages 84, 85, and 126.)
- [135] J. K. Kulbartz, “in private communication.”
University of Hamburg.
(Cited on page 92.)
- [136] S. Riggi, “Combined Spectrum and Xmax fits.” Talk held at the Pierre Auger Collaboration meeting, November 14-20 2009 (unpublished).
(Cited on pages 93 and 94.)
- [137] D. Perkins, *Particle Astrophysics*, vol. 1989.
Oxford University Press, 2003.
(Cited on page 95.)
- [138] S. Riggi, “in private communication.”
University of Santiago de Compostela.
(Cited on page 95.)
- [139] J. Huchra *et. al.*, “in private communication.” (publication in prep.).
(Cited on page 98.)
- [140] “2MASS Documentation.”
See <http://www.ipac.caltech.edu/2mass/>.
(Cited on page 98.)
- [141] “NVSS Documentation.”
See <http://www.cv.nrao.edu/nvss/>.
(Cited on page 98.)
- [142] “SUMSS Documentation.”
See <http://www.astrop.physics.usyd.edu.au/sumsscat/>.
(Cited on page 98.)
- [143] H. Kuehr, A. Witzel, I. I. K. Pauliny-Toth, and U. Nauber, “A catalogue of extragalactic radio sources having flux densities greater than 1 Jy at 5 GHz,” *Astron. & Astroph. Supplement* **45** (Sept., 1981) 367–430.
(Cited on page 101.)
- [144] S. van Velzen, “in private communication.”
University of Nijmegen, Netherlands.
(Cited on page 101.)